LAPPEENRANTA
UNIVERSITY OF TECHNOLOGY

Rami Al Nazer

FLEXIBLE MULTIBODY SIMULATION APPROACH IN THE DYNAMIC ANALYSIS OF BONE STRAINS DURING PHYSICAL ACTIVITY

Thesis for the degree of Doctor of Science (Technology) to be presented with due permission for public examination and criticism in Auditorium 1382 at Lappeenranta University of Technology, Lappeenranta, Finland on the 29th of August, 2008, at noon.

Acta Universitatis
Lappeenrantaensis
313

Supervisor	Professor Aki Mikkola Department of Mechanical Engineering Lappeenranta University of Technology Finland
Reviewers	Professor Jaime Domínguez Department of Mechanical Engineering University of Seville Spain
	Professor Viktor Berbyk Department of Applied Mechanics Chalmers University of Technology Sweden
Opponents	Professor Jaime Domínguez Department of Mechanical Engineering University of Seville Spain
	Professor Viktor Berbyk Department of Applied Mechanics Chalmers University of Technology Sweden

ISBN 978-952-214-611-3
ISBN 978-952-214-612-0 (PDF)
ISSN 1456-4491

Lappeenrannan teknillinen yliopisto
Digipaino 2008

ABSTRACT

Rami Al Nazer

Flexible Multibody Simulation Approach in the Dynamic Analysis of Bone Strains during Physical Activity

Lappeenranta, 2008
132 p.
Acta Universitatis Lappeenrantaensis 313
Diss. Lappeenranta University of Technology
ISBN 978-952-214-611-3, ISBN 978-952-214-612-0 (PDF), ISSN 1456-4491

The objective of this study is to show that bone strains due to dynamic mechanical loading during physical activity can be analysed using the flexible multibody simulation approach. Strains within the bone tissue play a major role in bone (re)modeling. Based on previous studies, it has been shown that dynamic loading seems to be more important for bone (re)modeling than static loading. The finite element method has been used previously to assess bone strains. However, the finite element method may be limited to static analysis of bone strains due to the expensive computation required for dynamic analysis, especially for a biomechanical system consisting of several bodies. Further, *in vivo* implementation of strain gauges on the surfaces of bone has been used previously in order to quantify the mechanical loading environment of the skeleton. However, *in vivo* strain measurement requires invasive methodology, which is challenging and limited to certain regions of superficial bones only, such as the anterior surface of the tibia.

In this study, an alternative numerical approach to analyzing *in vivo* strains, based on the flexible multibody simulation approach, is proposed. In order to investigate the reliability of the proposed approach, three 3-dimensional musculoskeletal models where the right tibia is assumed to be flexible, are used as demonstration examples. The models are employed in a forward dynamics simulation in order to predict the tibial strains during walking on a level exercise. The flexible tibial model is developed using the actual geometry of the subject's tibia, which is obtained from 3-dimensional reconstruction of Magnetic Resonance Images. Inverse dynamics simulation based on motion capture data obtained from walking at a constant velocity is used to calculate the desired contraction trajectory for each muscle. In the forward dynamics simulation, a proportional derivative servo controller is used to calculate each muscle force required to reproduce the motion, based on the desired muscle contraction trajectory obtained from the inverse dynamics simulation. Experimental measurements are used to verify the models and check the accuracy of the models in replicating the realistic mechanical loading environment measured from the walking test. The predicted strain results by the models show consistency with literature-based *in vivo* strain measurements. In conclusion, the non-invasive flexible multibody simulation approach may be used as a surrogate for experimental bone strain measurement, and thus be of use in detailed strain estimation of bones in different applications. Consequently, the information obtained from the present approach might be useful in clinical applications, including optimizing implant design and devising exercises to prevent bone fragility, accelerate fracture healing and reduce osteoporotic bone loss.

Keywords: flexible multibody dynamics, bone, strain estimation, MRI
UDC 621.8 : 004.942 : 621.766

ACKNOWLEDGEMENTS

The research work of this thesis was carried out in the Institute of Mechatronics and Virtual Engineering in the Department of Mechanical Engineering of Lappeenranta University of Technology (LUT) during the years 2006-2008.

I am deeply thankful to have had the opportunity to work with Professor Aki Mikkola. As my principal advisor, Professor Mikkola has been always the source of constant and valuable guidance and advice. His support, experience and cordiality will continue to influence my research work in the years to come. I would like to thank Dr. Asko Rouvinen and Dr. Kimmo Kerkkänen in the Institute of Mechatronics and Virtual Engineering (LUT) for their valuable advices. Special thanks to Dr. Pertti Kolari for his enthusiasm towards my research work and accepting to be a subject for this study. Many thanks to my colleague Timo Rantalainen in the Department of Biology of Physical Activity, University of Jyväskylä,, Professor Ari Heinonen in the Department of Health Sciences, University of Jyväskylä and Professor Harri Sievänen in Bone Research Group, UKK Institute, Tampere, for their fruitful cooperation during my research work.

I would like to thank the reviewers of the thesis, Professor Jaime Domínguez from University of Seville, Spain, and Professor Viktor Berbyk from Chalmers University of Technology, Sweden, for their constructive comments and advices. I would like also to thank all my friends and colleagues in the Institute of Mechatronics and Virtual Engineering. Special thanks to my colleagues Toumas Rantalainen and his family and Adam Klodowski for their assistant and help. I would like to thank my dearest friends Ali Halabia, Mohammad Al Manasrah and Kristine Jepremjana for their support and encouragement.

Finally, and most importantly, I am very grateful to my family for their love and support. My father Abdullah for being a constant source of support and encouragement. My mother Taghreed, unfortunately there is no word in this world can be capable of expressing my deepest appreciation and warmest thanks for your patience and lovely caring. My brothers Romel, Ramez, Mohammad and lovely sister Raya, comprehensive thanks are not possible, but every one of you knows how much endless love and greatest respect for him/her I have in my heart.

Lappeenranta, 25th of July, 2008 Rami Al Nazer

CONTENTS

1. INTRODUCTION 15
- 1.1. Scope of the Work and Outline of the Dissertation 23
- 1.2. Contribution of the Dissertation 24

2. STRAIN ANALYSIS IN MULTIBODY DYNAMICS 26
- 2.1. Description of Coordinates 31
- 2.2. Component Mode Synthesis 33
- 2.3. Kinematics Description of the Flexible Body 38
- 2.4. Inertia and Force Description of the Flexible Body 39
- 2.5. Equations of Motion of the Biomechanical Model 43

3. MULTIBODY MUSCULOSKELETAL MODELING 46
- 3.1. Skeletal Model 47
- 3.2. Joints and ligaments 50
- 3.3. Muscles 51
- 3.4. Simulation Procedure 53
- 3.5. Limitations of the Anatomical Components 60

4. NUMERICAL EXAMPLE 62
- 4.1. Description of Normal Human Walking 62
- 4.2. Experimental Subjects 63
- 4.3. Description of the Introduced Biomechanical Models 64
- 4.4. Human Experiments 75
- 4.5. Numerical Analysis 79
- 4.6. Results 83
- 4.7. Discussion 90
- 4.8. Limitations of the Introduced Biomechanical Models 99
- 4.9. Future Development of the Introduced Biomechanical Models 100

5. CONCLUSIONS 103

REFERENCES 106

APPENDIX A 119

NOMENCLATURE

Abbreviations

ADAMS	Automatic Dynamic Analysis of Mechanical Systems
CAD	Computer Aided Design
DAE	Differential Algebraic Equations
EMG	Electromyographical
FEA	Finite Element Analysis
MRI	Magnet Resonance Images
ODE	Ordinary Differential Equations
CT	Computed Tomography
PCSA	Physiological Cross Sectional Area

Symbols

$\mathbf{A}^{i}$	Transformation matrix of flexible body *i* reference coordinate system with respect to the global coordinate system
$\mathbf{a}^{iN}$	Fixed interface normal vibration modes of flexible body *i*
$\mathbf{b}^{i}$	Orthonormalized Craig-Bampton modes of flexible body *i*
$\mathbf{C}$	Vector of the linearly independent nonlinear constraint equations of the biomechanical model
$\mathbf{C}_{d}^{i}$	Generalized damping matrix of flexible body *i*
$\mathbf{C}_{dd}^{i}$	Diagonal modal damping matrix of the orthonormalized Craig-Bampton modes of flexible body *i*
$\mathbf{C}_{\mathbf{q}}$	Jacobian matrix
c^{i*}	Critical damping ratios of the orthonormalized Craig-Bampton modes of flexible body *i*

$\mathbf{D}^i$	kinematics matrix describing the strain-displacement relationship
$\mathbf{e}^i$	Vector of the nodal coordinates of flexible body *i*
$\mathbf{F}_e^{iP}$	Vector of the external force acting on an arbitrary node on flexible body *i*
$\mathbf{F}_f^i$	Vector of the external force associated with the nodal coordinates of flexible body *i*
$F_{muscle,\max}$	Maximum allowable muscle force
$\overline{\mathbf{G}}^i$	Matrix that depends on the Euler angles
$\mathbf{I}$	Identity matrix
$\mathbf{K}^i$	Generalized stiffness matrix of flexible body *i*.
$\mathbf{K}_{CB}^i$	Modal stiffness matrix of the non-orthogonal Craig-Bampton modes of flexible body *i*
$\mathbf{K}_f^i$	Finite element stiffness matrix associated with the nodal coordinates of flexible body *i*
$\mathbf{K}_{pp}^i$	Diagonal modal stiffness matrix of the orthonormalized Craig-Bampton modes of flexible body *i*
k	Number of nodes in element *j* in flexible body *i*
L_k^{ij}	Volume coordinates for element *j* in flexible body *i*
$\mathbf{M}^i$	Generalized mass matrix of flexible body *i*
m^i	Mass of flexible body *i*
m^{iP}	Mass of an arbitrary node on flexible body *i*
$\mathbf{m}_{CB}^i$	Modal mass matrix of the non-orthogonal Craig-Bampton modes of flexible body *i*
$\mathbf{m}_f^i$	Finite element mass matrix associated with the nodal coordinates of flexible body *i*
$\mathbf{m}_{pp}^i$	Diagonal modal mass matrix of the orthonormalized Craig-Bampton modes of flexible body *i*

m	Number of the selected orthonormalized Craig-Bampton modes of flexible body *i*
N_k^{ij}	Shape function of the degrees of freedom of node *k* in element *j*
n	Number of nodal coordinates of flexible body *i*
n_f	Number of total nodes of flexible body *i*
$\mathbf{p}^i$	Vector of the modal coordinates associated with the orthonormalized Craig-Bampton modes of flexible body *i*
P^i	Arbitrary node on flexible body *i*
$\mathbf{Q}_d^i$	Vector of the damping forces associated with the derivative of the generalized coordinates of flexible body *i*
$\mathbf{Q}_e^i$	Vector of the external forces associated with the generalized coordinates of flexible body *i*
$\mathbf{Q}_s^i$	Vector of the elastic forces associated with the generalized coordinates of flexible body *i*
$\mathbf{Q}_v^i$	Quadratic velocity vector of flexible body *i*
$\mathbf{q}$	Vector of the generalized coordinates of the total bodies in the biomechanical model
$\mathbf{q}^i$	Vector of the generalized coordinates of flexible body *i*
$\mathbf{q}_r^i$	Vector of the reference coordinates of flexible body *i*
$\mathbf{R}^i$	Vector of the translational coordinates of flexible body *i* coordinate system with respect to the global coordinate
$\mathbf{r}^{iP}$	Vector describing the position of any arbitrary node on flexible body *i* with respect to the global coordinate system
t	time
$\bar{\mathbf{u}}^{iP}$	Vector describing the position of any arbitrary node on flexible body *i* with respect to the body reference coordinate system

$\bar{\mathbf{u}}_f^i$	Vector describing the translational deformed position of all nodes on flexible body *i* with respect to the body reference coordinate system
$\bar{\mathbf{u}}_f^{iP}$	Vector describing the deformed position of an arbitrary node on flexible body *i* with respect to the body reference coordinate system
$\bar{\mathbf{u}}_o^{iP}$	Vector describing the undeformed position of any arbitrary node on flexible body *i* with respect to the body reference coordinate system
u_k^{ij}	Translation of node *k* in x^{ij} direction
V^i	Volume of flexible body *i*
V^{ij}	Volume of element *j* in flexible body *i*
v_k^{ij}	Translation of node *k* in y^{ij} direction
δW_i^i	Virtual work of the inertial forces acting on flexible body *i*
w_k^{ij}	Translation of node *k* in z^{ij} direction
$X_1 X_2 X_3$	Global coordinate system
$X_1^i X_2^i X_3^i$	Flexible body *i* reference coordinate system
$x^{ij} y^{ij} z^{ij}$	Element *j* coordinate system in flexible body *i*

Subscripts

B	Boundary nodal coordinates
I	Interior nodal coordinates
R	Reference translational coordinates of flexible body *i*
θ	Reference rotational coordinates of flexible body *i*
p	Modal coordinates of flexible body *i*

Greek Letters

$\boldsymbol{\theta}^i$	Vector of rotational coordinates of flexible body *i* reference coordinate system with respect to the global coordinate

$\mathbf{\Phi}^i$	Modal matrix whose columns are the orthonormalized Craig-Bampton modes of flexible body i
$\mathbf{\Phi}_t^i$	Slice from the modal matrix $\mathbf{\Phi}^i$ that corresponds to the translational degrees of freedom of the nodes of flexible body i
$\mathbf{\Phi}_C^i$	Matrix whose columns are the constraint modes of flexible body i
ω^{iN}	Set of eigenvalues or natural frequencies of the fixed interface normal vibration modes of flexible body i
$\mathbf{\Phi}_N^i$	Martrix whose columns are the fixed interface normal modes of flexible body i
$\mathbf{\Phi}_{CB}^i$	Modal matrix whose columns are the Craig-Bampton modes of flexible body i
ω^{i*}	Set of eigenvalues or natural frequencies of the orthonormalized Craig-Bampton modes of flexible body i
$\mathbf{\Phi}_t^{iP}$	Slice from the modal matrix $\mathbf{\Phi}^i$ that corresponds to the translational degrees of freedom of an arbitrary node on flexible body i
$\overline{\boldsymbol{\omega}}^i$	Angular velocity vector defined in flexible body i reference coordinate system
ρ^i	Density of the flexible body i
$\boldsymbol{\lambda}$	Vector of the Lagrange multipliers
$\boldsymbol{\varepsilon}^i$	Strain vector of flexible body i
$\sigma_{muscle,\max}$	Maximum muscle stress
$\varepsilon_{1,2}$	Maximum and minimum principal strains
ε_y	Normal strain in Y direction
ε_z	Normal strain in Z direction
γ_{yz}	Shear strain in YZ plane
$\gamma_{\max}$	Maximum shear strain

1. INTRODUCTION

Models and computer simulations of the human musculoskeletal system have served many purposes in biomechanical research. Numerous models have been used to predict or estimate characteristics of human mechanisms in body movement and simulate surgical treatments. The power of modeling is increasingly recognized in the field of biomechanics with the birth of specialized software in human modeling, providing a realistic and economical set of tools to improve and maintain the skills of healthcare providers and adding a valuable dimension to medical education, training and research. Due to the complexity involved in developing human biomechanical models, their fidelity and consistency with the real physical process they intend to mimic can be considered one of the main challenges [1]. Therefore, using experimental data combined with a human biomechanical model is considered a powerful scientific tool. Experimental data can be used as the source of model input parameters and as an evaluation of the validity of the model. Biomechanical models can replace some of the experimental measurements and provide a reasonable access to parameters, such as the internal forces in the skeleton and muscular actions, which may be difficult to conduct any other way [2]. Moreover, biomechanical models can be used to provide more quantitative explanations and analysis of how the neuromuscular and musculoskeletal systems interact to produce movement [3]. Therefore, mathematical and computational tools in general, and multibody dynamics in particular have been utilized extensively to build biomechanical models. Generally, biomechanical models can be divided into two types; finite element biomechanical models and multibody biomechanical models.

A biomechanical finite element model is developed from the geometrical description and mechanical properties of the anatomical component in order to analyze stress and strain in different anatomical structures, such as bones and tendons. Usually, a finite element biomechanical model requires a detailed geometrical description and mechanical properties of the anatomical component. Therefore, computer techniques such as Magnet Resonance Images (MRI) and Computed Tomography (CT) are commonly used in obtaining the actual geometry of the anatomical components. When a geometrical biomechanical model has been developed based on MRI or CT scans, it can be meshed in order to obtain a finite element model. The finite element biomechanical model can be used to determine interface stresses, deformations, forces, pressures and alignments in biomechanical systems, consisting of structural components like bones, muscles, joints and ligaments. Finite element analysis of biomechanical models can be used in a wide range of medical applications, including the orthopedic domain, bone (re)modeling analysis, studying the fracture process of anatomical structures, and assisting in the design of implants. As an example, Figure 1.1 shows a finite element model of a human femur obtained from successive CT scans, which is used to study the strain distribution during gait in different mechanical loading environments [4].

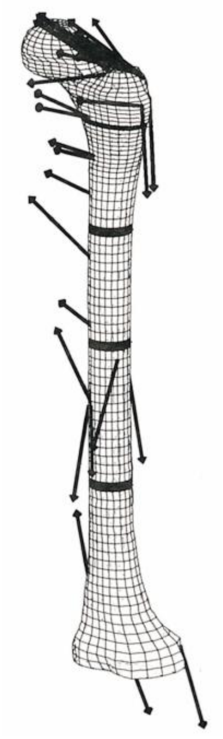

Figure 1.1 Finite element model based on CT scans of a human femur, with thigh muscles represented by arrows [4].

Cheung et al. [5] have developed a 3-dimensional finite element model of the foot and ankle based on MRI to investigate the internal stresses/strains within bones and soft tissues of the ankle and foot under various loadings. Van Rietbergen et al. [6] have developed microfinite element models of healthy and osteoporotic human femurs based on micro CT scans to quantify the strain distribution in femoral heads. The obtained strain distributions are used to establish a safety factor for the femoral trabecular bone. A 3-dimensional finite element model of a human proximal femur based on CT scans is used in the study of Lotz et al. [7] to predict the ultimate failure load based on stress/strain distributions in fall and one legged stance simulations. Karsa and Grynpas [8] have developed a 3-dimensional finite element model of the vertebral trabecular bone in order to study its static and dynamic responses under compressive loading. To study trabecular bone damage accumulation during cyclic compressive loading, a 2-dimensional finite element model of an idealized trabecular bone specimen has been developed in the study of Guo et al. [9]. A 3-dimensional finite element model of an artificial hip implant is used to study the failure of the implant based on stress/strain distribution [10, 11].

It can be concluded from the aforementioned studies that bone strains have been analyzed for various purposes using the finite element method. However, due to the complex geometry of a bone, a finite element model used in stress analysis requires fine element meshes, which in turn leads to a large number of nodal degrees of freedom. For this reason, numerical solutions of models are computationally expensive, limiting the finite element analyses to a piece of bone or a single bone. It is also noteworthy that, due to expensive computation, finite element models are usually applied in a static or short term-dynamic solution. Accordingly, the finite element method is considered computationally impractical to be used in the dynamic analysis of human musculoskeletal models, where number of bones and muscles as well as their interaction need to be taken into consideration.

The multibody dynamic approach is a mathematical tool that can be used to model different mechanical and structural systems. For instance, systems included in the definition of multibody systems comprise robots, manipulators, vehicles, and the human skeleton. The multibody dynamics system has been the focus of intensive research for the past years due to its wide practical applications, including the analysis, design, and control of ground, air, and space transportation vehicles (such as bicycles, automobiles, trains, airplanes, and spacecraft), manipulators and robots, articulated earthbound structures (such as cranes and draw bridges), articulated space structures (such as satellites and space stations) and bio-dynamical systems (such as human body, animals, and insects). Figure 1.2 illustrates a general multibody system shown in an abstract form.

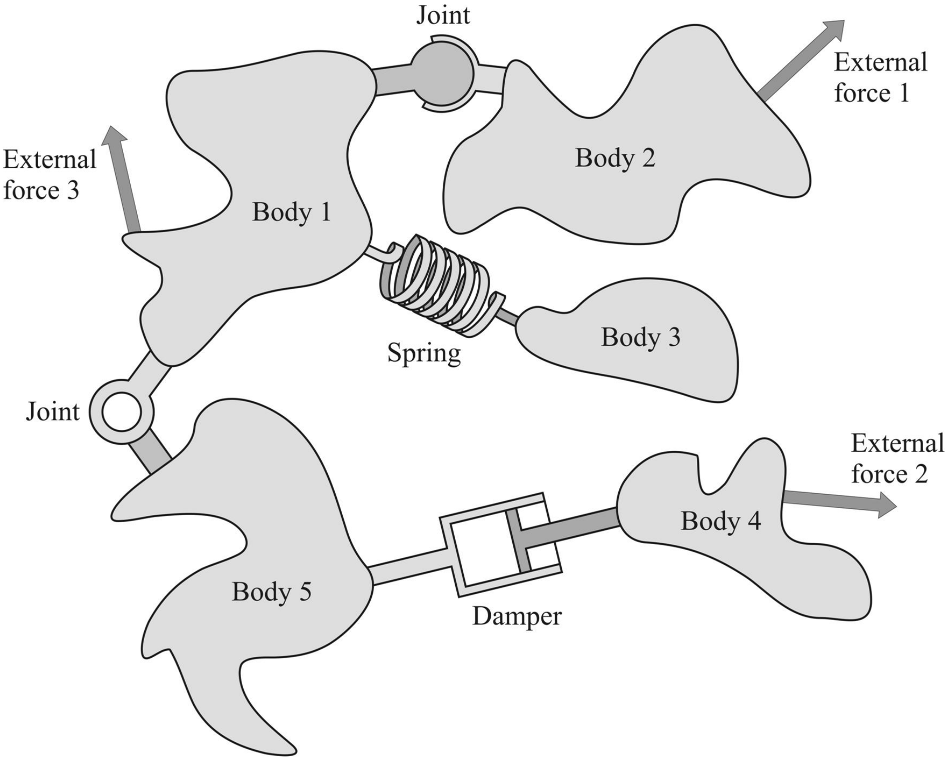
Joint
External
force 1
External
force 3
Body 2
Body 1
Spring
Body 3
Joint
External
force 2
Body 4
Body 5
Damper

Figure 1.2 Sketch of a general multibody system.

It can be seen in Figure 1.2 that a multibody system consists of a number of interconnected bodies, which can be rigid, flexible or both. These bodies are connected together by means of kinematic joints described mathematically by constraint equations. The forces applied over the multibody system bodies may be a result of springs, dampers, actuators or any other externally applied forces, such as gravity. The multibody biomechanical human models are typically more complicated than technical multibody systems, as they involve a larger variety of joint types, body forms and complex actuators in the form of muscles and neighbouring soft tissue [12]. Therefore, many commercial software such as **SIMM** [13] have been developed based on multibody dynamics theories in order to enhance the development of biomechanical modeling. For example, Figure 1.3 shows a graphic representation of a full body human musculoskeletal model, which has been developed based on a multibody dynamics commercial software [14] and is used to simulate riding a bicycle.

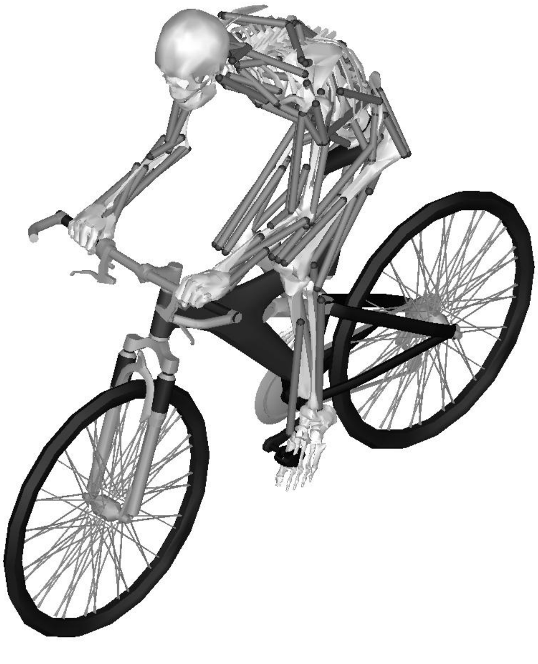

Figure 1.3 Graphic representation of a full body human musculoskeletal model used in the simulation of riding a bicycle.

Biomechanical models based on multibody dynamics have been used widely in the analysis of human physical activities, such as jumping, kicking, running, walking and many other exercises in sports science, medicine and orthopedics [15]. Anderson and Pandy [16] have developed a 3-dimensional human model consisting of 10 rigid bodies actuated by 54 muscles, to simulate maximal vertical jump. A 3-dimensional human skeletal model consisting of 16 rigid bodies with 35 degrees of freedom has been developed by Nagano et al. [17] to simulate a motion similar to the flight phase of a horizontal jump. In the work of Sasaki and Neptune [18], the forward dynamics of 2-dimensional musculoskeletal human model consisting of seven rigid bodies and 15 Hill-type musculotendon actuators at each leg is used to identify differences in muscle function between walking and running at the preferred transition speed. In the study of Bei and Fregly [19], a musculoskeletal multibody knee model consisting of two rigid bones and one deformable contact surface has been created to predict muscle forces and contact pressures in the knee joint simultaneously during gait. Multibody biomechanical models have been applied to passive human motion analysis in order to study different injury scenarios, such as these observed in impact or fall down situations. For example, Silva at al. [20] have studied the injury scenarios for a human head with impact simulation of different vehicle crash situations and the offside tackle of an athlete, using a 3-dimensional biomechanical model consisting of 12 rigid bodies coupled by 11 kinematic joints with passive torque applied at each joint. The biomechanical model described in the previous study of Silva et al. [20] is used in the work of Ambrósio and Silva [21] to investigate the whiplash injury scenario for three occupants in a roll over of an all-terrain vehicle simulation.

Multibody biomechanical models have been used widely in the analysis of the biomechanical consequences of surgical reconstructions, such as joint replacements and tendon transfer. Delp [22] has developed a 3-dimensional musculoskeletal lower extremity model consisting of seven rigid bodies and 43 muscles, to study the biomechanical consequences of surgical reconstructions of the lower extremity. In order to predict the motions of knee implants during a step-up activity, a 3-dimensional musculoskeletal model consisting of six rigid bodies with 21 degrees of freedom and 13 musculotendon actuators has been developed in the study of Piazza and Delp [23].

In all of the aforementioned studies, the bones are assumed to be rigid bodies, a fact that makes these models impractical for bone strain analysis. In this study, a flexible multibody simulation approach which couples the finite element method with multibody dynamics is used to predict the dynamic bone strains during physical activity. The proposed approach overcomes the expensive computation of the dynamic analysis of the biomechanical model using the finite element method. This is an important issue as dynamic bone strains rather than static strains play the primary role in the bone (re)modeling process [24, 25, 26, 27]. For this reason, the dynamic analysis of bone strains can provide a better elucidation of the bone's functional adaptation to mechanical loading environment stimuli. A schematic representation to illustrate the idea of the proposed approach, which can be of use in the dynamic bone strain analysis, is shown in Figure 1.4.

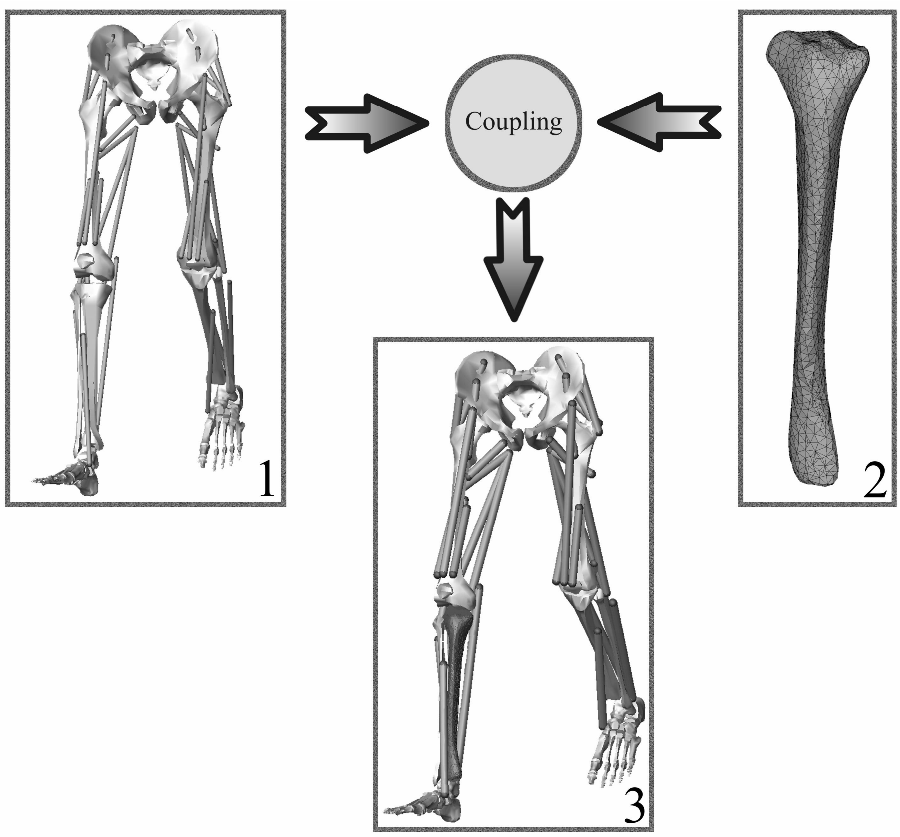

Figure 1.4 Graphic representation of the idea of using the flexible multibody simulation approach in the field of dynamic bone strain analysis; (1) Graphic representation of a rigid multibody biomechanical model, (2) finite element model of a bone and (3) graphic representation of a flexible multibody biomechanical model.

The absolute numbers and age-specific incidence rates of osteoporotic fractures have increased all over the world in recent decades, and without population level intervention, the increasing trend is likely to continue, thus creating a true public health problem for our societies [28]. For example, the number of hip fractures in Finnish people aged 50 or over has tripled between 1970 and 1997 [29]. Although there are several risk factors that affect fracture development, bone strength is considered one of the primary predictors. Thus for preventive and treatment purposes, the ultimate goal is to reduce the risk of fractures by increasing or maintaining the bone strength. Mechanical forces act upon bone by means of joint surfaces or muscles insertions lead to stress and strain in bone tissue. Strains applied to bone can stimulate its development and functional adaptation [30]. It is evident that the bones get stronger if sufficient magnitudes of strain, particularly at a high strain rate and in varying patterns are regularly imposed on the bone [24]. Of all bone traits, a strong bone structure is considered an essential factor in reducing bone fragility [31]. Exercise, in turn, is an efficient means to improve bone strength [32] and reduce fragility fractures [33]. To be specific in devising effective exercise regimes on bones, valid information on incident strain distributions is needed. However, measuring bone strains *in vivo* requires invasive methodology, which is challenging and not feasible for a majority of bones.

1.1. Scope of the Work and Outline of the Dissertation

The objective of this study is to use the flexible multibody dynamics simulation approach to assess dynamic bone strains during physical activity. It is widely known that mechanical tissue strain is an important intermediary signal in the transduction pathway linking the external loading environment to bone maintenance and functional adaptation. This study introduces briefly the theory of flexible multibody dynamics used in dynamic bone strain estimation. To illustrate the use of the flexible multibody simulation approach in bone strain analysis, three 3-dimensional musculoskeletal models are introduced. In the introduced models, the right tibia is assumed to be a flexible body. The flexible tibial model is obtained from a 3-dimensional reconstruction of Magnetic Resonance Images (MRI). The introduced models are used to simulate walking on a level exercise in order to predict the tibial strains. The parametric components used in developing the simulation models introduced in this study are discussed in detail.

This study is organized as follows. In Chapter 2, the flexible multibody formulations available in the literature are discussed briefly. The feasibility of flexible multibody formulations in the analysis of bone strain is explained. The theory of the floating frame of reference, which is used in this study in the estimation of dynamic bone strains, is briefly presented.

In Chapter 3, the anatomical components used in this study to develop a general flexible multibody biomechanical model are explained. The process of developing the finite element model of the bone based on a 3-dimensional reconstruction of MRI is explained. Moreover, the simulation procedure for predicting dynamic bone strains during physical activity is described in detail. The limitations of the anatomical components used to develop a general flexible multibody biomechanical model are also addressed in Chapter 3.

In Chapter 4, the general parametric anatomical components described in Chapter 3 are used to develop the introduced biomechanical models. In the introduced models, the right tibia is assumed to be the flexible body, and the tibial finite element model is generated from a 3-dimensional reconstruction of MRI. The introduced models are used to simulate walking on a level exercise in order to predict the tibial strains. The conducted experimental measurements which are needed either in developing or verifying the introduced biomechanical models are explained. The verification of the introduced models based on the experimental measurements is explained. The reliability of the predicted tibial strains obtained from the introduced models is studied on the basis of the reported literature-based *in vivo* strain measurements. The strain distribution about the cortical cross section at the middle of the tibial shaft during the stance phase is also demonstrated and compared to the literature-based *in vitro* strain measurement study. The limitations and future development of the introduced models are also addressed in Chapter 4. Finally, conclusions are drawn in Chapter 5.

1.2. Contribution of the Dissertation

The original contribution of this dissertation is using the flexible multibody simulation approach in dynamic bone strain analysis during physical activity. The bone strain environment is significant in the process of bone (re)modeling control and bone stimulation due to mechanical loadings. Therefore bone strains are considered to be a primary factor in the bone strengthening process. Based on previous studies, it has been shown that dynamic strains rather than static strains are the primary stimulus of the functional adaptation of a bone. Finite element biomechanical models have been used previously to assess bone strains. Due to computational reasons, however, dynamic analysis of the bone strains using the finite element method may be impractical, especially for a biomechanical system consisting of several bodies interconnected with each other. On the other hand, rigid multibody biomechanical models are limited to the dynamic analysis of rigid bodies where the flexibility of the bones can not be accounted for. In order to fill the gap and overcome the limitations that render the finite element method and rigid multibody dynamics unfeasible for dynamic bone strain analysis, the floating frame of reference formulation is used in estimating dynamic bone strains. The proposed approach to estimate dynamic bone strains overcomes also problems associated with experimental strain measurements. This is due to the fact that *in vivo* implementation of strain gauges on the surfaces of bone is a challenging, highly invasive technique and not feasible for the majority of bones. The approach presented in this dissertation may be utilized in a wide range of medical applications including, bone remodelling analysis, optimizing the exercise regime, and pre-clinical testing of implants against damage accumulation failure scenarios.

The author has proposed the simulation procedure method and created the introduced models as demonstration examples to perform the strain analysis for the bones. The finite element models of the bones were based on Magnetic Resonance Images which were acquired in the central hospital of Lappeenranta and Jyväskylä. The human experiments required as input parameters (i.e., motion capture) and to verify the introduced models (i.e., ground reaction force and Electromyographical muscle activity measurements) were carried out at the University of Jyväskylä with the help of the stuff of the Neuromuscular Research Center.

2. STRAIN ANALYSIS IN MULTIBODY DYNAMICS

In structures in general, strain plays a crucial role in understanding and defining material behavior and the elucidation of structural behavior and design. Bone can be considered to be a living tissue that can adapt its structure and geometry to its mechanical loading environment in order to maintain the skeletal mechanical integrity. Therefore, deformation of bone, which can be quantified as bone strain, is significant to the process of bone (re)modeling control and bone stimulation due to mechanical loadings. As a conclusion, bone strain is considered to be a fundamental factor in studying the effectiveness of the exercise regime in stimulating bone mass [34]. It is important to emphasize that bone adaptation is driven by dynamic rather than static loading [24, 25, 26, 27]. Therefore, in this study the bone strains are obtained from a dynamic analysis of the multibody biomechanical model. The deformations and corresponding strains of a body within a multibody system can be studied using four approaches:

1. The nonlinear finite element approach [35, 36].
2. The approach based on the linear theory of elastodynamics [35].
3. The lumped mass approach [37].
4. The approach based on the floating frame of reference formulation [35].

In the first approach, nonlinear finite element formulations, such as the absolute nodal coordinate formulation [35] and large rotational vector formulation [36] are embedded in the multibody formalism in order to describe the mechanical flexibility. Absolute nodal coordinate and large rotational vector formulations can be used efficiently in the large deformation and rotation analysis of a flexible multibody system that undergoes an arbitrary reference displacement [35, 36, 38, 39]. The absolute nodal coordinate formulation has been developed recently based on the finite element formulation, and is basically devoted for large deformation analysis of flexible multibody system. Authors have applied the absolute nodal coordinate formulation to 3-dimensional beam elements [40, 41] and 3-dimensional shell elements [42]. Absolute nodal coordinate formulation represents a departure from the conventional finite element formulations used in engineering analysis. In the formulation, slopes and positions are used as the nodal coordinates instead of infinitesimal or finite rotations. Beam and plate elements based on the absolute nodal coordinate formulation can describe large rigid body rotations exactly unlike the classical beam and plate finite elements that may not lead to accurate modeling of the rigid body dynamics. Using slopes and displacements as nodal coordinates avoids the cumbersome interpolation of rotational coordinates while no assumptions are made with regard to the magnitude of the deformation within the element. The advantages of using the absolute nodal coordinate formulation in the dynamic analysis of flexible multibody systems are its simplicity in describing some of the joint constraints and formulating the generalized forces. In addition, this formulation leads to a simple expression of the inertia forces in two and three dimensional cases leading to constant representation of mass matrix. The constant mass matrix simplifies the nonlinear equations of motion. The large rotational vector formulation has been the subject of extensive research for over two decades. The formulation has been successfully applied into nonlinear analysis of, for example, lightweight space structures. The formulation is based on the large displacement and rotation theory. In case of beam elements based on the large rotational vector formulation, the rotations of the cross section and global displacements of the centreline can be used as nodal coordinates. In this formulation, the element nodal coordinates are defined with respect to the global coordinate system which gives them a clear physical meaning. This also simplifies the description of the inertia of the element. The cross section or fiber rotation within an element can be approximated through the use of interpolation polynomials. Unlike the absolute nodal coordinate formulation, in 3-dimensional case the large rotational vector formulation does not lead to a constant mass matrix. The use of finite rotations as nodal coordinates can lead to numerical difficulties in representing the large rotation of the cross section of the finite element [38]. Accordingly, large rotation vector formulations can lead to singularity problems when slender structures are considered. [43].

The first approach can also be of use in the dynamic simulation of a small deformation of a flexible multibody system that undergoes an arbitrary reference displacement [38, 39]. However, for a body with a complex geometry, such as bone, where the discretization results in a large number of nodal degrees of freedom, the method may be considered computationally expensive [36]. This is attributed to the fact that the dimensionality (i.e., degrees of freedom) of the problem can not be reduced, as the deformation of a flexible body can not be expressed using the deformation mode shapes [35, 36]. The shape of the bone is highly irregular and complex. Therefore, dynamic analysis of a biomechanical model consisting of interconnected flexible and rigid bones using the first approach can be considered unfeasible due to the expensive computation. Further, the finite element model of the bone used in strain analysis is usually based on 3-dimensional reconstruction of MRI or CT scans in order to obtain the exact geometry of the bone. In addition, the finite element model of the bone is usually discretized with solid elements which correspond more realistically to the nature of the bone structure than beam and shell elements. Discretization of the finite element model of the bone using solid elements can not be achieved using the first approach, because it is limited to flexible bodies that can be modeled using beam and shell elements only [36].

In the second approach, based on the linear theory of elastodynamics, the response of the flexible body is calculated by uncoupling rigid body motion and elastic deformation. To this end, the flexible multibody system is first assumed to be a collection of rigid bodies in order to solve for the inertia and reaction forces, based on the analysis of rigid bodies using general purpose multibody computer programs. To account for the deformation of the bodies, the inertia and reaction forces obtained from the analysis of rigid bodies are applied to a linear elasticity problem. The final response of the system can be obtained by superimposing the deformation on the rigid motion of the body. Dynamic bone strains could be calculated using the linear theory of elastodynamics. However, in this approach, the deformation of the body is assumed to be small and has a negligible effect on the rigid body motion. Accordingly, the inertia terms in the reference equations are assumed to be independent of the elastic deformation [43]. In other words, in this approach the deformation and large rigid body motion are not coupled, possibly leading to an unnatural solution. In the linear theory of elastodynamics, the boundary conditions defined in the finite element model and used in the calculation of the deformation must correspond to the constraint equations of the rigid body calculation. For this reason, the boundary conditions may be laborious to define in practical problems so that they accurately represent the constraint equations used in the multibody system simulation.

In the lumped mass approach, the flexible body is idealized into several mass elements. Spring elements are placed between these masses to account for flexibility. Each of the mass elements can be considered as a rigid body, a response which can be obtained from the equations of motion. The stiffness of each spring located between each mass element can be usually obtained using the finite element method. In the lumped mass approach, the use of deformation modes to study the flexibility of the body is not possible. Therefore, this approach can be considered to be computationally expensive for a flexible body with complicated geometry, such as bone, as the flexible body has to be idealized with a large number of mass elements connected by springs in order to obtain accurate deformation.

The approach based on the floating frame of reference formulation is currently the most widely used method in the computer simulation of flexible multibody systems. It is implemented in several commercial as well as research general purpose multibody computer programs. Multibody dynamics with floating frame of reference formulation can be used in the analysis of flexible bodies that undergo large reference displacements; rotational and translational, with small deformations [35]. The configuration of the flexible body in the floating frame of reference is described using a mixed set of absolute reference and local deformation coordinates. In this approach, the classical linear finite element is embedded in the multibody formalism. Unlike the first and third approaches, the size of the problem can be reduced in the floating frame of reference formulation by using deformation mode shapes and assuming that during the motion a few modes are significant. While the first approach is limited to bodies that can be modeled using shell and beam elements only, the floating frame of reference does not suffer from this limitation, as solid elements can be used as well. In contrast to the approach based on the linear theory of elastodynamics, the rigid body motion and deformations are coupled in the floating frame of reference method, which makes it suitable for more general applications. The main feature of the approach based on the floating frame of reference formulation as compared to the other approaches is the use of a reference frame. The use of the reference frame makes it possible to couple deformations and large reference motions in the inertia description of the flexible body. Thus the deformations of the flexible body can be assumed to be linear with respect to the reference frame. The assumption makes it possible to use modal coordinates instead of nodal coordinates in the description of flexible body deformations, where the number of modal coordinates is much smaller than that of nodal coordinates. Consequently, the computational cost decreases drastically with a minimum deterioration of accuracy [35]. It is noteworthy that the floating frame of reference formulation can be used to model nonlinear deformations. The methods used to account for the nonlinear deformation in the floating frame of reference formulation can be categorized into two groups [44]. The first group is based on the substructring technique [45]. To account for the geometric elastic nonlinearity, the flexible body can be divided into substructures where a local reference coordinate system is employed for each substructure. Each substructure is assumed to experience small strain, and the deformation of each substructure is modeled using combinations of normal vibration and static correction modes. Consequently, the original floating frame of reference formulation is preserved. However, the previous method has two disadvantages. First, the number and size of the substructures must be chosen such that the linear elasticity theory has to remain valid within each substructure. Second, defining the compatibility constraints between adjacent substructures might be laborious, particularly, in case where the adjacent substructures are connected at multiple points. The second group is based on including nonlinear terms in the description of the stiffness matrix of the flexible body [44]. These nonlinear terms result from preserving the quadratic terms in the strain-displacement relationship. In case of linear deformation assumption, these terms are neglected. As a result of the nonlinear terms contribution to the strain-displacement relationship, the strain energy function will lead to the definition of the nonlinear geometric stiffness matrix. It is important to note that the concept of the component mode synthesis can not be used when the stiffness matrix is nonlinear.

As a conclusion, in a multibody system where the geometries of the bodies are complicated and small deformations are expected with large displacements, the floating frame of reference formulation may be the best choice [36]. Human bones have complex shapes, and during a variety of movements, the bones experience large translational and rotational displacements while strains within the bones remain small – of the order of 3000 microstrain at maximum [46]. Therefore, in this study, the multibody simulation approach with the floating frame of reference formulation is used as a procedure in the prediction of dynamic bone strains during physical activity. In the following sections of this chapter, the theory of the floating frame of reference is presented briefly. The components of the equations of motion of a flexible body (i.e., bone) are shown only.

2.1. Description of Coordinates

The deformation of the flexible body in the floating frame of reference formulation can be described using various discretization techniques, while in this study, the deformation is described using the finite element approach. Floating frame of reference is based on the use of two coordinate systems; reference and nodal coordinate systems. Figure 2.1 shows the floating frame of reference coordinate systems used in the description of a spatial flexible body *i*.

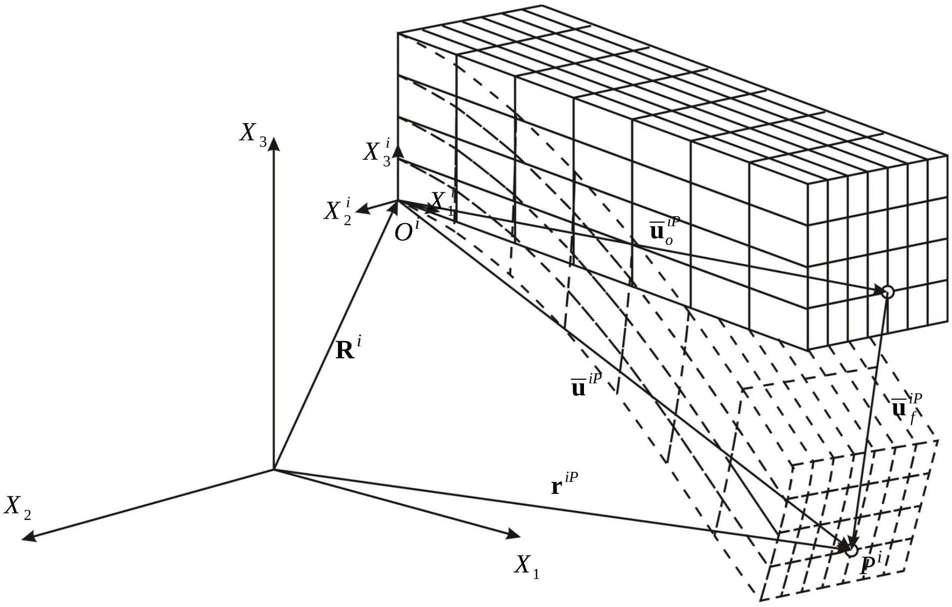

Figure 2.1 Coordinates for spatial flexible body *i* in the floating frame of reference formulation.

The position of an arbitrary node P^i on flexible body *i* shown in Figure 2.1 can be expressed with respect to the global coordinate system as follows:

$$\mathbf{r}^{iP} = \mathbf{R}^i + \mathbf{A}^i \bar{\mathbf{u}}^{iP} = \mathbf{R}^i + \mathbf{A}^i (\bar{\mathbf{u}}_o^{iP} + \bar{\mathbf{u}}_f^{iP}), \tag{2.1}$$

where $\mathbf{R}^i$ is the vector which describes the translation of flexible body *i* reference coordinate system $X_1^i X_2^i X_3^i$ with respect to the global coordinate system $X_1 X_2 X_3$ and $\mathbf{A}^i$ is the transformation matrix which describes the rotation of flexible body *i* reference coordinate system with respect to the global coordinate system. The matrix, $\mathbf{A}^i$, can be expressed using the three independent Euler angles [35]. In Eq (2.1), $\bar{\mathbf{u}}^{iP}$ is the vector which describes the translational position of node P^i with respect to flexible body *i* reference coordinate system, $\bar{\mathbf{u}}_o^{iP}$ and $\bar{\mathbf{u}}_f^{iP}$ are the vectors which describe the translational undeformed and deformed position of node P^i with respect to flexible body *i* reference coordinate system, respectively. Hereafter, superscript i denotes the flexible body (i.e., bone).

2.2. Component Mode Synthesis

In case the geometry of the flexible body is complex, such as bone, the finite element model results with a large number of nodal degrees of freedom, which makes it computationally expensive to define the deformations in time domain analyses. This computational problem can be alleviated using component mode synthesis [47]. As a result, the deformation of the flexible body can be described using deformation shape modes instead of nodal coordinates. The dimensionality of the flexible body finite element model (i.e., degrees of freedom) can be reduced by using only m deformation modes, where $m << n$ (nodal coordinates). This, in turn, reduces the computational effort drastically without a significant loss of accuracy [35]. A reduced order model of the flexible body can be described using m deformation modes as follows [32]:

$$\bar{\mathbf{u}}_f^i = \mathbf{\Phi}_t^i \mathbf{p}^i , \tag{2.2}$$

where $\bar{\mathbf{u}}_f^i$ is the vector which describes the translational deformed position of all nodes on the flexible body with respect to the body reference coordinate system, $\mathbf{\Phi}_t^i$ is the modal transformation matrix whose columns are the selected m deformation modes associated with the translational degrees of freedom of all nodes of the flexible body and $\mathbf{p}^i$ is the vector of the modal coordinates associated with the deformation modes. In the floating frame of reference formulation, the deformation due to the nodal rotation can be neglected, since it has insignificant effect in the deformation of the flexible body. However, the nodal rotational degrees of freedom can be taken into account in the definition of the constraints of the flexible body. The deformation modes have to be selected with care, as they should be capable to describe the behaviour of the system accurately. There are a number of methods to select the m deformation modes, while in this study the strain energy method [48] is used to select the significant deformation modes of the flexible body. The deformation modes defined in Eq (2.2) can be obtained either by eigenvalue analysis of the finite element model or by using experimentally identified modes [49]. In this study, the deformation modes defined in Eq (2.2) are obtained using eigenvalue analysis based on the Craig-Bampton method with the orthonormalization procedure [50], which yields the orthonormalized Craig-Bampton modes. As a result of using the component mode synthesis in the floating frame of reference formulation, the generalized coordinates of the flexible body can be defined as follows:

$$\mathbf{q}^i = \begin{bmatrix} \mathbf{q}_r^{iT} & \mathbf{p}^{iT} \end{bmatrix}^T = \begin{bmatrix} \mathbf{R}^{iT} & \boldsymbol{\theta}^{iT} & \mathbf{p}^{iT} \end{bmatrix}^T, \tag{2.3}$$

where $\mathbf{q}_r^i$ is the vector of reference coordinates, which describes the large displacements (i.e., rigid motion; translational $\mathbf{R}^i$ and rotational $\boldsymbol{\theta}^i$) of the flexible body reference coordinate system with respect to the global coordinate system. In the Craig-Bampton method, the vector of the nodal coordinates of the flexible body finite element model is partitioned into boundary and interior nodal coordinates. The equation of motion based on the flexible body finite element model can be defined as follows:

$$\mathbf{m}_f^i \ddot{\mathbf{e}}^i + \mathbf{K}_f^i \mathbf{e}^i = \mathbf{F}_f^i, \tag{2.4}$$

where $\mathbf{e}^i$ is the vector of the nodal coordinates of the flexible body resulting from the body descritization into a finite number of elements, $\mathbf{m}_f^i$ and $\mathbf{K}_f^i$ are the finite element mass and stiffness matrices associated with the nodal coordinates of the flexible body, respectively, and $\mathbf{F}_f^i$ is the vector of the external force associated with the nodal coordinates of the flexible body. Based on the Craig-Bampton partitioning, Eq (2.4) can be expressed in the following form:

$$\begin{bmatrix} \mathbf{m}_{BB}^i & \mathbf{m}_{BI}^i \\ \mathbf{m}_{IB}^i & \mathbf{m}_{II}^i \end{bmatrix} \begin{bmatrix} \ddot{\mathbf{e}}_B^i \\ \ddot{\mathbf{e}}_I^i \end{bmatrix} + \begin{bmatrix} \mathbf{K}_{BB}^i & \mathbf{K}_{BI}^i \\ \mathbf{K}_{IB}^i & \mathbf{K}_{II}^i \end{bmatrix} \begin{bmatrix} \mathbf{e}_B^i \\ \mathbf{e}_I^i \end{bmatrix} = \begin{bmatrix} \mathbf{F}_{fB}^i \\ \mathbf{F}_{fI}^i \end{bmatrix}, \tag{2.5}$$

where subscripts B and I correspond to the boundary and interior nodal coordinates, respectively. The Craig-Bampton method results in two sets of modes; non-orthogonal constraint modes and orthogonal fixed interface normal modes. The constraint modes describe deformation due to unit displacements of boundary nodal coordinates and can be obtained from a static equilibrium analysis of the flexible body finite element model expressed in Eq (2.5). As a result of applying a static equilibrium analysis, Eq (2.5) can be expressed in the following form:

$$\begin{bmatrix} \mathbf{F}^i_{fB} \\ \mathbf{F}^i_{fI} \end{bmatrix} = \begin{bmatrix} \mathbf{K}^i_{BB} & \mathbf{K}^i_{BI} \\ \mathbf{K}^i_{IB} & \mathbf{K}^i_{II} \end{bmatrix} \begin{bmatrix} \mathbf{e}^i_B \\ \mathbf{e}^i_I \end{bmatrix}. \tag{2.6}$$

The constraint modes can be extracted from Eq (2.6), assuming that the interior forces equal to zero as follows:

$$\begin{bmatrix} \mathbf{F}^i_{fB} \\ \mathbf{0} \end{bmatrix} = \begin{bmatrix} \mathbf{K}^i_{BB} & \mathbf{K}^i_{BI} \\ \mathbf{K}^i_{IB} & \mathbf{K}^i_{II} \end{bmatrix} \begin{bmatrix} \mathbf{e}^i_B \\ \mathbf{e}^i_I \end{bmatrix}. \tag{2.7}$$

Consequently:

$$\mathbf{e}^i_I = \left[-\mathbf{K}^i_{II} \right]^{-1} \mathbf{K}^i_{IB} \mathbf{e}^i_B = \mathbf{\Phi}^i_C \mathbf{e}^i_B, \tag{2.8}$$

where $\mathbf{\Phi}^i_C$ is the mode matrix whose columns are the non-orthogonal constraint modes. On the other hand, the fixed interface normal modes describe vibration modes when fixed boundary conditions are applied at all the boundary nodal coordinates. The fixed interface normal modes can be obtained by solving an eigenvalue analysis of Eq (2.5) as follows:

$$\left[-(\omega^{iN})^2 \mathbf{m}^i_{II} + \mathbf{K}^i_{II} \right] \mathbf{a}^{iN} = \mathbf{0}, \tag{2.9}$$

where ω^{iN} is a set of eigenvalues or natural frequencies associated with eigenvectors $\mathbf{a}^{iN}$. These eigenvectors are called fixed interface normal modes. The combination of the constraint modes and fixed interface normal modes yields the non-orthogonal Craig-Bampton deformation modes. Assembling the non-orthogonal Craig-Bampton modes in a matrix yields a mode matrix whose columns are the non-orthogonal Craig-Bampton modes as follows:

$$\mathbf{\Phi}^{i}_{CB} = \begin{bmatrix} \mathbf{I} & \mathbf{0} \\ \mathbf{\Phi}^{i}_{C} & \mathbf{\Phi}^{i}_{N} \end{bmatrix}, \tag{2.10}$$

where $\mathbf{\Phi}^{i}_{N}$ is the mode matrix whose columns are the fixed interface normal modes obtained from Eq (2.9). It is essential to emphasize here that the non-orthogonal Craig-Bampton modes expressed in Eq (2.10) are not orthogonal with respect to the finite element mass and stiffness matrices. As a result, the modal mass and stiffness matrices of the non-orthogonal Craig-Bampton modes will contain non-zero off-diagonal terms. For this reason, the coupling between the generalized elastic coordinates can not be removed. An important issue that should be taken into account when selecting the deformation modes is that the modes must be defined in one reference coordinate system [51]. The Craig-Bampton modes containing the constraint and vibration modes described in Eq (2.8) and Eq (2.9), respectively, may be defined using different reference coordinate systems. Therefore, the Craig-Bampton modes defined in Eq (2.10) should be used with care in the floating frame of reference formulation. The orthonormalization procedure can be applied to the non-orthogonal Craig-Bampton modes in order to enforce them as orthogonal. The orthonormalization procedure can be accomplished by solving the following eigenvalue analysis:

$$\left[-(\omega^{i*})^{2}\mathbf{m}^{i}_{CB} + \mathbf{K}^{i}_{CB}\right]\mathbf{b}^{i} = \mathbf{0}, \tag{2.11}$$

where ω^{i*} is a set of eigenvalues or natural frequencies associated with eigenvectors $\mathbf{b}^{i}$. These eigenvectors are the selected *m* orthonormalized Craig-Bampton modes of the flexible body. In Eq (2.11), $\mathbf{m}^{i}_{CB}$ and $\mathbf{K}^{i}_{CB}$ are the modal mass and stiffness matrices of the non-orthogonal Craig-Bampton modes, respectively. The matrices are not diagonal matrices and they can be expressed respectively as follows:

$$\mathbf{m}^i_{CB} = \mathbf{\Phi}^{iT}_{CB}\mathbf{m}^i_f\mathbf{\Phi}^i_{CB} . \tag{2.12}$$

$$\mathbf{K}^i_{CB} = \mathbf{\Phi}^{iT}_{CB}\mathbf{K}^i_f\mathbf{\Phi}^i_{CB} . \tag{2.13}$$

It can be noticed from Eq (2.11) that the orthonormalized Craig-Bampton modes represent the eigenvectors of the Craig-Bampton representation of the finite element model. As a result of the orthonormalization procedure, the original physical description of the Craig-Bampton modes defined in Eq (2.10) is changed. Consequently, the resulting orthonormalized Craig-Bampton modes will include approximate free-free modes (i.e., modes of the unconstrained body) and the vibration modes of the boundary degrees of freedom. The orthonormalized Craig-Bampton modes resulting from the orthonormalization procedure expressed in Eq (2.11) can be assembled in a matrix. This modal matrix can be defined as follows:

$$\mathbf{\Phi}^i = \begin{bmatrix} \mathbf{b}^i_1 & \cdots & \mathbf{b}^i_m \end{bmatrix} , \tag{2.14}$$

where $\mathbf{\Phi}^i$ is the modal transformation matrix whose columns are the selected m orthonormalized Craig-Bampton modes. It is worth noting that the modal transformation matrix $\mathbf{\Phi}^i_t$ defined in Eq (2.2) is a slice from the modal transformation defined in Eq (2.14) that corresponds only to the translational degrees of freedom of the nodes, while the modal matrix $\mathbf{\Phi}^i$ corresponds to the translational and rotational degrees of freedom of the nodes of the flexible body. The orthonormalized Craig-Bampton modes defined in Eq (2.14) can be normalized with respect to the mass matrix expressed in Eq (2.12). Consequently, the diagonal mass and stiffness matrices can be expressed in the following forms:

$$\mathbf{m}^i_{pp} = \mathbf{\Phi}^{iT}\mathbf{m}^i_{CB}\mathbf{\Phi}^i = \mathbf{I}_{(m\times m)} , \tag{2.15}$$

$$\mathbf{K}^{i}_{pp} = \mathbf{\Phi}^{iT}\mathbf{K}^{i}_{CB}\mathbf{\Phi}^{i} = \begin{bmatrix} \omega_1^{i2*} & & 0 \\ & \ddots & \\ 0 & & \omega_m^{i2*} \end{bmatrix}, \tag{2.16}$$

where $\mathbf{m}^{i}_{pp}$ and $\mathbf{K}^{i}_{pp}$ are the diagonal modal mass and stiffness matrices of the orthonormalized Craig-Bampton modes, respectively.

2.3. Kinematics Description of the Flexible Body

The biomechanical multibody model presented in this study consists of interconnected rigid and flexible bodies. In computer aided analysis of such a heterogeneous system, it is desirable to use a formulation that yields the rigid body inertia properties exactly [52]. In order to obtain the exact rigid body inertia properties (i.e., the mass, the mass moment of inertia and the moment of mass) of the flexible body, the equations of motion of the flexible body are defined with respect to the fixed global coordinate system [52]. Thus, Eq (2.1) can be rewritten using the generalized coordinates of the flexible body described in Eq (2.3) as follows:

$$\mathbf{r}^{iP} = \mathbf{R}^{i} + \mathbf{A}^{i}(\bar{\mathbf{u}}^{iP}_{o} + \mathbf{\Phi}^{iP}_{t}\mathbf{p}^{iT}), \tag{2.17}$$

where $\mathbf{\Phi}^{iP}_{t}$ is the modal transformation matrix whose columns are the selected m deformation modes which are associated with the translational degrees of freedom of node P^{i} on the flexible body. The global velocity equation of node P^{i} can be obtained by differentiating Eq (2.17) with respect to time, which yields the following:

$$\dot{\mathbf{r}}^{iP} = \dot{\mathbf{R}}^{i} - \mathbf{A}^{i}\tilde{\bar{\mathbf{u}}}^{iP}\bar{\mathbf{G}}^{i}\dot{\boldsymbol{\theta}}^{i} + \mathbf{A}^{i}\mathbf{\Phi}^{iP}_{t}\dot{\mathbf{p}}^{iT} = \dot{\mathbf{R}}^{i} - \mathbf{A}^{i}(\tilde{\bar{\mathbf{u}}}^{iP}_{o} + \tilde{\mathbf{h}})\bar{\mathbf{G}}^{i}\dot{\boldsymbol{\theta}}^{i} + \mathbf{A}^{i}\mathbf{\Phi}^{iP}_{t}\dot{\mathbf{p}}^{iT}, \tag{2.18}$$

where $\tilde{\bar{\mathbf{u}}}^{iP}$ is the skew symmetric matrix of vector $\bar{\mathbf{u}}^{iP}$, $\tilde{\bar{\mathbf{u}}}^{iP}_{o}$ is the skew symmetric matrix of vector $\bar{\mathbf{u}}^{iP}_{o}$ and $\bar{\mathbf{G}}^{i}$ is the matrix that can be used to define the relation between the angular velocity vector defined in the flexible body reference coordinate system and the time derivative of the rotational coordinates of the flexible body reference coordinate system with respect to the global coordinate system as follows:

$$\bar{\boldsymbol{\omega}}^i = \bar{\mathbf{G}}^i \dot{\boldsymbol{\theta}}. \tag{2.19}$$

In Eq (2.18), $\tilde{\mathbf{h}}$ is the skew symmetric matrix of vector $\mathbf{h}$. Vector $\mathbf{h}$ can be defined as follows:

$$\mathbf{h} = \mathbf{\Phi}_t^{iP} \mathbf{p}^{iT}. \tag{2.20}$$

The velocity vector defined in Eq (2.18) can be described in a partitioned form as follows:

$$\dot{\mathbf{r}}^{iP} = \begin{bmatrix} \mathbf{I} & -\mathbf{A}^i \tilde{\bar{\mathbf{u}}}^{iP} \bar{\mathbf{G}}^i & \mathbf{A}^i \mathbf{\Phi}_t^{iP} \end{bmatrix} \begin{bmatrix} \dot{\mathbf{R}}^i \\ \dot{\boldsymbol{\theta}}^i \\ \dot{\mathbf{p}}^i \end{bmatrix}, \tag{2.21}$$

where $\mathbf{I}$ is the 3×3 identity matrix. Differentiating Eq (2.21) with respect to time yields the global acceleration equation of node P^i. Using the relations expressed in this section, the global acceleration equation of node P^i can be expressed in the following form:

$$\ddot{\mathbf{r}}^{iP} = \ddot{\mathbf{R}}^i + \mathbf{A}^i \tilde{\bar{\boldsymbol{\omega}}}^i \tilde{\bar{\boldsymbol{\omega}}}^i (\bar{\mathbf{u}}_o^{iP} + \mathbf{\Phi}_t^{iP} \mathbf{p}^i) + \mathbf{A}^i \tilde{\dot{\bar{\boldsymbol{\omega}}}}^i (\bar{\mathbf{u}}_o^{iP} + \mathbf{\Phi}_t^{iP} \mathbf{p}^i) + 2\mathbf{A}^i \tilde{\bar{\boldsymbol{\omega}}}^i \mathbf{\Phi}_t^{iP} \dot{\mathbf{p}}^i + \mathbf{A}^i \mathbf{\Phi}_t^{iP} \ddot{\mathbf{p}}^i. \tag{2.22}$$

2.4. Inertia and Force Description of the Flexible Body

In this section, the inertia and force description of the flexible body are expressed by employing the principle of the virtual work of the inertial forces, $\delta W_i^i = \int_{V^i} \rho^i \delta \mathbf{r}^{iT} \ddot{\mathbf{r}}^i dV^i$, where ρ^i and V^i are the density and volume of the flexible body, respectively.

Description of Inertia

The generalized mass matrix of the flexible body can be defined using the expression of the virtual work of the inertial forces [35] as follows:

$$\mathbf{M}^i = \begin{bmatrix} \mathbf{m}^i_{RR} & \mathbf{m}^i_{R\theta} & \mathbf{m}^i_{Rp} \\ & \mathbf{m}^i_{\theta\theta} & \mathbf{m}^i_{\theta p} \\ symmetric & & \mathbf{m}^i_{pp} \end{bmatrix}, \tag{2.23}$$

where the subscripts R, θ and p denote the reference translational, rotational and modal coordinates, respectively, of the flexible body. The sub-matrices of the generalized mass matrix $\mathbf{M}^i$ defined in Eq (2.23) can be expressed as follows:

$$\mathbf{m}^i_{RR} \cong \sum_{P=1}^{n_f} \mathbf{m}^{iP}_{RR} \cong m^i \mathbf{I}, \tag{2.24}$$

$$\mathbf{m}^i_{R\theta} \cong \sum_{P=1}^{n_f} \mathbf{m}^{iP}_{R\theta} \cong \sum_{P=1}^{n_f} - m^{iP} \mathbf{A}^i \tilde{\bar{\mathbf{u}}}^{iP} \bar{\mathbf{G}}^i, \tag{2.25}$$

$$\mathbf{m}^i_{Rp} \cong \sum_{P=1}^{n_f} \mathbf{m}^{iP}_{Rp} \cong \sum_{P=1}^{n_f} m^{iP} \mathbf{A}^i \mathbf{\Phi}^{iP}_t, \tag{2.26}$$

$$\mathbf{m}^i_{\theta\theta} \cong \sum_{P=1}^{n_f} \mathbf{m}^{iP}_{\theta\theta} \cong \sum_{P=1}^{n_f} m^{iP} \bar{\mathbf{G}}^{iT} \tilde{\bar{\mathbf{u}}}^{iP^T} \tilde{\bar{\mathbf{u}}}^{iP} \bar{\mathbf{G}}^i, \tag{2.27}$$

$$\mathbf{m}^i_{\theta p} \cong \sum_{P=1}^{n_f} \mathbf{m}^{iP}_{\theta p} \cong -\sum_{P=1}^{n_f} m^{iP} \bar{\mathbf{G}}^{iT} \tilde{\bar{\mathbf{u}}}^{iP^T} \mathbf{\Phi}^{iP}_t, \tag{2.28}$$

$$\mathbf{m}^i_{pp} \cong \sum_{P=1}^{n_f} \mathbf{m}^{iP}_{pp} \cong \sum_{P=1}^{n_f} m^{iP} \mathbf{\Phi}^{iP^T}_t \mathbf{\Phi}^{iP}_t = \mathbf{I}_{(m\times m)}, \tag{2.29}$$

where n_f is the number of nodes of the flexible body, m^i is the mass of the flexible body and m^{iP} is the mass of node P^i on the flexible body.

Generalized Forces

The generalized forces acting on node P^i on the flexible body can be divided into three types; external forces, elastic forces and damping forces. The external forces are produced by the muscles, ligaments, contact and gravity. The elastic forces are due to the deformation of the flexible body, while the damping forces are due to the viscoelasticity property of the flexible body (i.e., bone). Viscoelasticity of the bone can arise from a variety of mechanisms at different structural scales of the bone [53]. Viscoelasticity includes phenomena, such as creep, relaxation, and dynamic response. In this study, the dynamic strains of the bone occurring during physical activities are the point of interest. Therefore the influence of the viscoelasticity of the bone on the dynamic response under different types of loading that can be imposed on the bone is taken into account by defining critical damping ratios for the deformation modes of the bone. The principle of virtual work can be used to obtain the equations of the generalized forces [35]. The vector of the external forces acting on node P^i, and associated with the generalized coordinates of the flexible body can be expressed as follows:

$$\mathbf{Q}_e^i = \mathbf{F}_e^{iP} \left[\mathbf{I} \quad -\mathbf{A}^i \tilde{\bar{\mathbf{u}}}^{iP} \overline{\mathbf{G}}^i \quad \mathbf{A}^i \mathbf{\Phi}_t^{iP} \right]^T, \tag{2.30}$$

where $\mathbf{F}_e^{iP}$ is the vector of the external forces acting on node P^i on the flexible body. The vector of the elastic forces associated with the generalized coordinates of the flexible body can be expressed as follows:

$$\mathbf{Q}_s^i = -\mathbf{q}^{iT} \mathbf{K}^i, \tag{2.31}$$

where $\mathbf{K}^i$ is the generalized stiffness matrix of the flexible body, which can be defined as follows:

$$\mathbf{K}^i = \begin{bmatrix} 0 & 0 & 0 \\ \vdots & \ddots & \vdots \\ 0 & \cdots & \mathbf{K}_{pp}^i \end{bmatrix}. \tag{2.32}$$

The vector of the damping forces associated with the derivative of the generalized coordinates of the flexible body can be expressed as follows:

$$\mathbf{Q}_d^i = -\dot{\mathbf{q}}^{iT}\mathbf{C}_d^i, \tag{2.33}$$

where $\mathbf{C}_d^i$ is the generalized damping matrix of the flexible body, which can be defined as follows:

$$\mathbf{C}_d^i = \begin{bmatrix} 0 & 0 & 0 \\ \vdots & \ddots & \vdots \\ 0 & \cdots & \mathbf{C}_{dd}^i \end{bmatrix}, \tag{2.34}$$

where $\mathbf{C}_{dd}^i$ is the diagonal modal damping matrix of the orthonormalized Craig-Bampton modes of the flexible body. The matrix can be expressed as follows:

$$\mathbf{C}_{dd}^i = \begin{bmatrix} c_1^{i*} & & 0 \\ & \ddots & \\ 0 & & c_m^{i*} \end{bmatrix}, \tag{2.35}$$

where c_m^{i*} is the critical damping ratio associated with the mth orthonormalized Craig-Bampton mode of the flexible body.

Quadratic Velocity Vector

The vector of the quadratic velocity inertia forces, which contains the terms that are quadratic in velocity, such as gyroscopic and Coriolis forces, can be defined using the expression of the virtual work of the inertial forces, and the global acceleration vector defined in Eq (2.22) [35] as follows:

$$\mathbf{Q}_v^i = \left[\left(\mathbf{Q}_v^i\right)_R \quad \left(\mathbf{Q}_v^i\right)_\theta \quad \left(\mathbf{Q}_v^i\right)_p \right]^T, \tag{2.36}$$

where the components of the quadratic velocity vector $\mathbf{Q}_v^i$ defined in Eq (2.36) can be expressed as follows:

$$\left(\mathbf{Q}_v^i\right)_R \cong \sum_{P=1}^{n_f} \left(m^{iP} \mathbf{A}^i \tilde{\overline{\boldsymbol{\omega}}}^i \tilde{\overline{\boldsymbol{\omega}}}^i \overline{\mathbf{u}}^{iP} + 2m^{iP} \mathbf{A}^i \tilde{\overline{\boldsymbol{\omega}}}^i \boldsymbol{\Phi}_t^{iP} \dot{\mathbf{p}}^i \right). \tag{2.37}$$

$$\left(\mathbf{Q}_v^i\right)_\theta \cong \sum_{P=1}^{n_f} \left(-m^{iP} \overline{\mathbf{G}}^{iT} \tilde{\overline{\mathbf{u}}}^{iP^T} \tilde{\overline{\boldsymbol{\omega}}}^i \tilde{\overline{\boldsymbol{\omega}}}^i \overline{\mathbf{u}}^{iP} - 2m^{iP} \overline{\mathbf{G}}^{iT} \tilde{\overline{\mathbf{u}}}^{iP^T} \tilde{\overline{\boldsymbol{\omega}}}^i \boldsymbol{\Phi}_t^{iP} \dot{\mathbf{p}}^i \right). \tag{2.38}$$

$$\left(\mathbf{Q}_v^i\right)_p \cong \sum_{P=1}^{n_f} \left(m^{iP} \boldsymbol{\Phi}_t^{iP} \tilde{\overline{\boldsymbol{\omega}}}^i \tilde{\overline{\boldsymbol{\omega}}}^i \overline{\mathbf{u}}^{iP} + 2m^{iP} \boldsymbol{\Phi}_t^{iP^T} \tilde{\overline{\boldsymbol{\omega}}}^i \boldsymbol{\Phi}_t^{iP} \dot{\mathbf{p}}^i \right). \tag{2.39}$$

2.5. Equations of Motion of the Biomechanical Model

In this study, the equations of motion of the biomechanical model are formulated using an augmented technique based on Lagrange multipliers. The equations of motion of the biomechanical model presented in this study can be expressed as follows [35]:

$$\mathbf{M}\ddot{\mathbf{q}} + \mathbf{C}_d \dot{\mathbf{q}} + \mathbf{K}\mathbf{q} + \mathbf{C}_{\mathbf{q}}^T \boldsymbol{\lambda} = \mathbf{Q}_e + \mathbf{Q}_v, \tag{2.40}$$

where $\mathbf{q}$ is the vector of the generalized coordinates of all bodies in the biomechanical model, $\mathbf{C}_{\mathbf{q}}$ is the Jacobian matrix of the nonlinear constraints equation, and $\boldsymbol{\lambda}$ is the vector of the Lagrange multipliers. Eq (2.40) represents a system of second-order differential equations whose solution must satisfy the algebraic constraint equations during the dynamic simulation. The algebraic constraint equations which describe the mechanical joints of the bodies in the model as well as their specified trajectories can be expressed as follows:

$$\mathbf{C}(\mathbf{q},t)=\mathbf{0}, \tag{2.41}$$

where t is the time and $\mathbf{C}$ is the vector of the linearly independent nonlinear constraint equations of the biomechanical model. Eq (2.40) and Eq (2.41) represent a set of nonlinear differential algebraic equations (DAE), which have to be solved simultaneously. However, an integrator of such a system of equations is still under research and development [35]. The stability convergence and accuracy of the methods used in solving DAE are still not deeply known [36]. Therefore, the set of DAE expressed in Eq (2.40) and Eq (2.41) can be transformed to a set of second ordinary differential equations (ODE), where the accuracy of solving this set of equations and the stability convergence have been the topic of numerous studies [36]. The transformation from DAE to ODE can be accomplished by differentiating the kinematic constraint equations defined in Eq (2.41) twice with respect to time, which yields the following equation:

$$\mathbf{C}_{\mathbf{q}}\ddot{\mathbf{q}}=\mathbf{Q}_c=-\mathbf{C}_{tt}-2\mathbf{C}_{\mathbf{q}t}\dot{\mathbf{q}}-(\mathbf{C}_{\mathbf{q}}\dot{\mathbf{q}})_{\mathbf{q}}\dot{\mathbf{q}}\,. \tag{2.42}$$

As a result, Eq (2.40) and Eq (2.42) can be combined in one matrix equation which can be solved for accelerations and the vector of Lagrange multipliers. The system can be expressed in the following form [35]:

$$\begin{bmatrix}\mathbf{M} & \mathbf{C}_{\mathbf{q}}^{T}\\ \mathbf{C}_{\mathbf{q}} & \mathbf{0}\end{bmatrix}\begin{bmatrix}\ddot{\mathbf{q}}\\ \boldsymbol{\lambda}\end{bmatrix}=\begin{bmatrix}\mathbf{Q}_e+\mathbf{Q}_v-\mathbf{C}_d\dot{\mathbf{q}}-\mathbf{K}\mathbf{q}\\ \mathbf{Q}_c\end{bmatrix}. \tag{2.43}$$

Having solved for the modal coordinates from Eq (2.43), the strain vector of the flexible body, $\boldsymbol{\varepsilon}^{i}$, can be obtained as a post-processing procedure as follows:

$$\boldsymbol{\varepsilon}^i = \mathbf{D}^i \boldsymbol{\Phi}^i \mathbf{p}^i \,, \tag{2.44}$$

where $\mathbf{D}^i$ is the kinematics matrix that describes the strain-displacement relationship. The matrix can be obtained using the shape function matrix. The strain-displacement relationship described by matrix $\mathbf{D}^i$ is assumed to linear. Consequently, the geometric elastic nonlinearity and the material nonlinearity are assumed to be neglected. As regard assuming the geometric elastic nonlinearity to be neglected, it was shown in previous studies [46] that the strain within the bone remains small during different physical activities, in the range of 3000 microstrain at maximum, which validates the assumption. Neglecting the material nonlinearity can be justified for a bone based on the linear load deformation curves obtained in the elastic region for a human femur subjected to uniaxial tension or compression and torsion loading tests [54]. Therefore, based on the previous study of Reilly and Burstein [54], the material law of the bone can be assumed linear in the elastic region. However, for bone fracture analysis, the nonlinear deformation due to large strain and material nonlinearity that accounts for the plastic deformation of the bone upon fracture has to be accounted. In this case, the approach proposed in the study of Ambrósio and Nikravesh [55] might be used for this type of analysis.

3. MULTIBODY MUSCULOSKELETAL MODELING

Multibody musculoskeletal models can be considered as an important tool in the field of biomechanics. The models are broadly used in medicine, orthopedics, ergonomics and sports. The multibody dynamics theory provides a means to study and analyze the behavior of different biomechanical systems, as well as their components. Multibody musculoskeletal models are playing an increasingly significant role in surgical treatment simulation [56]. Surgeons are seeking for tools to support them in the planning phase of surgery treatment and studying the consequences of the treatment prior to its application [57]. The input parameters required in developing musculoskeletal models, such as bone geometry, description of joint kinematics and muscle attachments as well as architecture are typically based on *in vivo* or *in vitro* studies and cadaveric measurements [56]. Most of the model parameters are highly dependent on the individual person's anthropometric data including height, weight, age, ethnicity, size, gender and physical condition [58]. For this reason, scaling and extrapolation techniques are often used in the commercial software specialized in biomechanical modeling to fit the parameters of the model with the specified anthropometric data. Musculoskeletal models based on multibody dynamics have proved to be effective, practical and appealing tools due to ethical and economical reasons. The multibody musculoskeletal model developed by Delp [22] can be used as a training simulator for less experienced surgeons to investigate the effects of surgical decisions on a model rather than a patient. In some cases, it can be more economical to use multibody musculoskeletal models to obtain the required measurements rather than using *in vivo* and/or *in vitro* experimental procedures, for example, to simulate and predict joint response under different loading conditions [59]. Internal forces and strains of the skeleton, as well as muscular actions can be estimated using multibody musculoskeletal models without a need to employ invasive techniques. It is important to note that some physical parameters, such as trabecular bone strains, can be impossible to obtain *in vivo*.

In this chapter, the anatomical components used to develop a general flexible musculoskeletal multibody model which can be utilized in the dynamic analysis of bone strains during physical activity are explained. The anatomical components in addition to the simulation procedure, as well as the limitations of the anatomical components are described in the following sections.

3.1. Skeletal Model

The general shape of the human skeleton can be considered to have a symmetrical pattern [60]. In general, the skeleton has physiological functions, such as generation of blood cells and storing calcium, as well as mechanical functions, such as providing support for the body against external forces (e.g. gravity) and acting as a lever system to transfer forces (e.g. muscular forces) [25]. In human movement modelling, the mechanical functions are of interest. Due to the fact that the skeleton serves as a lever system where the origins and insertions of the muscles are placed, the accurate geometry of the bone is essential for developing an accurate model to predict muscular forces and joint moments. For this reason, in many commercial software specialized in human modelling, such as **BRG.LifeMODE** [14], the skeleton model is developed based on MRI or CT scans. Skeleton models can be scaled according to experimental subject anthropometric variables (height, weight, age, ethnicity and gender). The bones forming the structure of the skeleton model are usually determined according to the scope and objective of the study. For example, if the objective of the study is to investigate the ankle movement during physical activity, the foot may be considered as one segment rather than separating it into different bodies. According to the proposed approach in this study, the bone under strain analysis is assumed to be a flexible body while other bones can be assumed rigid.

Flexible Bone

The flexible multibody simulation approach with the floating frame of reference formulation explained in Chapter 2 can be used to describe the flexibility of the bone. Depending on the type of the strain analysis to be performed, CT scans or MRI data acquisition methods of the geometry of the bone can be employed. Of these two methods, CT scan data acquisition can be considered more general, as it provides information about the inhomogeneous material properties of the bone. It is noteworthy, however, that the CT scan data acquisition method imposes radiation doses on the subject. For this ethical reason, the MRI data acquisition method is used in this study to obtain the geometrical configuration of the bone. Figure 3.1 shows the general 3-dimensional reconstruction process of MRI used to generate the finite element model of a bone.

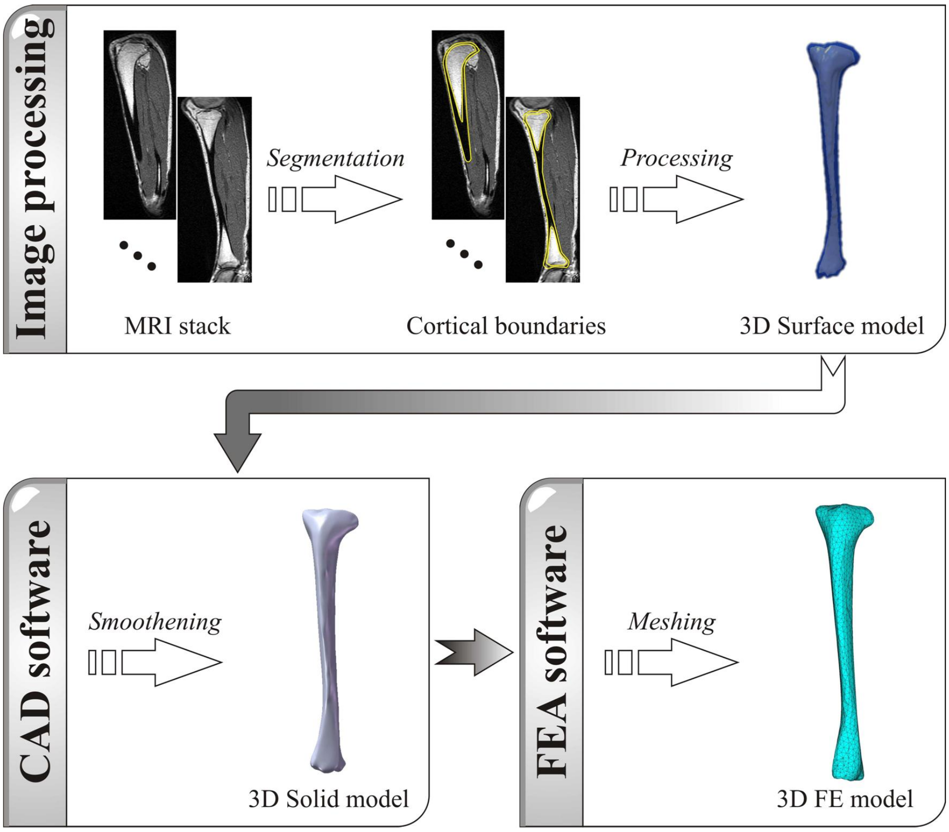
Image processing
Segmentation
Processing
MRI stack
Cortical boundaries
3D Surface model
CAD software
Smoothening
3D Solid model
FEA software
Meshing
3D FE model

Figure 3.1 Generation process of the finite element model of the bone based on 3-dimensional reconstruction of MRI.

As depicted in Figure 3.1, the MRI are segmented using 3-dimensional image processing software, such as **3D-DOCTOR** [61] to define the boundaries of the cortical bone's inner and outer surfaces. The boundary surfaces of the cortical bone are processed to form 3-dimensional surface model of the bone. The 3-dimensional surface model of the bone consisting of inner and outer cortical surfaces can be imported to Computer Aided Design CAD software, such as **SolidWorks** [62] to perform smoothening processes. The smoothening processes are required in order to create a 3-dimensional solid model of the bone suitable for meshing. The 3-dimensional solid model of the bone can be imported to Finite Element Analysis (FEA) software, such as **ANSYS** [63] to describe the finite element model of the bone using solid element. It is essential to note that the solid model of the bone results from the subtraction of the inner volume model of the bone consisting of the inner cortical surface from the outer volume model consisting of the outer cortical surface. For this reason, the subsequent solid cortical layer is represented by a complex irregular thickness which can be only meshed using solid element. Eigenvalue analysis based on the Craig-Bampton method can be performed on the finite element model of the bone in order to obtain the reduced finite element model of the bone, as shown in Figure 3.2.

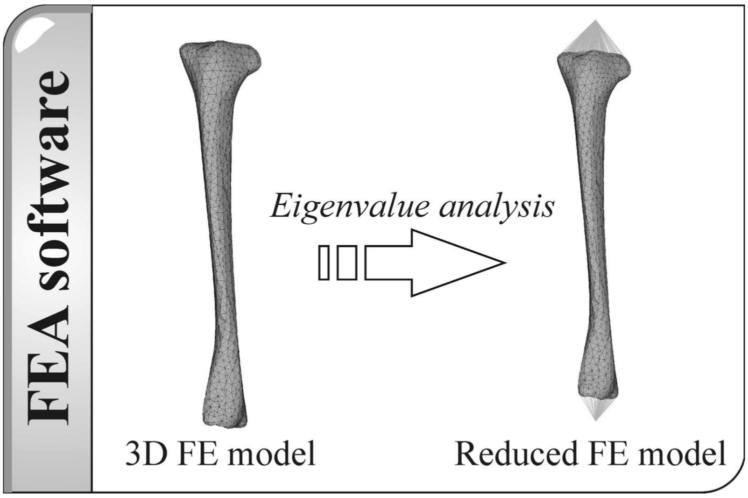

Figure 3.2 Reduced finite element model of the bone to be coupled with the rigid biomechanical model.

As explained in Chapter 2, the reduced finite element model of the bone can be described using the orthonormalized Craig-Bampton deformation modes. In this study, the software (**ANSYS**) is used to obtain the orthonormalized Craig-Bampton modes employed in the floating frame of reference formulation. As a result of the eigenvalue analysis, the nodal coordinates of the finite element model of the bone can be transformed to modal coordinates with the help of the modal transformation matrix of the orthonormalized Craig-Bampton modes, as explained in Eq (2.2). The strain energy method can be used to select the significant orthonormalized Craig-Bampton modes during the forward dynamics simulation of the physical activity [48].

3.2. Joints and ligaments

Joints in musculoskeletal models describe the transformations that relate the position and orientation of one bone to another. In biomechanical models, the anatomical joints can be represented either by kinematic joints (i.e., mechanical joints) or by contact joints (i.e., realistic anatomical joints), depending on the objective of the analysis. However, in most of the biomechanical models used in human movement investigation, the anatomical joints are represented by mechanical joints [3, 15], such as revolute joints for knees and elbows, or spherical joints for hips and shoulders. In this study, the anatomical joints are modeled as mechanical joints which are represented by nonlinear constraint equations relating the coordinates of the bodies connected by such joints. The function of ligaments is basically to guide joint movement and constrain the movement within the allowed physical angular limits of the joint [3, 25]. This function is incorporated in the model by applying a nonlinear torsional spring and torsional damper at each constraint degree of freedom in the model [3]. The magnitude of the applied torsional spring varies with the joint orientation so that it is small at the initial joint orientation to permit joint deformation with minimal resistance, while it increases exponentially near the physical angular limits to protect the joint from exceeding impossible physical angles [16]. In the physical operating range of the joint, the torque varies linearly with the joint orientation [25]. The stiffness of the torques at the physical operating range of the joint can be defined experimentally based on the passive joint response and can be found for some joints such as flexion/extension for hip and elbow joints, in the literature [64, 65]. The damping is included to increase the numerical stability of the model during the forward dynamic simulation [16]. The overall stiffness of the joint is provided by ligaments and muscles as well as cartilage, capsule and menisci. However, cartilage, capsule and menisci are usually not included in multibody biomechanical models used for movement investigations [3]. This can be justified that these structures do not affect the transmission of the muscular forces by the joints [3].

3.3. Muscles

Muscle modeling is an important component of body segmental motion analysis. Several researchers have studied the properties of muscles and their contribution in applying forces to the skeleton [66, 67]. Muscles are responsible of the body movement actuation by developing forces that generate moments about the joints. The muscles are excited and activated by the central nervous system to develop forces which are transmitted to the skeleton by means of tendons. There are a number of models describing the muscle in the literature [68, 69]. Generally, the muscle models available in the literature can be divided into two types: molecular models [70] and phenomenological models [66]. The molecular models describe the muscle force generation process on the sarcomer level, taking into account biophysical/biochemical processes. The phenomenological models describe the muscle actions using parametric mathematical models without the analysis of biophysical/biochemical processes. In multibody biomechanical models used for human movement investigation, molecular muscle models appear to be unfeasible [71]. On the other hand, phenomenological models have proved to be practical in many simulations for human movements [68]. In this study, the muscle is modeled as a contractile active element in series with a viscoelastic element, as shown in Figure 3.3.

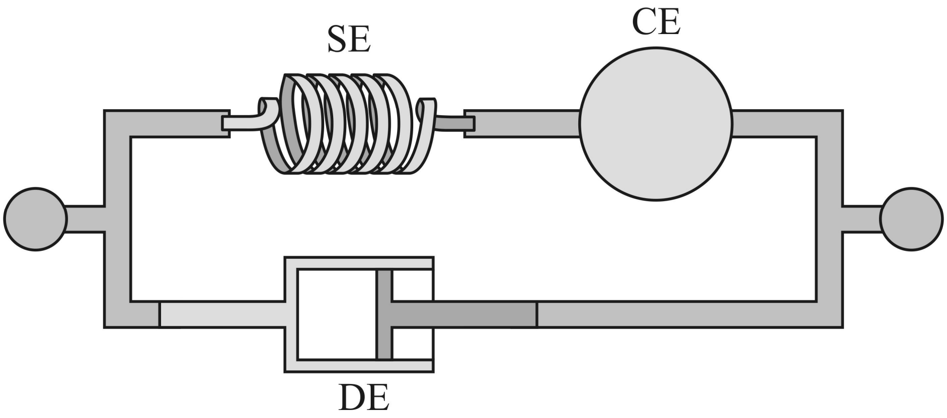

Figure 3.3 Muscle model used in this study. **CE** is the contractile element, **SE** is the spring element and **DE** is the damping element.

In the muscle model shown in Figure 3.3, the viscoelastic element describes the passive behaviour of the muscle. The element is responsible for recording the desired contraction muscle trajectory. The contractile active element describes the activity of the muscle. The element is represented by a proportional derivative servo controller. The controller is used to calculate the muscle force based on the desired muscle contraction trajectory in order to reproduce the motion and keep each muscle force within its allowable physiological limit. The maximum allowable muscle force can be defined as follows [72]:

$$F_{muscle,\,\max} = \text{PCSA} \cdot \sigma_{muscle,\,\max}\,, \tag{3.1}$$

where PCSA is the physiological cross sectional area of the muscle and $\sigma_{muscle,\,\max}$ is the maximum muscle stress. In this study, the maximum muscle stress is assumed to be 87.1 N/cm^2 according to Hatze [73]. The paths of the muscles (i.e., muscle origin and insertion sites) in addition to the physiological cross sectional areas of the muscles are defined according to Eycleshymer and Schoemaker [74] and scaled to the model based on the anthropometric data of the experimental subject.

3.4. Simulation Procedure

The simulation procedure employed in this study to analyse the dynamic bone strains during physical activity is based on the nature of the muscle model used. As explained in this chapter, the muscle model consists of an active contractile element that generates the muscle force based on the recorded desired muscle contraction trajectory. Therefore, the biomechanical model needs a training environment where the desired muscles contraction trajectories for a given movement can be calculated. In this study, inverse dynamics simulation is used to provide such a training environment. In order to perform the inverse dynamics simulation, motion capture of the physical activity under investigation is required. The forward dynamics simulation is vital for the purpose of this study in order to analyze the bone strains in a realistic environment where the muscles are the prime actuators of the model. As a summary, the simulation procedure used in this study comprises both inverse and forward dynamics simulations. Flexible multibody dynamics including inverse and forward dynamics have been used previously in the analysis and design of controllers of flexible multibody systems [49]. The simulation procedure used in this study to predict dynamic bone strains during physical activity consists of the following respective steps.

Motion analysis

The study of biomechanics involves motion analysis. There are a number of methods that can be used to analyze human motion, such as body structure analysis, tracking and recognition [75]. In this study, tracking motion analysis using multiple cameras setup is used to capture the movement. There are a number of advantages in using multiple cameras over a single camera, such as enlarging the area captured [75]. In order to track the human body motion, visual markers are placed on various locations on the subject. This should be accomplished in such a way that the motion capture system is able to track the marker trajectories during the physical activity under investigation. The digitization of the video images and converting them into 3-dimensional coordinates of the markers can be done using a number of software, such as **Peak Motus**. The motion capture data is used to drive the musculoskeletal model through motion agents during the inverse dynamics simulation. The motion agents are massless bodies attached to the model segments at the same locations where the visual markers have been placed on the subject. The motion agent is attached to a segment of the musculoskeletal model using a six degrees of freedom spring damper element. The motion agents are constrained using the marker trajectories which have been recorded via the motion capture. To illustrate the function and configuration of the motion agent in the biomechanical model, a leg flexion/extension activity is given as a demonstration example in Figure 3.4.

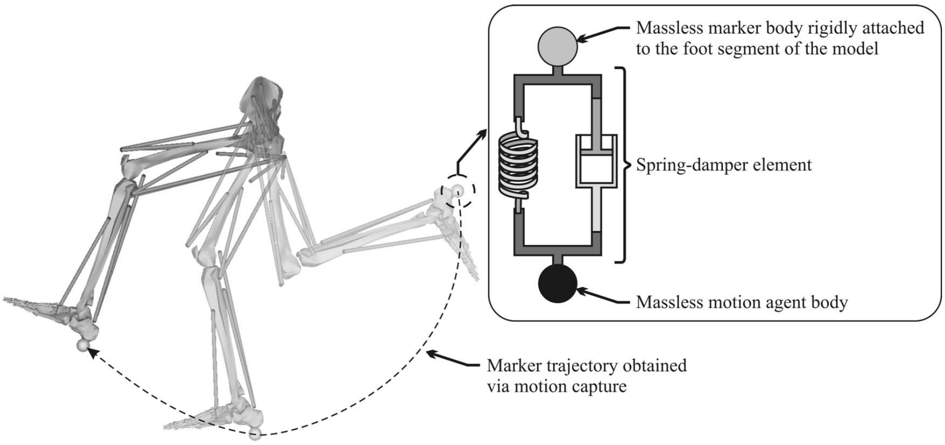
Massless marker body rigidly attached to the foot segment of the model
Spring-damper element
Massless motion agent body
Marker trajectory obtained via motion capture

Figure 3.4 Graphic illustration of the configuration and function of the motion agent for a leg flexion/extension activity driven by a motion agent attached to the foot segment of the biomechanical model during inverse dynamics simulation.

Since motion capture is used to compute the position and orientation of the body segments from the positions of the markers attached to the skin of the subject, accurate marker positions are required. The experimental errors in motion capture can be divided into two major groups. The first group is caused by errors in the capture of the positions of the markers attached to the skin of the subject, and the second group is due to the movement of the skin and consequently of the markers with respect to the underlying bone (skin artefacts) [76]. The first group contains the errors caused by an imperfect calibration of the system. Those errors can be due to image distortions, digitizing of the image, because of the limited resolution of the digital cameras, and human errors in the manual digitizing of the markers. The latter two errors are due to inaccurate determination of the exact location of the centroids of the markers during the digitizing process. This is due to the fact that the marker is seen in the image as a group of a few bright pixels. The second group is considered to be the major source of error in the motion capture [76]. The aforementioned experimental errors in the motion capture can cause large errors in the determination of the position and orientation of the segments and should, therefore, be minimized. There are several techniques used to reduce these errors, such as smoothing the 3-dimensional coordinates of the markers by means of discrete filters and adequate positioning as well as distribution of the markers on the subject to prevent the propagation of the errors. Filtration procedure with the objective of reducing the noise level (i.e., errors) in the motion capture in order to make it suitable for use in the inverse dynamics simulation can be applied using a number of software, such as **MATLAB**.

Inverse dynamics simulation

In inverse dynamics simulation, the applied forces necessary to generate a desired motion response are calculated. The motion of the biomechanical model can be generally acquired using experimental techniques based on video imaging. The muscular forces which are the prime actuators of the body are not considered to be the governors of the motion in inverse dynamics simulation [25]. For this reason, the strains of the bone obtained from inverse dynamics simulation may not be realistic. In the inverse dynamics simulation, the forces of different muscular groups can be lumped as moments about anatomical joints leading to a determinate inverse dynamics problem. The control method applied in the inverse dynamics simulation is the computed torque method [49]. From the joint moments (i.e., torques) and desired muscular contraction trajectories calculated in the inverse dynamics simulation the muscular forces can be obtained. The marker trajectories serve as input for the inverse dynamics simulation that drives the model during the simulation. The marker trajectories are generated from a 3-dimensional reconstruction of the motion capture data of the markers placed at various locations on the subject and tracked during the motion. It is important to emphasize that the model has to be consistent with the kinematic data (i.e., motion capture), and as a consequence, the kinematic constraint equations of the model and their derivatives have to be satisfied during the inverse dynamics simulation. To insure that the model is consistent with the kinematic data, the motion agents are used to drive the model during the inverse dynamics simulation as it is demonstrated in Figure 3.4. These motion agents enforce the degrees of freedom of the joints in the model to follow the marker trajectories obtained via motion capture. An important issue in performing inverse dynamics simulation is the reduction of the experimental errors in motion capture, which were explained previously in this chapter, in order to obtain an accurate performance of the physical activity similar to the measured one.

Forward dynamics simulation

Forward dynamics simulation refers to the computational strategies used to calculate the accelerations, velocities and positions of the generalized coordinates. In forward dynamics simulation, either muscular forces or joint torques are used to actuate the biomechanical model. In this study, muscular forces are used to drive the model in forward dynamics simulation. Muscular forces are selected as actuators instead of the joint torques in order to obtain the dynamic bone strains from a realistic environment simulation where the muscles are the actuators of the model. Furthermore, in coordination studies, it is not recommended to utilize joint torque-actuated models, as such models represent the net effect of muscular forces around the joint. Also, in some cases joint torque-actuated models give a misleading interpretation of the muscle function [3]. In the forward dynamics simulation used in this simulation procedure, the muscular forces calculated in the inverse dynamics simulation are tracked using proportional derivative (PD) servo controllers, in order to guarantee the reproduction of the motion. The PD servo controller minimizes the error between the desired muscle contraction trajectory obtained from the inverse dynamics simulation and the instantaneous one obtained from the forward dynamics simulation at each simulation time step. In addition, it keeps each muscle force within its physiological limit (physiological cross sectional muscle area multiplied by maximum muscle stress). Using the forward dynamics simulation, the musculoskeletal model with flexible bone(s) can be employed to estimate bone deformations due to dynamic loading during physical activity. The significant deformation modes of the flexible bone in the forward dynamics simulation are selected based on the strain energy method. The selected deformation modes are used in the dynamic analysis in order to define the bone strains. Due to the nature of the muscle model used in this study, dynamic optimization techniques used to overcome the muscle redundancy problem can not be used in the forward dynamics simulation. This is due to the fact, that most of the dynamic optimization techniques require activation dynamics to be taken into account in the muscle model, as they are generally based on the search for the neural excitations that drive a forward-dynamics model of the musculoskeletal model to track the prescribed motion, or on the determination of the optimal neural excitations using a systematic procedure to optimize a certain performance of the physical activity [15]. However, in general, dynamic optimization is considered to be computationally expensive as it can solve one optimization problem for one complete cycle of the movement [3, 15]. Therefore, parallel computing is usually used to perform the dynamics optimization [3]. The simulation procedure employed to analyse the dynamic bone strains due to mechanical loading during physical activity is described in the schematic diagram provided in Figure 3.5. The software used at each modeling and simulation step in this study is shown in the schematic diagram provided in Figure 3.6.

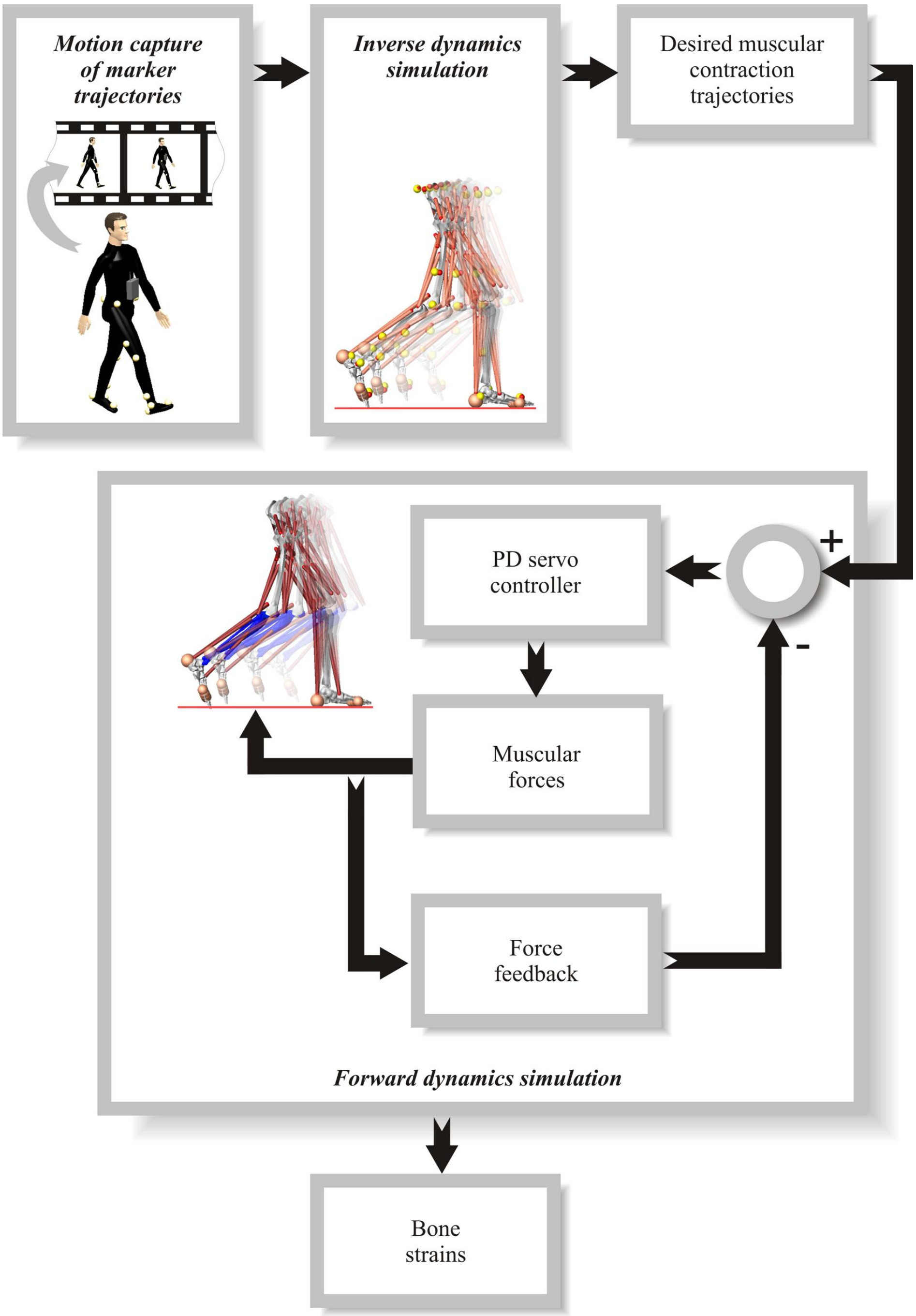
Motion capture of marker trajectories
Inverse dynamics simulation
Desired muscular contraction trajectories
PD servo controller
+
-
Muscular forces
Force feedback
Forward dynamics simulation
Bone strains

Figure 3.5 Schematic diagram of the simulation procedure used in this study.

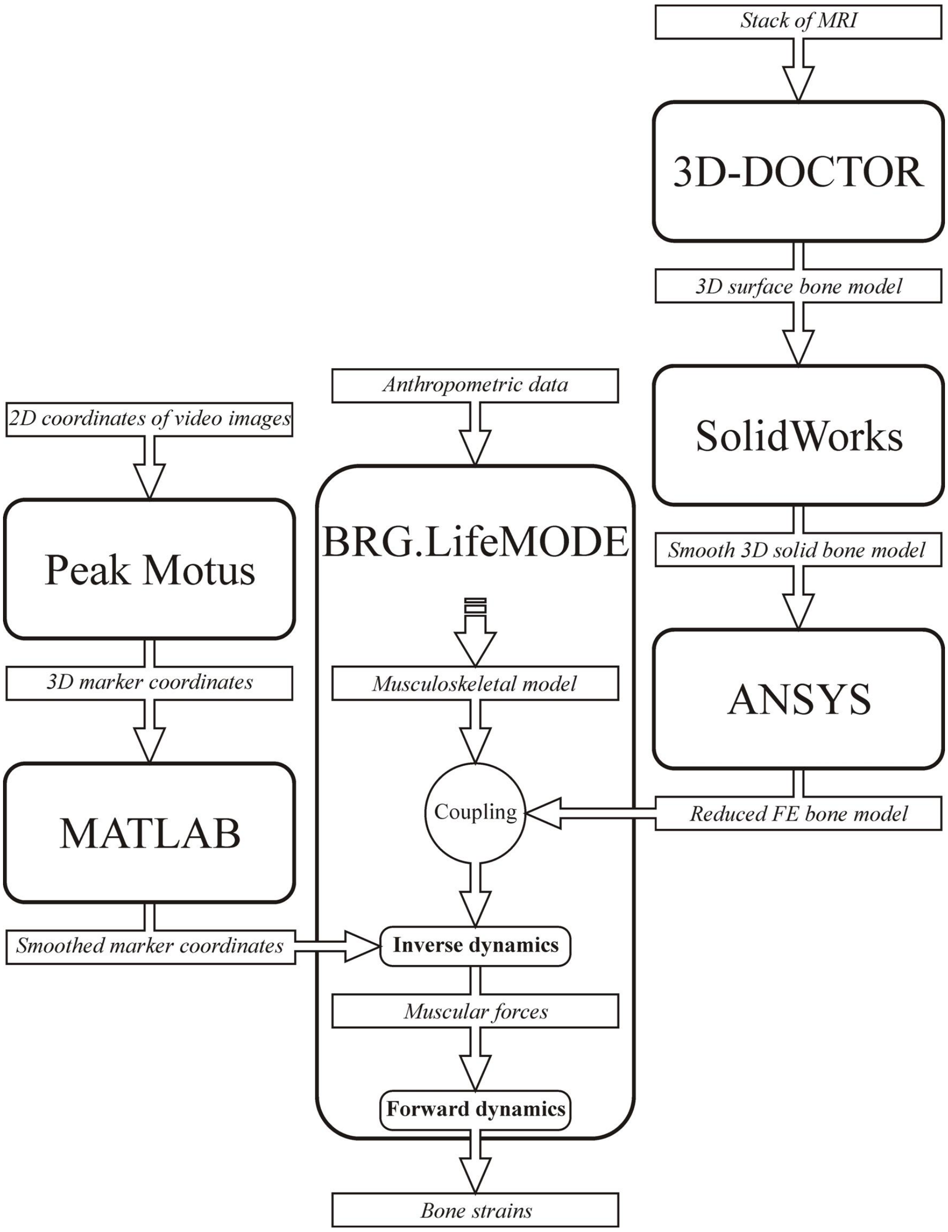
Stack of MRI
3D-DOCTOR
3D surface bone model
SolidWorks
Smooth 3D solid bone model
ANSYS
Reduced FE bone model
Anthropometric data
BRG.LifeMODE
Musculoskeletal model
Coupling
Inverse dynamics
Muscular forces
Forward dynamics
Bone strains
2D coordinates of video images
Peak Motus
3D marker coordinates
MATLAB
Smoothed marker coordinates

Figure 3.6 Schematic diagram of the software used in this study at each modeling and simulation step.

3.5. Limitations of the Anatomical Components

It is essential to reiterate that the anatomical components presented in this chapter can be used to develop a general flexible multibody biomechanical model which can be used in the dynamic analysis of bone strains during physical activity. The accuracy of dynamic bone strain prediction can be further improved by addressing some of the limitations of the presented anatomical components. It is worth noting that these limitations are not related to the objective of this study. The limitations of the anatomical components presented in this chapter can be considered as some of the challenges of developing multibody biomechanical models used in human movement investigation in general. However, these limitations may affect the accuracy of bone strain analysis using the approach proposed in this study. The limitations of the anatomical components can be listed as follows:

1. The accuracy of the biomechanical model generated based on the anatomical components presented in this chapter can be limited by the estimation procedure of muscular forces. This is due to the fact that extensive description of a human musculoskeletal model including the skeleton and many muscle groups for the simulation of human motions still remains an ambitious and challenging task.
2. The simulation procedure employs motion capture of the subject’s body kinematics. This task may not be possible in some environments due to the high costs associated with the measurement systems, or due to technical difficulties, such as external activities.
3. Despite the fact that the anatomical joints in most multibody biomechanical models, as well as the introduced models, used in the human movement investigation, are represented by mechanical joints [3, 15], the usage of the real joint models that describe the complex behaviour of the joints might improve the consistency of the kinematic data (i.e., motion capture) with the model and the compliance of the joints in the dynamic analysis.
4. The inverse dynamics simulation employed by the simulation procedure requires the positions, velocities and acceleration of the segments of the model. The velocities and accelerations of the model segments are the marker trajectories

derivatives, which can be considered a major source of error due to noise amplification in the numerical derivatives. The accumulation error may affect the performance of the inverse dynamics simulation, which in turn affects the accuracy of muscular forces estimation in the forward dynamics simulation. However, in order to avoid noise amplification in the numerical derivatives, the motion capture of the physical activity should be obtained carefully.

5. Another general limitation can arise from the fact that the proposed approach in this study requires employing the forward dynamics simulation for bone strain analysis. This is because the forward dynamics simulation provides a realistic environment in which the muscles are the prime actuators of the model. In some cases where the biomechanical model involves more complex muscle model, the forward dynamics simulation might become expensive, especially in the cases where dynamic optimization techniques are used [3, 76].
6. In this study, the flexible bone is generated based on 3-dimensional reconstruction of MRI. This may limit the definition of the material properties of the bone, as the density and elasticity are assumed to be homogenous, while in reality they are inhomogeneous [25, 77]. This problem can be overcome by using CT scans instead of MRI in the modeling of flexible bones.

4. NUMERICAL EXAMPLE

In this chapter, the accuracy of the flexible multibody simulation approach proposed in this study to analyze dynamic bone strains during physical activity is studied. The anatomical components described in Chapter 3 are used to develop three 3-dimensional musculoskeletal models with a right flexible tibia in each model. The introduced models are applied to simulate walking on a level exercise in order to predict the tibial strains. Walking is chosen as a numerical example because it is the most common daily exercise. The multibody biomechanical models used to simulate walking exercise including verification have been extensively reported in the literature [78]. Further, walking exercise has been the focus of many *in vivo* and *in vitro* strain measurements studies [46, 79, 80, 81, 82, 83], and thus the reliability of the predicted strain results by the introduced models can be easily investigated. The simulated tibial strains are compared with previous *in vivo* tibial strain measurements conducted for walking [46, 79, 80, 81]. The strain distribution around the cortical tibia in the middle of the tibial shaft are also presented and compared with a previous *in vitro* strain measurement study [82]. Experimental measurements of the ground reaction force and Electromyographical (EMG) muscle activity are used to verify the introduced models mimicking capability of the real mechanical loading environment during walking test.

4.1. Description of Normal Human Walking

Normal human walking or human gait gives people a picture of a nearly periodic and symmetric motion, where the patterns occurring in one side of the body repeat in the other side, 180^0 out of phase. This periodic leg movement is the essence of the cyclic nature of human gait. The walking cycle can be divided into phases characterized by the contacts occurring between feet and ground. There are two main phases in the gait cycle [78]: the stance phase starting from the heel strike until the toe-off and the swing phase starting from the toe-off until the heel strike. During the stance phase, the foot is in contact with the ground, whereas in the swing phase that same foot is no longer in contact with the ground and the leg is swinging through in preparation for the next foot strike.

The stance phase can be divided into two sub-phases namely: double support phase and single support phase. In the double support phase both feet are in contact with the ground, and it begins with the heel strike of one foot, and ends with the toe-off of the opposite foot. In the single support phase, only one of the feet is in contact with the ground. The swing phase consists of three sub-phases namely: initial swing, mid-swing and terminal swing. At normal walking speed, the stance phase takes about 62% of the gait cycle period and the swing phase takes approximately 38% of the gait cycle period [78]. At a certain speed, the human will switch from walking to running, where swing phase time becomes more than the stance time for both legs, and the double stance phase completely disappears [76]. An illustration of normal human walking cycle is shown in Figure 4.1.

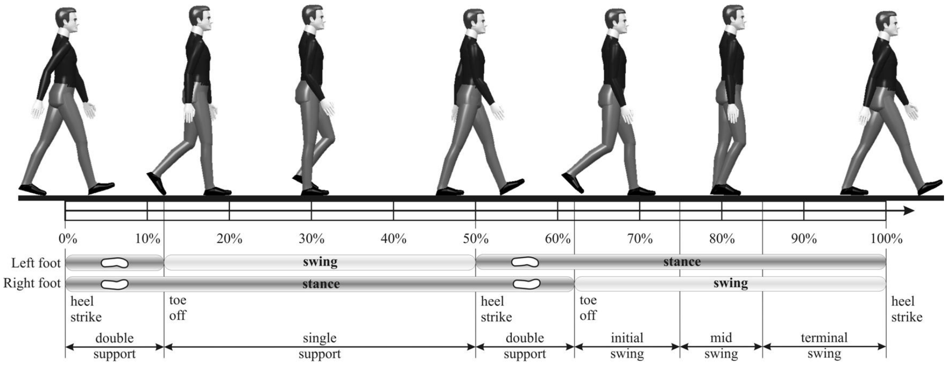
0%
10%
20%
30%
40%
50%
60%
70%
80%
90%
100%
Left foot
Right foot
swing
stance
stance
swing
heel strike
toe off
heel strike
toe off
heel strike
double support
single support
double support
initial swing
mid swing
terminal swing

Figure 4.1 Phases of normal human walking cycle.

4.2. Experimental Subjects

Three healthy voluntary Caucasian men served as subjects for the study. The first subject is 25 years old, 1840 mm in height and with 89 kg mass, the second subject is 52 years old, 1680 mm in height and with 65 kg mass and the third subject is 28 years old, 1770 mm in height and with 84 kg mass. The study is accepted by the local ethical committee in Jyväskylä and the subjects gave a written informed consent. The experiment is conducted according to the Helsinki declaration.

4.3. Description of the Introduced Biomechanical Models

The introduced biomechanical models in this study are developed using the commercial software **BRG.LifeMODE** [14]. The software is based on the commercial multibody software **ADAMS** [84]. The skeleton of the musculoskeletal models is generated from the anthropometric database accessible through the software based on the experimental subject's height, weight, age, ethnicity and gender. Hereafter the first model [85, 86] corresponds to the first subject, the second model [87] corresponds to the second subject and the third model corresponds to the third subject. The first model is represented by a lower body musculoskeletal model, while the second and third models are represented by a full body musculoskeletal model. The first and second models are presented in this chapter, while the third model is presented in Appendix A(I). The third model has completely the same parameters of the second model, however, the third model is generated based on different anthropometric data that corresponds to its subject.

In the first model, the skeleton is modeled using seven segments: lower torso, two thighs, two shanks and two feet. The skeleton of the second model consists of the skeleton segments of the first model with the addition of 12 segments representing the upper body skeleton model: head, neck, upper torso, central torso, two scapulas, two arms, two forearms and two hands. All the segments in the first and second models are assumed to be rigid bodies, except for the tibia at the right shank segment which is assumed to be a flexible body. Figure 4.2 shows the segments used in modeling the skeleton in the introduced models, in addition to the locations of joints. Table 4.1 shows the types of joints used to constrain the segments in the models, in addition to their kinematic description.

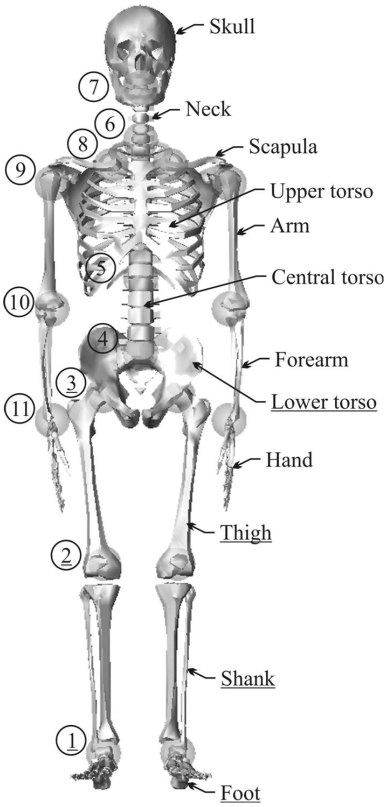
Skull
7
Neck
6
8
Scapula
9
Upper torso
Arm
5
Central torso
10
4
Forearm
3
Lower torso
11
Hand
Thigh
2
Shank
1
Foot

Figure 4.2 Graphic representation of the skeleton model with joint locations represented as centers of the spheres. The underlined segments and joints are used in the first model, while all the segments and joints are used in the second and third models.

Table 4.1 Kinematic constraints in the introduced models.

Joint Number	**Joint Name**	**Type**	**Segments**		**Motion**		
1	Ankle	Universal	Lower torso	Thigh	Flexion /extension	Inversion /eversion	-
2	Knee	Revolute	Shank	Thigh	Flexion /extension	-	-
3	Hip	Spherical	Shank	Foot	Flexion /extension	Abduction /adduction	Rotation
4	Lumbar	Revolute	Lower torso	Central torso	Flexion /extension	-	-
5	Thoracic	Revolute	Central torso	Upper torso	Flexion /extension	-	-
6	Lower neck	Revolute	Upper torso	Skull	Flexion /extension	-	-
7	Upper neck	Fixed	Neck	Skull	-	-	-
8	Scapular	Fixed	Upper torso	Scapula	-	-	-
9	Shoulder	Universal	Scapula	Arm	Flexion /extension	Abduction /adduction	
10	Elbow	Revolute	Arm	Forearm	Flexion /extension	-	-
11	Wrist	Revolute	Forearm	Hand	Flexion /extension	-	-

The torsional stiffness value defined within the physical angular limit of each degree of freedom of the joint in the lower body model is estimated based on the equations defined by Amankwah et al. [64], except for ankle inversion/eversion and hip rotation. For ankle inversion/eversion, a stiffness value of 10000 Nmm/º is used to maintain the stability of the ankle joint in the inverse dynamics simulation, while the stiffness of hip rotation is assumed to be 800 Nmm/º. This numerical value is obtained by studying the angular trajectory responses between the inverse and forward dynamics simulations. In the second model, the torsional stiffness value for the shoulder flexion/extension is estimated based on the study of Zhang et al. [88], for the elbow flexion/extension is estimated based on the study of Lin et al. [65], and for the wrist flexion/extension is estimated based on the study of Leger et al. [89]. The torsional stiffness values for shoulder abduction/adduction and lumbar, thoracic and lower neck flexion/extension are assumed, as they can not be found in the literature. Table 4.2 shows the stiffness and damping values of the joints used in the first and second models.

Table 4.2 Joint stiffness and damping used for the joints in the introduced models.

Joints	**Flexion/extension**		**Inversion/eversion Abduction/adduction**		**Rotation**	
	Stiffness [Nmm/º]	**Damping [Nmms/º]**	**Stiffness [Nmm/º]**	**Damping [Nmms/º]**	**Stiffness [Nmm/º]**	**Damping [Nmms/º]**
Ankle	210	21	10000	1000	-	-
Knee	270	27	-	-	-	-
Hip	700	70	1500	150	800	80
Lumbar	1000	100	-	-	-	-
Thoracic	1000	100	-	-	-	-
Lower neck	1000	100	-	-	-	-
Shoulder	700	70	700	70	-	-
Elbow	60	6	-	-	-	-
Wrist	30	3	-	-	-	-

The first model is actuated by 12 muscle groups including 17 muscles. The muscle groups are: the soleus, gastrocnemius, tibialis anterior, biceps femoris, vastus lateralis, rectus femoris, iliacus, gluteus medius, gluteus maximus, adductor magnus, vastus medialis and semitendinosus. The second model is actuated by 39 muscle groups consisting of the 12 muscle groups used in the first model with the addition of 27 muscle groups including 43 muscles used in the upper body model. The muscle groups in the upper body model are: the rectus abdominis, obliquus extremus abdom, erector spinae, scalenus anterior, scalenus medius, scalenus posterior, splenius cervicis, splenius capitis, sternocleidomastiodeus, pectoralis major, pectoralis minor, trapezius, latissimus dorsi, deltoideus, biceps brachii, brachioradialis, triceps brachii, pronator teres, flexor carpi ulnaris, flexor carpi radialis, flexor pollicis longus, psoas major, flexor digitorum profundus, extensor carpi rad longus, extensor digti minimi, abductor pollicis longus and subclavius. Figure 4.3 shows graphic representations of the first and second models used in this study.

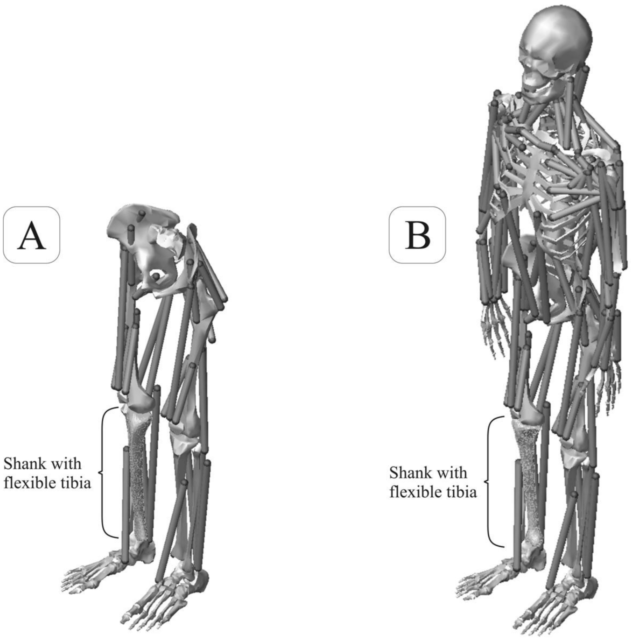

Figure 4.3 Graphic representations of the musculoskeletal first (A) and second as well as third (B) model used in this study.

Flexible Tibia

The geometrical configuration of the right flexible tibia of the first and second subjects is obtained from 3-dimensional reconstruction of MRI. In the introduced models, the tibial finite element model is described in **ANSYS** [63] using a 4-node tetrahedral solid element. Figure 4.4 shows the 4-node tetrahedral element used in discretizing the tibial finite element models.

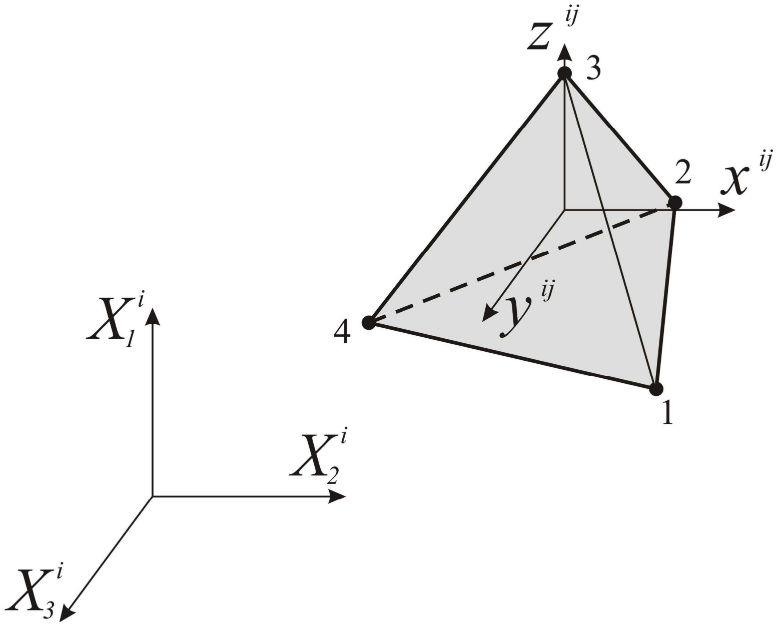

Figure 4.4 4-node tetrahedral solid element *j* used to describe the tibial finite element models.

The assumed nodal displacement field of element *j* shown in Figure 4.4 can be written as follows:

$$u^{ij}(x^{ij}, y^{ij}, z^{ij}) = N_1^{ij}u_1^{ij} + N_2^{ij}u_2^{ij} + N_3^{ij}u_3^{ij} + N_4^{ij}u_4^{ij}, \tag{4.1}$$

$$v^{ij}(x^{ij}, y^{ij}, z^{ij}) = N_1^{ij}v_1^{ij} + N_2^{ij}v_2^{ij} + N_3^{ij}v_3^{ij} + N_4^{ij}v_4^{ij}, \tag{4.2}$$

$$w^{ij}(x^{ij}, y^{ij}, z^{ij}) = N_1^{ij} w_1^{ij} + N_2^{ij} w_2^{ij} + N_3^{ij} w_3^{ij} + N_4^{ij} w_4^{ij}, \tag{4.3}$$

where $x^{ij} y^{ij} z^{ij}$ is the element coordinate system that is assumed to be parallel to the finite element tibial reference coordinate system $X_1^i X_2^i X_3^i$, u_k^{ij} is the translation of node *k*(*k* = 1,..,4) in x^{ij} direction, v_k^{ij} is the translation of node *k* in y^{ij} direction, w_k^{ij} is the translation of node *k* in z^{ij} direction and N_k^{ij} is the shape function of the degrees of freedom of node *k* in element *j*. The shape function N_k^{ij} can be described using the volume coordinates of element *j* as follows:

$$N_k^{ij} = L_k^{ij}, \tag{4.4}$$

where L_k^{ij} is a volume coordinate of element *j* which can be defined as follows [90]:

$$L_1^{ij} = \frac{1}{6V^{ij}}(a_1 + b_1 x^{ij} + c_1 y^{ij} + d_1 z^{ij}), \tag{4.5}$$

$$L_2^{ij} = \frac{1}{6V^{ij}}(a_2 + b_2 x^{ij} + c_2 y^{ij} + d_2 z^{ij}), \tag{4.6}$$

$$L_3^{ij} = \frac{1}{6V^{ij}}(a_3 + b_3 x^{ij} + c_3 y^{ij} + d_3 z^{ij}), \tag{4.7}$$

$$L_4^{ij} = \frac{1}{6V^{ij}}(a_4 + b_4 x^{ij} + c_4 y^{ij} + d_4 z^{ij}), \tag{4.8}$$

where V^{ij} is the volume of element *j* which can be defined as follows:

$$V^{ij} = \frac{1}{6}\begin{vmatrix} 1 & x_1^{ij} & y_1^{ij} & z_1^{ij} \\ 1 & x_2^{ij} & y_2^{ij} & z_2^{ij} \\ 1 & x_3^{ij} & y_3^{ij} & z_3^{ij} \\ 1 & x_4^{ij} & y_4^{ij} & z_4^{ij} \end{vmatrix}, \tag{4.9}$$

where $x_k^{ij}\,y_k^{ij}\,z_k^{ij}$ is the coordinates of node *k* in element *j* coordinate system. The constants a_1, b_1, c_1 and d_1 in Eq (4.5) can be defined as follows:

$$a_1 = \begin{vmatrix} x_2^{ij} & y_2^{ij} & z_2^{ij} \\ x_3^{ij} & y_3^{ij} & z_3^{ij} \\ x_4^{ij} & y_4^{ij} & z_4^{ij} \end{vmatrix}. \tag{4.10}$$

$$b_1 = -\begin{vmatrix} 1 & y_2^{ij} & z_2^{ij} \\ 1 & y_3^{ij} & z_3^{ij} \\ 1 & y_4^{ij} & z_4^{ij} \end{vmatrix}. \tag{4.11}$$

$$c_1 = -\begin{vmatrix} x_2^{ij} & 1 & z_2^{ij} \\ x_3^{ij} & 1 & z_3^{ij} \\ x_4^{ij} & 1 & z_4^{ij} \end{vmatrix}. \tag{4.12}$$

$$d_1 = -\begin{vmatrix} x_2^{ij} & y_2^{ij} & 1 \\ x_3^{ij} & y_3^{ij} & 1 \\ x_4^{ij} & y_4^{ij} & 1 \end{vmatrix}. \tag{4.13}$$

The other constants in Eq (4.6) to Eq (4.8) can be defined by cyclic permutation of subscripts 1, 2, 3 and 4 in the order $1 \to 2 \to 3 \to 4 \to 1$. Recalling back Eq (2.44), the kinematic matrix of element *j* in the flexible body *i* can be defined as follows:

$$\mathbf{D}^{ij} = \begin{bmatrix} \frac{\partial N_1^i}{\partial x^i} & 0 & 0 & \frac{\partial N_2^i}{\partial x^i} & 0 & 0 & \frac{\partial N_3^i}{\partial x^i} & 0 & 0 & \frac{\partial N_4^i}{\partial x^i} & 0 & 0 \\ 0 & \frac{\partial N_1^i}{\partial y^i} & 0 & 0 & \frac{\partial N_2^i}{\partial y^i} & 0 & 0 & \frac{\partial N_3^i}{\partial y^i} & 0 & 0 & \frac{\partial N_4^i}{\partial y^i} & 0 \\ 0 & 0 & \frac{\partial N_1^i}{\partial z^i} & 0 & 0 & \frac{\partial N_2^i}{\partial z^i} & 0 & 0 & \frac{\partial N_3^i}{\partial z^i} & 0 & 0 & \frac{\partial N_4^i}{\partial z^i} \\ \frac{\partial N_1^i}{\partial y^i} & \frac{\partial N_1^i}{\partial x^i} & 0 & \frac{\partial N_2^i}{\partial y^i} & \frac{\partial N_2^i}{\partial x^i} & 0 & \frac{\partial N_3^i}{\partial y^i} & \frac{\partial N_3^i}{\partial x^i} & 0 & \frac{\partial N_4^i}{\partial y^i} & \frac{\partial N_4^i}{\partial x^i} & 0 \\ 0 & \frac{\partial N_1^i}{\partial z^i} & \frac{\partial N_1^i}{\partial y^i} & 0 & \frac{\partial N_2^i}{\partial z^i} & \frac{\partial N_2^i}{\partial y^i} & 0 & \frac{\partial N_3^i}{\partial z^i} & \frac{\partial N_3^i}{\partial y^i} & 0 & \frac{\partial N_4^i}{\partial z^i} & \frac{\partial N_4^i}{\partial y^i} \\ \frac{\partial N_1^i}{\partial z^i} & 0 & \frac{\partial N_1^i}{\partial x^i} & \frac{\partial N_2^i}{\partial z^i} & 0 & \frac{\partial N_2^i}{\partial x^i} & \frac{\partial N_3^i}{\partial z^i} & 0 & \frac{\partial N_3^i}{\partial x^i} & \frac{\partial N_4^i}{\partial z^i} & 0 & \frac{\partial N_4^i}{\partial x^i} \end{bmatrix}^j . \quad (4.14)$$

The finite element model of the right tibia of the (1) first subject and (2) second subject, generated based on MRI is shown in Figure 4.5.

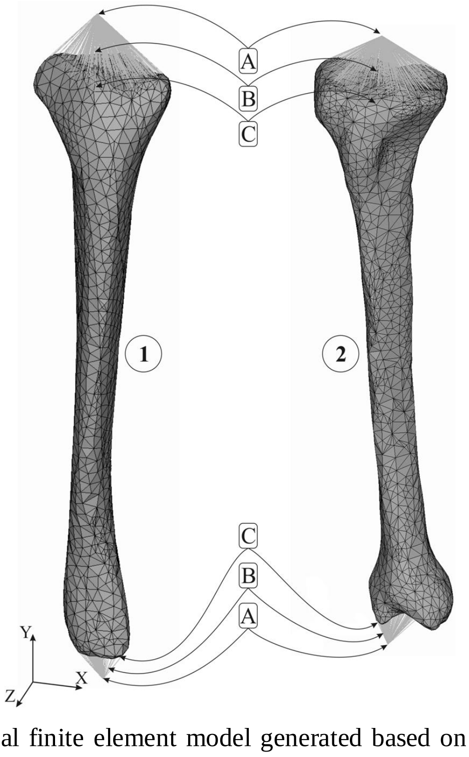

Figure 4.5 The tibial finite element model generated based on MRI and used in the forward dynamics simulation for strain analysis. (1) first subject and (2) second subject. A = two selected boundary nodes, B = massless rigid beams and C = surface nodes.

In order to couple the flexible tibia to the adjacent bodies, massless nodes are modeled at the location of the ankle and knee joints. These nodes are selected as boundary nodal coordinates, and connected to the nodes at the surface of the tibial metaphyses using a number of beam elements with unrealistic density and high stiffness as shown in Figure 4.5. This leads to a beam description to be practically rigid with no mass (i.e., massless rigid beams). These massless rigid beams transform constraint forces due to the joints to the flexible tibia. A large number of massless rigid beams are used in order to ensure that the constraint forces due to the joints do not cause unnatural local deformation in the flexible tibia. The flexible tibia is used in the forward dynamics analysis to calculate deformation due to dynamic loading using Eq (2.2). The material properties of the cortex bone are modeled to be linearly elastic and transversely isotropic. Young's modulus and the shear elastic modulus of the cortex bone are assumed to be 17 GPa and 10 GPa, respectively, in the longitudinal direction along the bone, while they are assumed to be transversely isotropic with the values of 5 and 3.5 GPa, respectively [91]. The total number of nodal degrees of freedom of the tibial finite element models of the first and second subjects are 16719 (i.e., $n = 16719$) and 18384, respectively.

Foot-Ground Contact Model

An increasing number of applications of the biomechanical models in sports, gait analysis, health and product development requires comprehensive modeling of the contact with the surrounding environment. The interaction between the biomechanical model and the environment, such as the gravity, contact and collision forces has to be taken into account during the simulation. In the introduced models, the contact between the foot and the ground has to be taken into account. The foot-ground contact model should prevent the foot from falling down through the ground and release it from the ground at the toe-off as well. Generally, in the biomechanical models, the description of the contact, such as the foot-ground contact, consists of two models. The first model is the contact force model which represents the interaction between the matting surfaces. The second model is the contact detection model based on the geometric description of the contacting surfaces. In this study, the foot-ground contact force is modeled using five

spring-damper systems located under each metatarsal head, in addition to one spring-damper system located under the calcaneous. Each spring applies force in all three directions; vertical, fore-aft and transverse. The vertical force varies exponentially with the height of the foot above the ground in order to diminish quickly as the foot rises above the ground [16]. The forces in the fore-aft and transverse directions are linear functions of the foot position in the transverse plane and represent the friction forces preventing the foot from slipping during contact. The magnitude of the ground reaction force is typically the resultant of the vertical and friction forces. The foot-ground contact force model properties consists of stiffness of the contact, damping of the contact, vertical force exponent coefficient, full damping depth, static friction coefficient, dynamic friction coefficient, friction transition velocity and stiction transition velocity.
Table 4.3 shows the values used to define the foot-ground contact force model properties in the introduced models.

Table 4.3 Foot-ground contact force model parameters in the first and second models. The stiffness, damping and full damping depth values are defined based on the study of Gilchrist and Winter [92].

Contact parameters	**First Model**	**Second and Third Models**
Stiffness	200 N/mm	150 N/mm
Damping	2 Ns/mm	20 Ns/mm
Exponent coefficient	1	1
Full damping depth	1 mm	1 mm
Static friction coefficient	1	1
Dynamic friction coefficient	0.8	0.8
Friction transition velocity	1 mm/s	1 mm/s
Stiction transition velocity	1 mm/s	1 mm/s

The geometrical contact detection model, in this study, is represented by a 3-dimensional ellipsoid contact surface located under each metatarsal head, in addition to one ellipsoid contact surface located under the calcaneous, while the ground is represented by a flat surface. The use of the ellipsoid surface provides easiness in detecting the contact points between the foot and the ground plane, calculating the ground reaction force with higher fidelity, and increasing the compliance between the foot and the ground. The values of the stiffness and damping of the foot-ground contact models can be tuned so that the simulated ground reaction force for each model would be in a good agreement with the experimental measured one. Generally, it can be noticed that increasing the stiffness value will increase the ground reaction force and decrease the contact time between the foot and the ground. Increasing the damping value will decrease the oscillations in the ground reaction force curve and increase the contact time between the foot and the ground. Figure 4.6 shows a graphic representation of the ellipsoid contact surfaces used in calculating the ground reaction force.

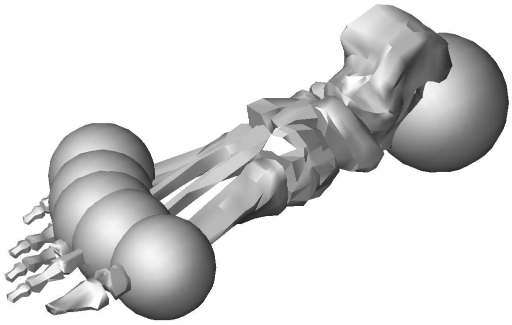

Figure 4.6 Graphic representation of the 3-dimensional contact ellipsoid surfaces.

4.4. Human Experiments

Gait analysis laboratories equipped with motion capture systems, force plates and EMG electrodes recorders are increasingly being used to measure body motion, ground forces and muscular activation patterns, respectively, in a non-invasive manner. The human experiments were conducted in the Neuromuscular Research Center in the department of Biology of Physical Activity at University of Jyväskylä. The subjects are asked to walk barefoot at a constant velocity (1.47 m/s for the first subject and 1.5 m/s for the second subject) on top of a 10 m long force platform (Raute Inc, Finland) on a level ground.

Vertical and horizontal ground reaction forces are collected separately for the right leg from both subjects. The resultant ground reaction force is calculated from the right leg of each subject. EMG activity of the right tibialis anterior, soleus, rectus femoris, vastus lateralis, biceps femoris and gluteus medius muscles are recorded simultaneously from the walking test conducted for the first subject. EMG activity from the right tibialis anterior, soleus, rectus femoris, vastus lateralis, biceps femoris, gluteus medius, vastus medialis, gastrocnemius medialis, gastrocnemius lateralis, and gluteus maximus muscles are recorded simultaneously from the walking test conducted for the second subject. Bipolar EMG Ag/AgCl electrodes with inter-electrode distance of 20 mm are used. The EMG electrodes are prepared and positioned according to SENIAM [93] recommendations. In case of tibialis anterior, biceps femoris and vastus lateralis the positioning is made in accordance with the study of Rainoldi et al. [94]. The ground reaction force and EMG are sampled at 2000 Hz (CED limited analog to digital board, Cambridge, England). The video, ground reaction force and EMG collection are synchronized and the data collection is started with a pair of photocells. The photocells are also used to determine the walking velocity. The walking exercise conducted for the first subject is recorded with four digital video cameras (COHU High Performance CCD Camera, San Diego CA, USA) at 50 Hz sampling frequency. The walking exercise conducted for the second subject is recorded with four video cameras (two analogic: HSC-200 PM, Peak Performance Technologies Inc., CO, USA and two digital: HDR-HC3E, Sony Corporation, Japan) at a 50 Hz sampling frequency. Schematic illustrations of the measurement set up of the first and second subjects are provided in Figure 4.7.

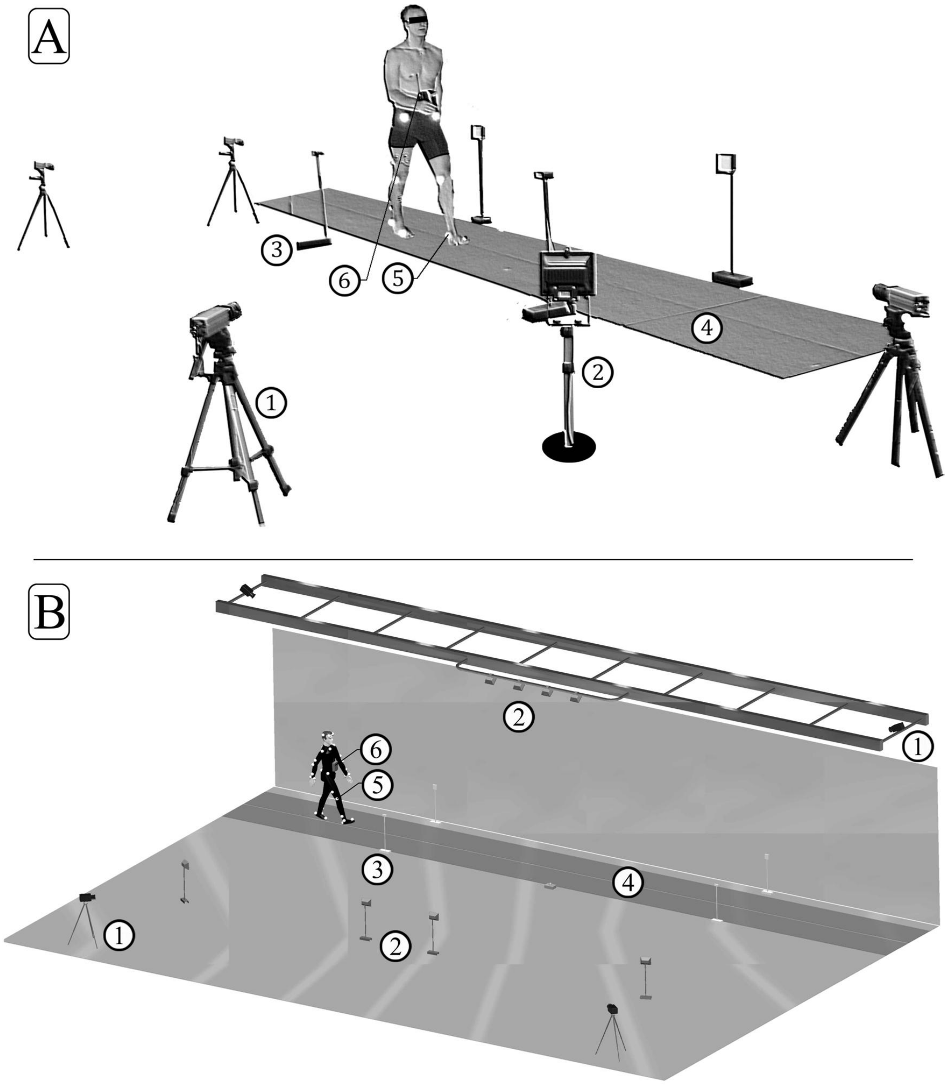

Figure 4.7 Schematic illustration of the experimental set up of the first subject (A) and the second as well as third subjects (B). 1. Cameras. 2. Light source. 3. Photocells. 4. Force platform. 5. Visual markers. 6. Telemetric EMG transmitter.

The camera pick-up area is adjusted in such a way that approximately a 1.5 walking cycle could be recorded from each camera. Visual markers are placed on the first and second subjects before the beginning of the experiments in predefined anatomical and technical landmarks, following guidelines given in Reference [14] as shown in Figure 4.8.

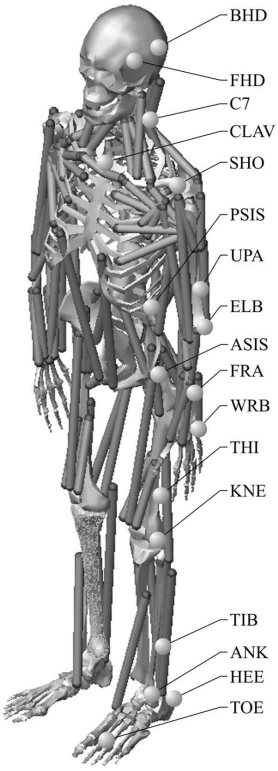

Figure 4.8 Schematic illustration of the motion capture marker placement. The markers on the lower body are applied on the first subject while the markers on the full body are applied on the second and third subjects. BHD = back head, FHD = front head, C7 = 7th cervical vertebrae, Clav = clavicle, SHO = acromio-clavicular joint, UPA = upper arm between ELB and SHO markers, PSIS = posterior superior iliac spine, ELB = humeral lateral epicondyle, ASIS = anterior superior iliac spine, FRA = forearm between ELB and WRB markers, WRB = ulnar epicondyle THI = lower lateral 1/3 surface of the thigh, KNE = femoral lateral epicondyle, ANK = lateral malleolus, TIB = lower 1/3 of the shank, TOE = second metatarsal head, HEE = calcaneous at the same height as the toe marker.

One walking cycle, from heel strike of the right leg to the next heel strike, is selected for the analysis. The video clips from all four cameras are digitized using **Peak Motus 8.1.0** (Peak Performance Technologies Inc, USA), and the software is used to calculate the 3-dimensional coordinates for each marker. The coordinate system is arranged so that the *X*-axis is in the direction of the walking movement, the *Y*-axis is from right to leg compared to the direction of the movement, and the Z-axis is directed up. The 3-dimensional coordinates are exported to **MATLAB®** [95]. In order to minimize the digitization error, each of the coordinates is filtered with a 2nd order 5 Hz low-pass Butterworth filter [2]. The direction of the movement is transferred linearly, so that all of the digitized markers move an equal amount in X-direction, while each of the markers has the same Z and Y coordinate values at the beginning and end of the walking cycle. Successive walking cycles of one person can be assumed to have a similar pattern [78]. Therefore, the coordinates are interpolated so that coordinate data for a total of four identical walking cycles are produced. A total number of 250 sagittal MRI from the right tibia of the first subject with slice thickness of 1.2 mm are taken (Signa 1.5T Excite, GE Medical Systems, France) with intervals of 0.6 mm in the neutral unloaded position. As regards the second subject, a total number of 130 coronal MRI from the right tibia with slice thickness of 1.2 mm are taken (Philips Intera 1.5T, Netherlands) with intervals of 0.6 mm in the neutral unloaded position.

4.5. Numerical Analysis

The significant deformation modes in the forward dynamics simulation of the walking exercise are selected based on the strain energy method. A total number of 10 deformation modes (i.e., $m = 10$) are used in the numerical analysis of the first model, and a total number of 11 deformation modes are used in the numerical analysis of the second model. A critical damping ratio of 1 is applied to the selected modes based on the study of Dias Rodrigues et al. [96]. Figure 4.9 and Figure 4.10 show the selected tibial deformation modes for the first and second models, respectively, with their natural frequencies used in the forward dynamics analysis to obtain the tibial strains.

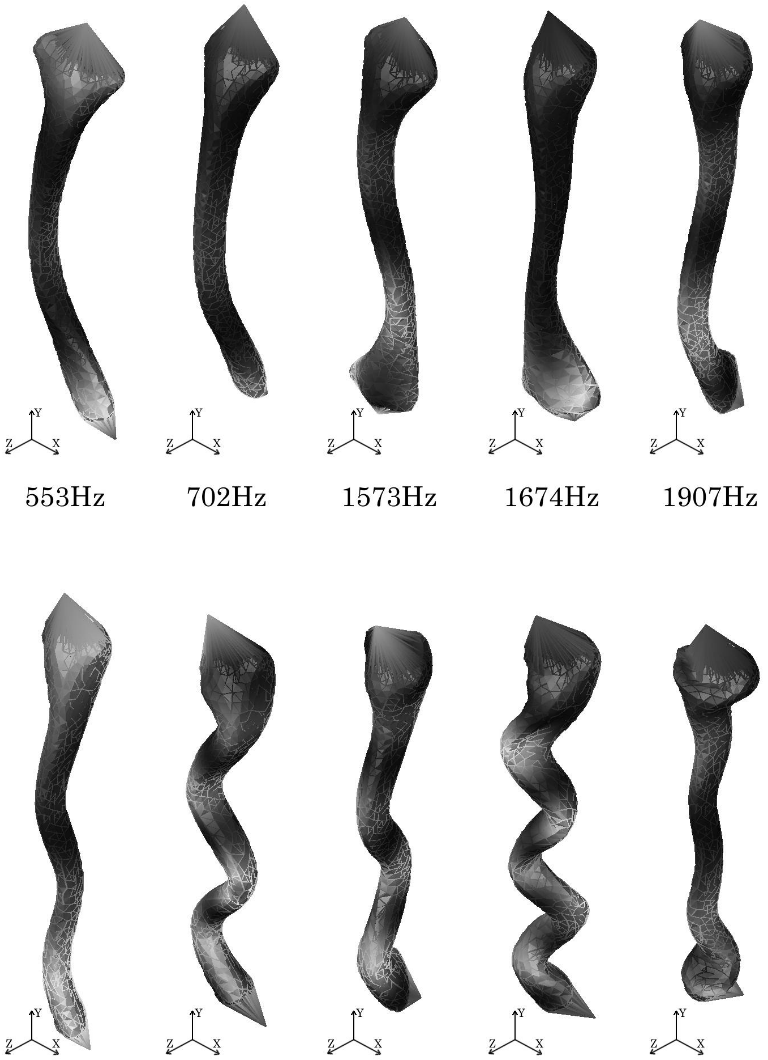

553Hz 702Hz 1573Hz 1674Hz 1907Hz

4799Hz 4999Hz 5561Hz 9244Hz 13966Hz

Figure 4.9 The selected tibial deformation modes with their natural frequencies of the flexible tibia used in the first model.

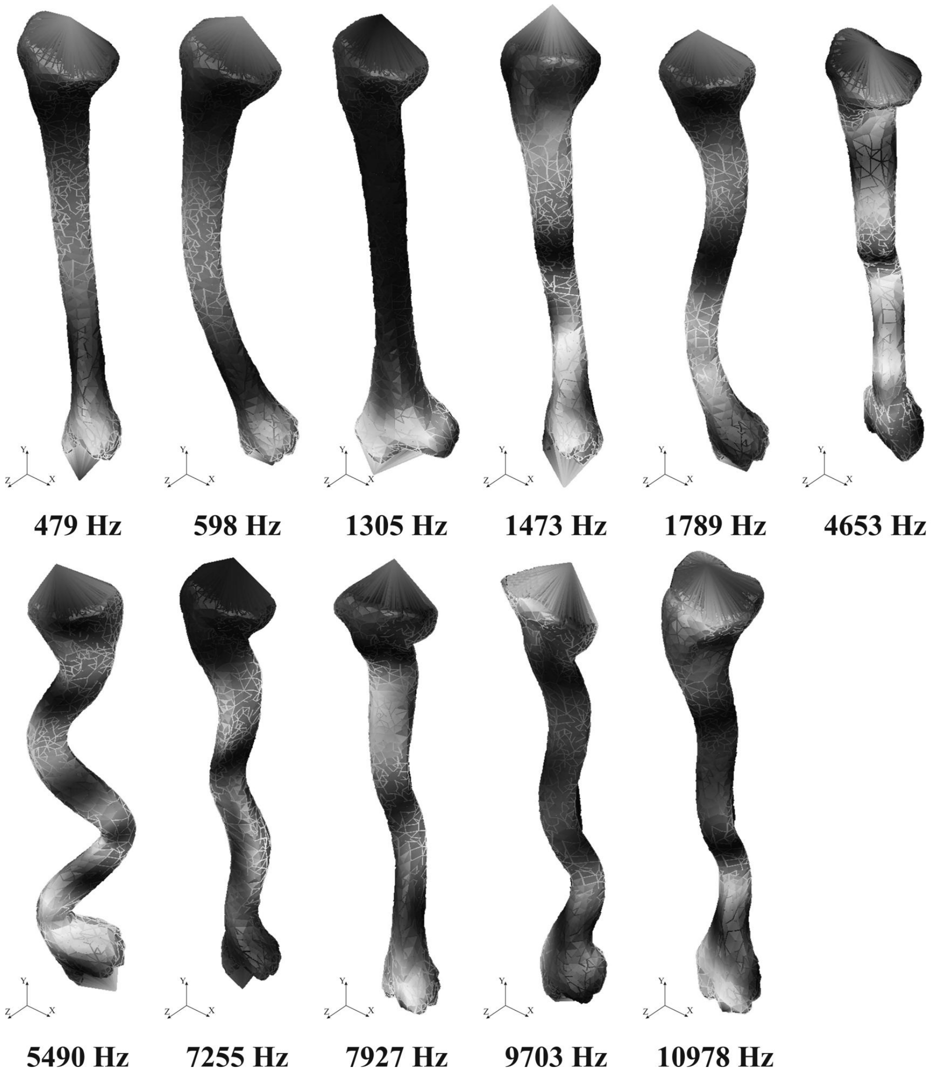
479 Hz
598 Hz
1305 Hz
1473 Hz
1789 Hz
4653 Hz
5490 Hz
7255 Hz
7927 Hz
9703 Hz
10978 Hz

Figure 4.10 Same as Figure 4.9 for the second model.

The principal strains and maximum shear strain are obtained from the introduced models at a location corresponding to the location defined by Lanyon et al. [79], Burr et al. [46], Milgrom et al. [80, 81] at the anteromedial aspect of the right tibial midshaft. The principal strains and maximum shear strain obtained from the previous *in vivo* strain measurements studies are calculated from the measured in plane strains using rosette strain gauge bonded to the anteromedial aspect of the right tibial midshaft. Therefore, for the sake of comparison with the previous *in vivo* strain measurements, the principal and maximum shear strains can be calculated based on the in plane strains obtained from the models using the following standard formulas [97]:

$$\varepsilon_{1,2} = \frac{\varepsilon_y + \varepsilon_z}{2} \pm \sqrt{\left(\frac{\varepsilon_y - \varepsilon_z}{2}\right)^2 + \left(\frac{\gamma_{yz}}{2}\right)^2}\,, \tag{4.15}$$

$$\gamma_{\max} = 2\sqrt{\left(\frac{\varepsilon_y - \varepsilon_z}{2}\right)^2 + \left(\frac{\gamma_{yz}}{2}\right)^2} = (\varepsilon_1 - \varepsilon_2)\,, \tag{4.16}$$

where $\varepsilon_{1,2}$ and $\gamma_{\max}$ are the maximum, minimum principal and maximum shear strains, respectively and $\varepsilon_y, \varepsilon_z$ and γ_{yz} are the in plane normal strains in *Y* and *Z* directions and the shear strain in the *YZ* plane, respectively, which can be obtained from the introduced models.

To demonstrate the strain distributions around the cross section at the middle of the tibial shaft during the stance phase, the axial strain defined in the direction of the long axis of the tibia is simulated in four locations corresponding to the locations defined by Peterman et al. [82]. The muscular forces and the ground reaction force dominate the loading on the bone [98], which in turn determines the strain behavior. Therefore, in order to verify the accuracy of the introduced models, the ground reaction force and EMG activation patterns obtained from experiments are compared with their correspondences obtained from the models in terms of the cross-correlation coefficient (γ). It is essential to point out that due to the ethical and legal restrictions in measuring the muscle force in humans invasively, muscular forces obtained from the simulation models are usually evaluated based on a qualitative comparison with the corresponding EMG patterns obtained from experimental measurements [66, 99]. There is an agreement in the scientific community about the relation between the EMG signal and the corresponding muscle force, in a sense that, increasing the firing rate of an individual motor unit and/or increasing the number of motor units leads to an increment in the generated muscle force and the corresponding EMG signal [25, 66]. However, the nature of this relation is still under research and investigation due to many reasons which are explained later on in this chapter. The kinematics of the models obtained from the inverse and forward dynamics simulations are compared in order to verify the capability of the models of replicating the motion in the forward dynamics simulation. This is accomplished by comparing the position of the mass center of each segment in the models in the X, Y and Z directions, resulting from inverse dynamics simulation to their correspondences resulting from forward dynamics simulation in terms of γ.

4.6. Results

Four walking cycles are simulated using a simulation time step of 0.02 seconds. Screen shots of the walking performance during the forward dynamics simulation for one walking cycle of the right leg from the (1) first model (2) second model are provided in Figure 4.11.

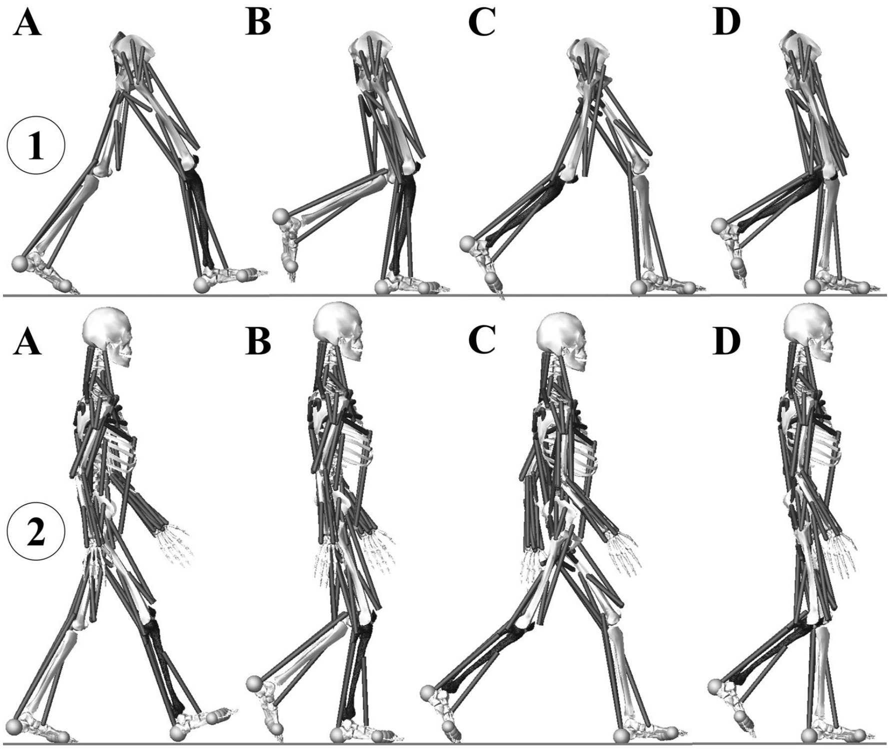

Figure 4.11 Screen shots of the walking performance during the forward dynamics simulation for one walking cycle of the right leg in the (1) first model and (2) second model. A) Heel strike, B) Full foot-heel off, C) heel off-toe off and D) forward swing.

The values for the maximum and minimum principal strain, maximum shear strain and axial strain are obtained from the models. The numerical strain results obtained from the models and their correspondences reported from the previous *in vivo* strain measurements are given in Table 4.4. Figure 4.12 and Figure 4.13 show the simulated maximum and minimum principal strains and maximum shear strains for four walking cycles.

Table 4.4 The principal and maximum shear strain magnitudes with their rates. Literature values from *in vivo* measurements and the values estimated by the models. The principal and maximum shear strains are obtained from the anteromedial aspect of the tibial midshaft, which is the same location in all of the studies mentioned in the table.

	Strain magnitude [microstrain]			**Strain rate [microstrain/s]**		
	Max principal	Min principal	Max Shear	Max	Min	Max shear
Lanyon et al. [79]	395	-434	829	Not reported	-4000	Not reported
Burr et al. [46]	437	-544	871	11006	-7183	16162
Milgrom et al. [80]	840	-454	1183	3955	-3306	10303
Milgrom et al. [81]	394	-672	Not reported	4683	-3820	Not reported
First model	305	-645	948	4000	-7000	10000
Second model	335	-453	785	6000	-6300	10230

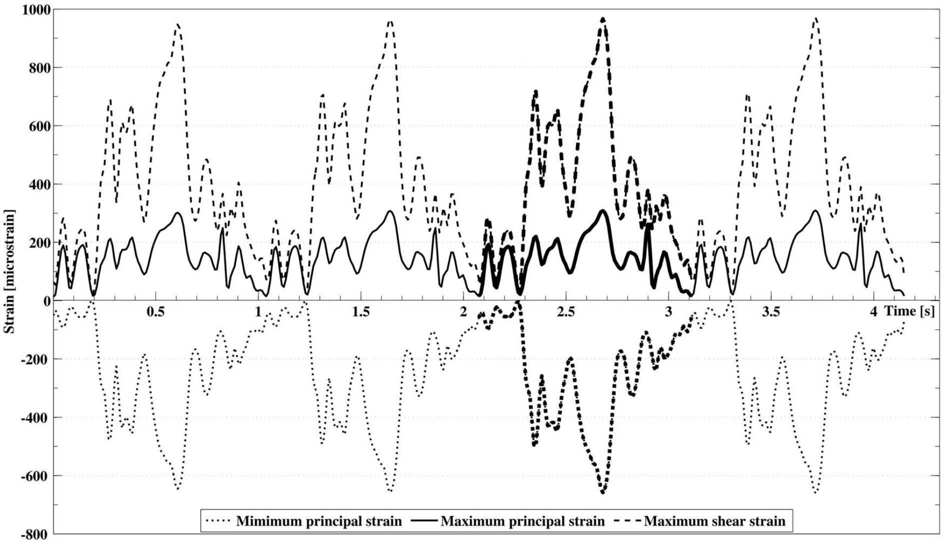

Figure 4.12 Simulated maximum and minimum principal strains and maximum shear strain curves at the anteromedial aspect of the right tibial shaft of the first model for four walking cycles. The bolded line corresponds to one walking cycle.

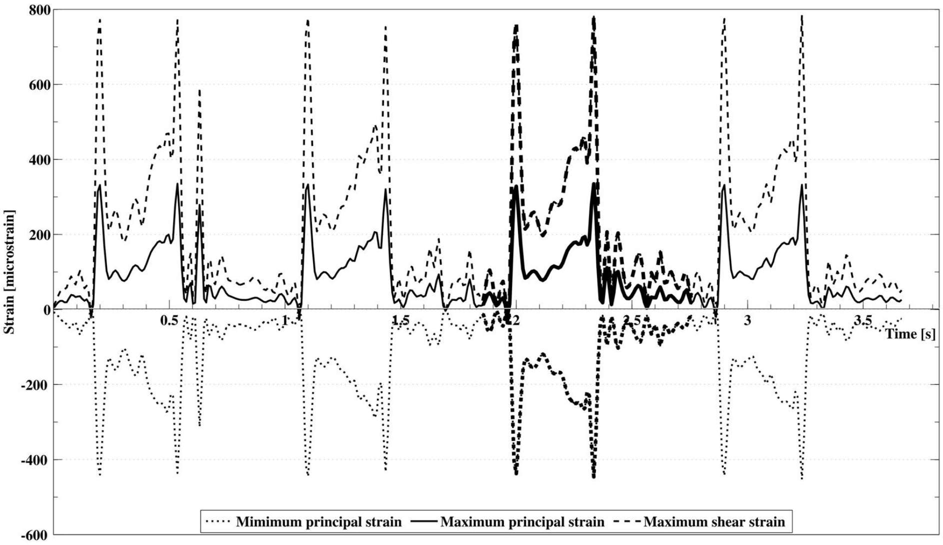

Figure 4.13 Same as Figure 4.12 for the second model.

As regards the ground reaction force and muscular forces, Table 4.5 shows the cross-correlation coefficient (γ) between measured and simulated values.

Table 4.5 Cross-correlation coefficient (γ) between measured and simulated values of the ground reaction and muscular forces of the first and second models.

Compared Items	**First model** (γ)	**Second model** (γ)
Ground reaction force	0.97	0.95
Soleus	0.94	0.64
Gluteus medius	0.75	0.84
Vastus lateralis	0.65	0.47
Tibialis anterior	0.39	0.80
Biceps femoris	0.33	0.55
Rectus femoris	0.22	0.29
Gastrocnemius Lateralis	-	0.82
Gastrocnemius Medialis	-	0.86
Gluteus maximus	-	0.72
Vastus medialis	-	0.50

Simulated and measured muscular forces of the first and second models are plotted in Figure 4.14 and Figure 4.15. Simulated and measured ground reaction forces of the first and second models are plotted in Figure 4.16. In the comparison of the kinematics of the models between inverse and forward dynamics simulations, γ is higher than 0.99 for the position of the mass center of each segment in the models in the X, Y and Z directions.

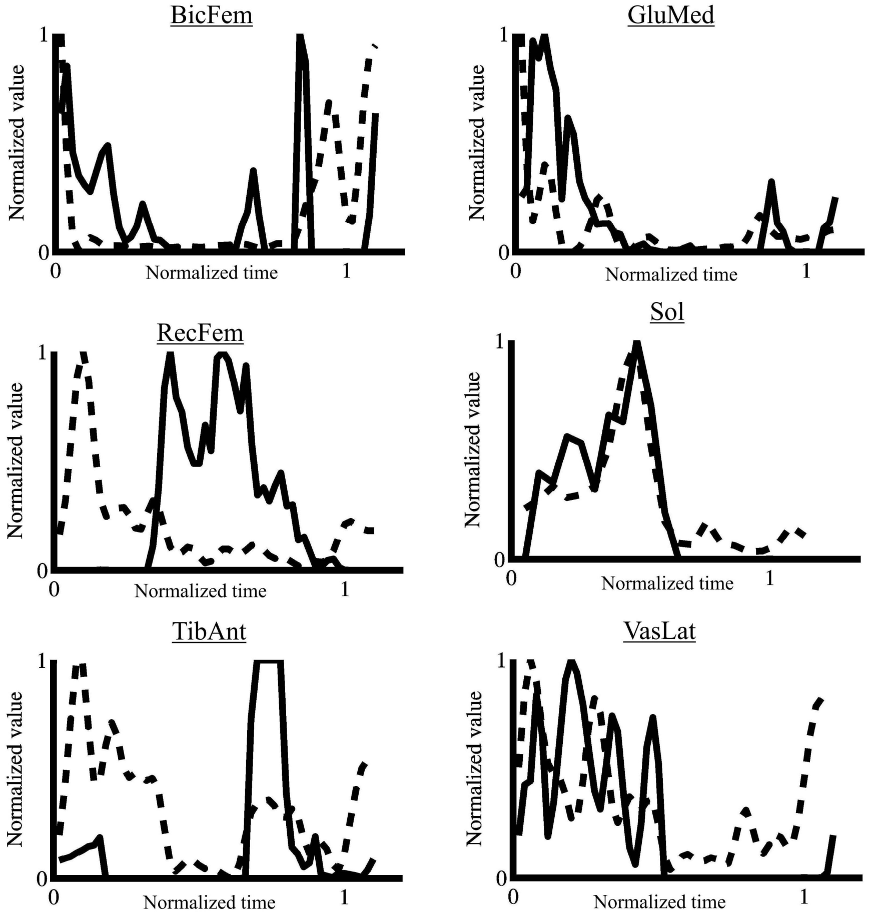

Figure 4.14 Measured electromyographical (EMG) muscle activity (dashed line ---) and simulated muscular force production (solid line ——) obtained from the first model plotted against normalized time for one walking cycle. EMG and force values are normalized to the maximum values for each plot. EMG is rectified and low pass filtered at 10 Hz. BicFem = biceps femoris, GluMed = gluteus medius, RecFem = rectus femoris, Sol = soleus, TibAnt = tibialis anterior and VasLat = vastus lateralis.

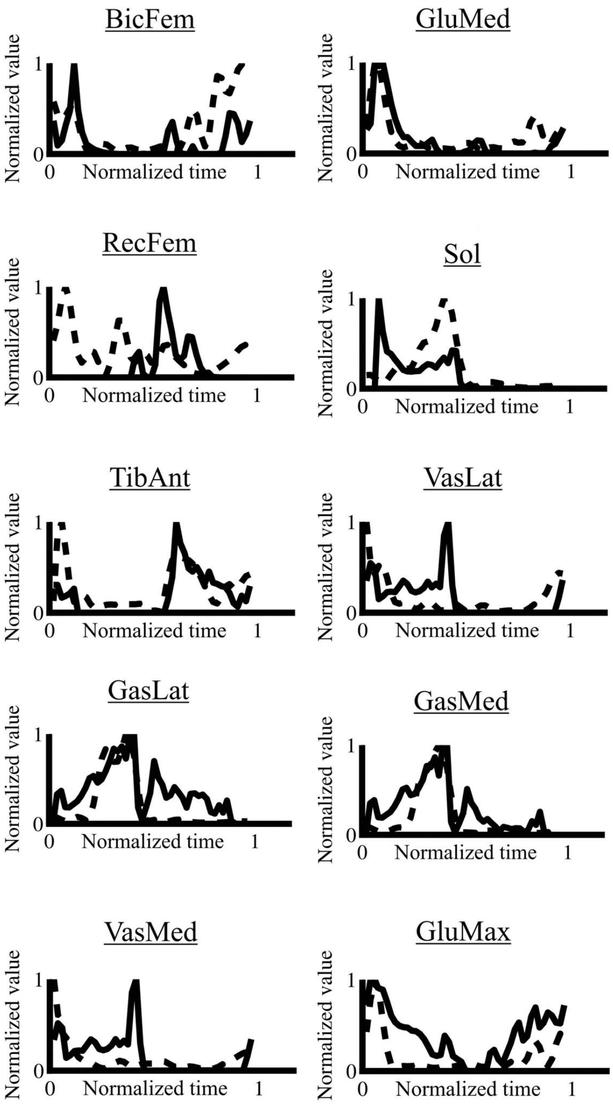

Figure 4.15 Measured electromyographical (EMG) muscle activity (dashed line ---) and simulated muscular force production (solid line ––) obtained from the second model plotted against normalized time for one walking cycle. EMG and force values are normalized to the maximum values for each plot. EMG is rectified and low pass filtered at 10 Hz. BicFem = biceps femoris, GluMed = gluteus medius, RecFem = rectus femoris, Sol = soleus, TibAnt = tibialis anterior, VasLat = vastus lateralis, GasLat = gastrocnemius lateralis, GasMed = gastrocnemius medialis, VasMed = Vastus medialis, GluMax = Gluteus maximus.

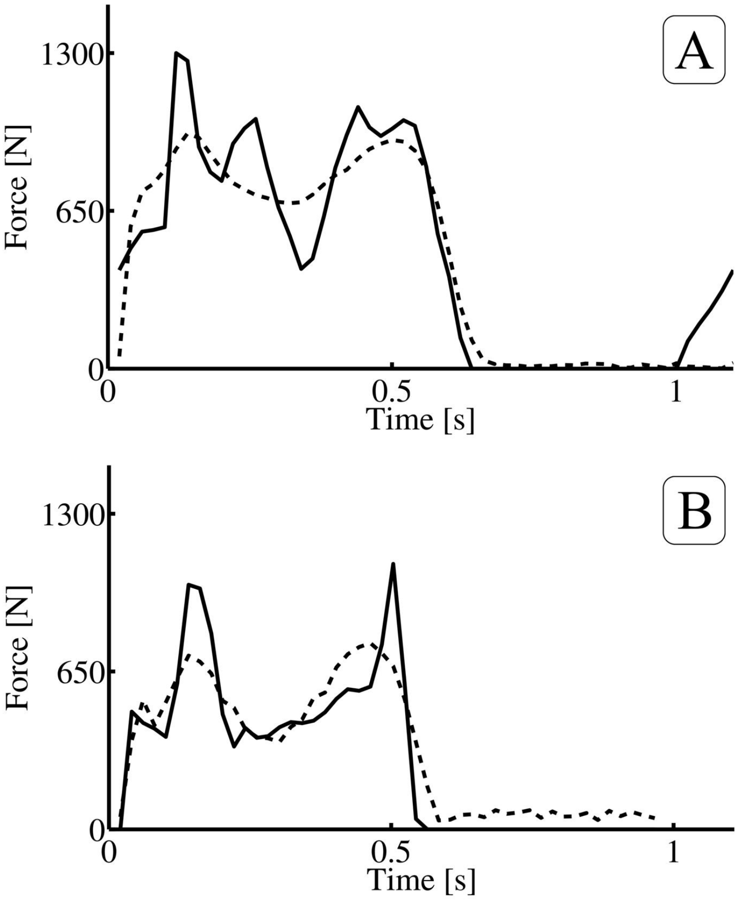

Figure 4.16 Measured ground reaction force (dashed line ---) and simulated ground reaction force (solid line —–) obtained from the first model (A) and second model (B) plotted against time for one walking cycle.

4.7. Discussion

No significant difference is found between the strain results obtained from the present models and the previous *in vivo* strain measurements [46, 79, 80, 81]. The accuracy of the strain results predicted by the introduced models is investigated. Based on this investigation, the strain magnitudes obtained from the models are strongly dependent on the ground reaction force estimation and the significant deformation modes used in the numerical analysis. This implies that if the models are capable of predicting reasonable ground reaction force comparable to the values and patterns measured from the experiment, the strain magnitude estimation can stay within the normal and acceptable ranges. In order to investigate the effect of the deformation modes used to describe the flexibility of the tibial model on the strain results, a total number of 25 deformation modes is calculated for each model. Based on the strain energy method, the significant deformation modes used in the numerical analysis for every model, represent the modes at which the convergence of the strain results occurs. Therefore, including the other deformation modes of each model has insignificant effect on the strain results. The deformation modes calculated for each model are shown in Appendix A(II). Moreover, the significant deformation modes of the flexible tibia rely on the geometrical configuration of the individual flexible tibial model and the performance of the walking exercise in the forward dynamics simulation. It is essential to point out that the local strains developed at the nodes near the muscle insertion points on the bone, require local deformation modes that can accurately capture the deformation at these locations. In addition, the muscle insertion should be modeled with more complexity, taking into account the insertion as an area rather than a point and giving an insight into the distribution of the muscle force in the region where the muscle is inserted. Further, a highly dense bone mesh at the muscle insertion region is required for this kind of complex muscle attachment model, and to capture the local strains with an adequate accuracy.

It can be depicted from Figure 4.16, that the ground reaction force corresponds to the phases of the walking cycle explained previously in this chapter. It can be noticed that there are two peaks representing the heel strike and the toe-off, respectively, and the sway curve in between represents the stance phase occurring between the heel strike until the toe- off and finally the curve starts to decay until it reaches zero during the forward swing phase. The simulated ground reaction force and muscular forces are used to verify the introduced models. Due to the fact that the musculoskeletal loading conditions are widely unknown and may vary considerably [100], the strain magnitudes obtained from the present models may be considered as an acceptable approximation of the previous *in vivo* strain measurements.

Strain Results

The study of Lanyon et al. [79] is considered as the first *in vivo* strain measurement on a tibia for a normal subject during physical activities. In that study, walking on a belt without shoes at 1.4 m/s is one of these physical activities where tibial strains are assessed. The maximum principal and maximum shear strains obtained from the first model are different by 23% and 14%, respectively, with respect to their correspondences reported by Lanyon et al. [79]. The maximum and minimum principal strains and maximum shear strain obtained from the second model differ by 15%, 4% and 5%, respectively, with respect to values reported by Lanyon et al. [79]. The profiles of the maximum and minimum principal strains shown in Figure 4.12 and Figure 4.13 seem to be comparable to their correspondences obtained from the study of Lanyon et al. [79] (see Appendix A(III)). The oscillations in the strains are apparently due to the fluctuations of the muscular forces. The high peaks observed at the strain profiles shown in Figure 4.13 at the heel strike and push off phases can be explained because of the over estimated ground reaction force obtained from the second model at those phases, which can be noticed in Figure 4.16. The study of Burr et al. [46] shows *in vivo* strain measurements in two subjects during walking at 1.39 m/s and wearing heavy infantry boots weighing 1.2 kg. The differences between the values of the minimum principal strain and maximum shear strain obtained from the first model are 18% and 9%, respectively, with respect to their correspondences obtained in Burr et al. [46]. The maximum and minimum principal strains and maximum shear strain obtained from the second model differ by 23%, 17% and 10%, respectively, with respect to the values obtained in Burr et al. [46]. Yet, the maximum shear strain curve obtained from the models appears to be comparable to the one obtained in Burr et al. [46] (see Appendix A(III)). It can be noticed that the strain rate magnitudes obtained in Burr et al. [46] are higher than their correspondences obtained from the models and the other *in vivo* strain measurement studies. However, the minimum strain rates obtained by the first and second models are different by 3% and 12%, respectively, with respect to the value reported by Burr et al. [46]. Milgrom et al. [80] present tibial principal strains measured *in vivo* in six subjects during walking with running shoes on a treadmill at 1.39 m/s. While the value of the maximum shear strain obtained from the first model is different by 20% of the corresponding strain observed by Milgrom et al. [80], the maximum strain and maximum shear strain rates obtained from the first model are within the range of ±2% of their correspondences reported in the same study. In the second model, the predicted minimum principal strain and maximum shear strain rate are almost identical compared to the values reported in the study of Milgrom et al. [80], with an insignificant difference which can be considered negligible. Furthermore, in a recent study by Milgrom et al. [81], the tibial principal strains and strain rates are measured *in vivo* during walking with running shoes for four male subjects. The values of the maximum and minimum principal strains obtained from the first model are different by 22% and 4% with respect to the corresponding ones obtained by Milgrom et al. [81], while the value of the maximum strain rate is 14% lower than its correspondence reported in the same study. The maximum and minimum principal strains predicted by the second model differ by 15% and 32%, respectively, with respect to the values observed in the study of Milgrom et al. [81]. Comparing the previous *in vivo* strain measurements during walking to the numerical results obtained from the present models, it can be concluded that the results obtained from the models are reasonable and consistent with the *in vivo* strain data. The differences between the strain results may be explained on the basis of many aspects such as the subject’s age, gender, height and weight, in addition to the experimental techniques used to measure the strains.

Strain Distributions

In the study of Peterman et al. [82], the dynamic gait simulator described by Sharkey and Hamel [101] is used to measure the strain *in vitro* during the stance phase of walking from heel strike to toe off. In that study, five cadaver feet from different donors are harvested approximately 180 mm above the ankle, and seven gage strain rosettes are bonded at the middle of each harvested tibial shaft (approximately 90 mm above the ankle) in seven locations around the cortex of the tibia. Axial strain profiles measured in the direction of the long axis of the tibia from four gages are reported in that study. Figure 4.17 and Figure 4.18 show the simulated axial strain profiles at the middle of the tibia of the first and second models, respectively, in four locations which correspond most closely to the locations defined by Peterman et al. [82].

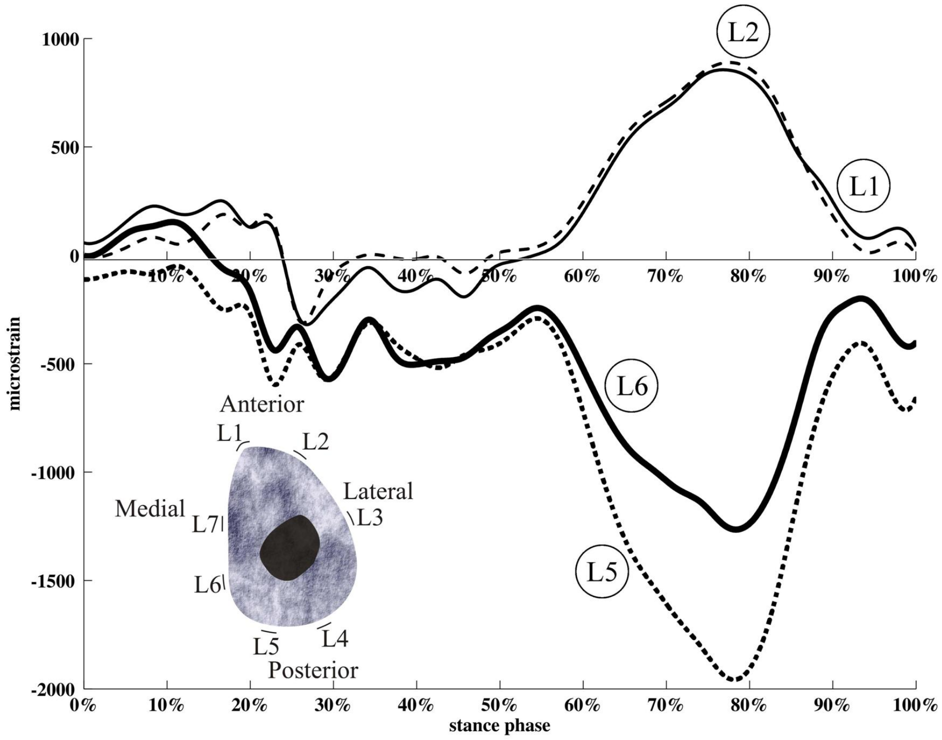

Figure 4.17 Simulated axial strain curves at two anterior and two posterior sites around the cortical tibia at the middle shaft during the stance phase. The shape represents the cortical cross sectional geometry at the middle of the first subject’s tibia with marked locations that correspond most closely to the locations defined in the study of Peterman et al. [82].

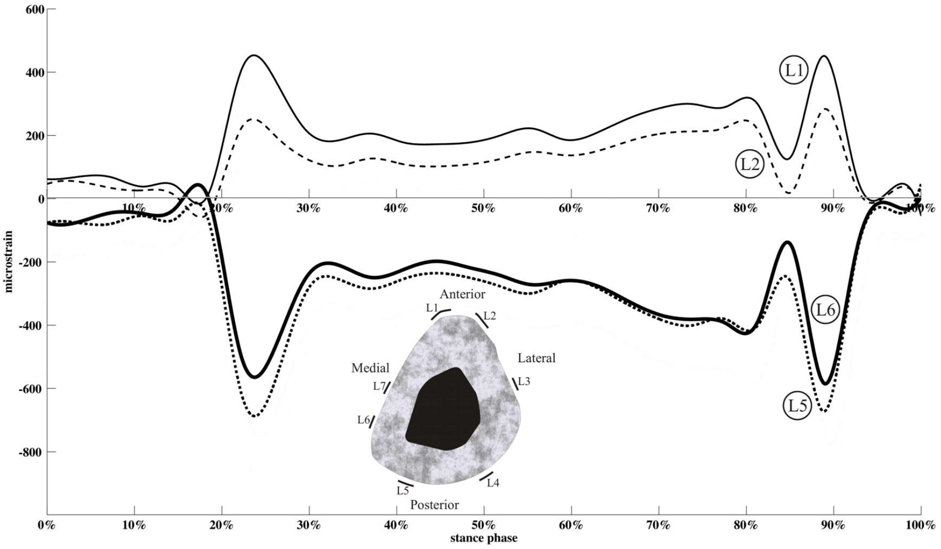

Figure 4.18 Same as Figure 4.17 for the second model.

The simulated strain profiles shown in Figure 4.17 and Figure 4.18 are similar to their correspondences recorded in the study of Peterman et al. [82] (see Appendix A(III)). It is worth mentioning that strains at different distances between the ankle and the middle of the tibia are simulated using the presented models in the same locations around the cortical tibia as defined by Peterman et al. [82], and their profiles were similar across all simulations and distance levels. Peterman et al. [82] state that they measured the strains around the cortical tibia at different distances 90, 120 and 150 mm above the ankle, and their profiles were also similar across all measurements and mounting levels. Another concluding remark obtained from the models agreeing with what is stated in the study of Peterman et al. [82] is that the axial strains at the anterior location L1 has a similar profile to the maximum principal strain while axial strain at the posterior location L5 reflects the minimum principal strain. The strain measurements reported in the study of Peterman et al. [82] from the seven gage strain rosettes about the cortical tibia and their correspondences obtained from the models are shown in Table 4.6.

Table 4.6 Strain distribution magnitudes about the cortical tibia obtained from the introduced models and their correspondences reported in the study of Peterman et al. [82].

Locations & Type of strains	**Peterman et al. [82] (mean*, peak) [microstrain]**	**First model [microstrain]**	**Second model [microstrain]**
L1			
Axial strain	505*, 989	855	451
Maximum principal strain	603*, 1088	855	452
Minimum principal strain	-155*, -240	-624	-368
Maximum shear	670*, 1185	1480	820
L2			
Axial strain	600*	888	283
L3			
Axial strain	-500*	-623	-257
L4			
Axial strain	-1400*	-1800	-675
L5			
Axial strain	-1020*, -1864	-1900	-673
Maximum principal strain	369*, 674	1499	471
Minimum principal strain	-1055*, -1926	-1907	-677
Maximum shear	1293*, 2317	3406	1148
L6			
Axial strain	-1200*	-1300	-584
L7			
Axial strain	0*	-635	-273

The strain distributions obtained from the introduced models indicate that bending is the primary mode of tibial loading, as it has been shown in other mammalian long bones according to the studies of Biewener [102] and Garcia and da Silva [103]. It can be noticed from Table 4.6 that in general the strain values obtained from the models have acceptable agreement with their correspondences reported in the study of Peterman et al. [82], except for the axial strain obtained at location L7. The discrepancy between the simulated axial strain at location L7 and its corresponding measured strain reported in the study of Peterman et al. [82] may be explained based on the location of the neutral axis of bending during the stance phase. In the introduced models, the strain distributions represent simulated strains around the cortical tibia at the middle of the tibial shaft, where the whole tibia is taken into consideration. On the other hand, in the study of Peterman et al. [82], the strain distributions represent measured strains around the cortical tibia at the middle of the tibial shaft, where the tibia is harvested 180 mm above the ankle. Therefore, the location of the neutral axis of bending in the tibia of the introduced models might differ from the one reported in the study of Peterman et al [82]. In the study of Peterman et al. [82], the axial strains measured at location L7 nearly averaged to zero due to the close proximity of this location to the neutral axis of bending during the stance phase, as stated in that study. On the other hand, in the introduced models it seems that location L7 experiences compressive stress during the stance phase. However, an agreement can be found between the axial strain obtained from the introduced models at location L7 and its correspondence measured from *in vivo* and *in vitro* in the study of Milgrom et al. [83]. Based on the agreement between the predicted strains by the present models and the previous *in vitro* strain measurement study [82], it can be concluded that the models are able to predict the strain distributions around the cortical tibia during changing mechanical loading environment in the gait stance phase.

Validation of the Introduced Biomechanical Models

The accuracy of the biomechanical models is studied by comparing the numerical results of the ground reaction and muscular forces obtained from the models with their correspondences measured from the practical experiments. The results have acceptable overall agreement, while some discrepancy can be, however, observed between the measured muscular activities and modeled muscular force production patterns. To avoid invasive methodologies for measuring muscular forces *in vivo* because of ethical and legal constraints concerning humans, EMG data is commonly used to investigate the accuracy of muscular forces obtained from musculoskeletal models based on a qualitative comparison [66, 99]. However, EMG data can tell when the muscle is active, but it can not be considered an accurate indication of the muscular force patterns and magnitudes in dynamic movements. The relationship between muscular forces and EMG data is nonlinear [104]. In addition, the duration of the muscle force signal may differ from the duration of the corresponding EMG signal due to the temporal disassociation between the two signals, which is accounted for by so-called electro-mechanical delay [25]. This implies that the muscle force pattern does not necessarily agree with the EMG pattern. Further, the nonlinear EMG- force relationship is dependent on the joint angle, which makes EMG-force relationship indeterminate in dynamic situations [105]. In addition, EMG data can not indicate the contribution of an individual muscle to the observed motion. For example a muscle can accelerate joints that it does not span and body segments which it is not attached to [99]. It is also important to bear in mind the methodological limitations of EMG measurements. More specifically, in order to predict the force output of a distinct muscle, it is imperative that the EMG recorded represents only the electrical activity of the muscle of interest. Especially in case of muscles where the electrode placement site is spatially in close proximity to some other muscle, there is almost invariably at least some unwanted signal (cross talk) recorded from the other adjacent muscle [106].

In the first model, the discrepancy between the tibialis anterior and biceps femoris forces obtained from the model, and their EMG measured from the experiment may be caused by the algorithm used to solve the muscular force production. The algorithm is based on changes in muscle length. Thus, in the case of tibialis anterior, the algorithm did not account for coactivation of muscles. In the analogy to isometric force production, a muscle can produce force without changing its length during coactivation of an antagonist muscle. As regards the biceps femoris, the discrepancy found may be explained because of the biarticulate nature of the biceps femoris muscle. The biarticulate muscle can produce force without changing its length. It can be noticed that there is a discrepancy found between the rectus femoris force obtained from both models and their measured EMG patterns from the experiments. This discrepancy can be explained that there might be a possibility that signals from surrounding muscles, especially vastus lateralis and vastus medialis may also have been recorded during the EMG measurements (cross talk) [107]. Accordingly, the initial activity noticed in the rectus femoris EMG pattern shown in Figure 4.15 may be caused by cross talk from vastus lateralis and vastus medialis where both of them are active at the beginning. The second high peak noticed in the force production patterns of the vastus lateralis and vastus medialis obtained from the second model may be caused by the over estimated ground reaction force during the push off phase which can be seen in Figure 4.16(B). Another reason which might have contributed to the discrepancy between the simulated muscular forces and the measured EMG activation patterns is the absence of a criterion for muscular force distribution. The muscle model used in this study lacks the activation dynamics, and thus a number of optimization techniques, such as the tracking dynamics optimization method [108], can not be applied in order to uniquely determine the contribution of each individual muscle during physical activity. Nevertheless, the forces of the five major muscle groups; gluteus maximus, gluteus medius, vastus, soleus, and gastrocnemius, which are the prime movers, contributing up to 70% of the total mechanical energy produced by all the muscles and supporting the whole body during walking [3], are predicted reasonably by the introduced models, except for the vastus muscle force, which is predicted less accurately.

4.8. Limitations of the Introduced Biomechanical Models

In addition to the general limitations discussed in Chapter 3, caused by the anatomical components used to develop a general flexible multibody biomechanical model, other specific limitations of the introduced models related to the tibial finite element model can be also listed as follows:

1. In the introduced models, the material properties of the cortical bone of the flexible tibia are assumed to be homogenous, while in reality they are inhomogeneous [25, 77]. The assumption of homogenous material properties may limit the models to be suitable for tibial strains analysis in the mid-region of the tibial shaft where the variation of the bone material properties is relatively low [77]. However, to acquire an estimate of the inhomogeneous properties of the bone, CT scans are needed. Therefore more sophisticated simulation of bone material properties based on CT scans may further improve the estimation of strain results using the introduced models.

2. In the introduced models, the tibial finite element model consists of the cortical bone only without taking into consideration the trabecular bone. Neglecting the trabecular bone may limit the models to be suitable for tibial strain analysis in the middle diaphysis of the tibia. This is due to the fact that in the middle diaphysis of the tibia, where the strains are estimated, there is little if any trabecular bone, and thus neglecting trabecular bone tissue may be justified as it may have an insignificant effect on the estimated strains. However, the introduced models may not be suitable for strain analysis in the tibial metaphyses where the trabecular bone extensively exists.

4.9. Future Development of the Introduced Biomechanical Models

Developing accurate multibody biomechanical models is challenging because of the intrinsic complexity of biological systems. The accuracy of using the flexible multibody simulation approach in predicting dynamic bone strains is basically limited to the complexity involved in developing multibody biomechanical models. Increasing the accuracy of the multibody biomechanical model can lead to a more accurate estimation of dynamic bone strains based on the flexible multibody approach. In the introduced biomechanical models, several future enhancement proposals can be suggested. These proposals may increase the accuracy of the bone strain estimation using the approach proposed in this study. The proposals can be listed as follows:

1. Despite the fact that most multibody biomechanical models, as well as the introduced models, assume that the muscle attachments are single points on the bone [3], more sophisticated muscle attachment simulation may lead to further enhancement of muscular force estimation. Thus, more accurate bone strains estimation can be achieved using the introduced models.
2. More sophisticated muscle model may lead to more accurate muscular force estimation. For example, the accuracy of the muscular forces predicted by the introduced models may be increased by using other muscle models. For example, Hill muscle model [67] or the musculotendon actuator model described in the

study of Zajac [66], or by using a combined muscle model consisting of a neural network to model the muscle activation dynamics based on EMG signals and Hill muscle model to account for the muscle contraction dynamics [109, 110].

3. Integrating magnetic resonance imaging techniques into a musculoskeletal modeling framework can enhance the modeling of musculoskeletal anatomy, muscle architecture, joint motion, muscle moments arms and muscle motion (muscle tissue deformation) [56]. For example, most musculoskeletal models, as well as the introduced models, represent the muscle geometry as a series of line segments [56]. This simplification limits the accuracy of muscles paths definition and assumes that all fibres within each muscle compartment have the same length and moment arm. Blemker and Delp [111] have shown that the limitations of the muscle model described as series of line segments can be overcome by using a 3-dimensional finite element model of a muscle based on MRI. In the introduced models, the prime actuator muscles of the simulated exercise may be modeled using 3-dimenisonal finite element models based on MRI to give better estimation of muscular forces and thus bone strains. However, using a 3-dimensional representation of a muscle based on MRI is still under development and research, as it can be considered impractical to be used in a large number of multibody biomechanical models due the expensive computation [111]. Figure 4.19 shows an example of 3-dimensional finite element models of gluteus maximus, gluteus medius, psoas and illiacus generated on the basis of MRI and used to simulate hip flexion-extension [111].

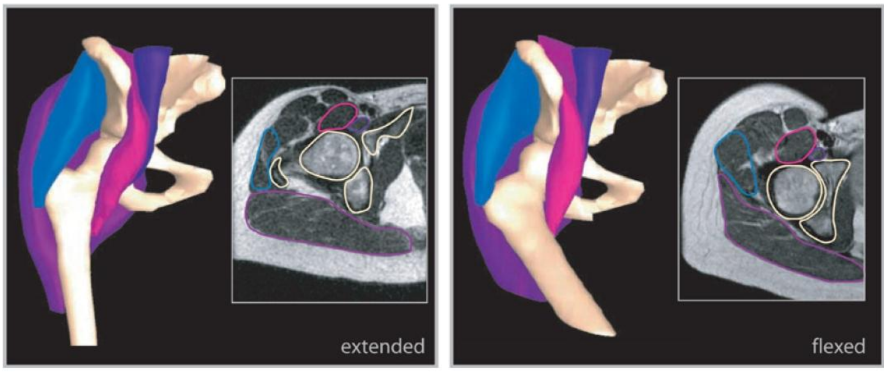

Figure 4.19 3-dimensional finite element models of gluteus maximus, gluteus medius, psoas and illiacus generated based on MRI and used to simulate hip flexion-extension [111].

5. CONCLUSIONS

The objective of this study was to demonstrate the utility of the flexible multibody simulation approach in the field of dynamic bone strain analysis. It is evident that there is a strong relation between strains within the bone tissue and bone (re)modeling. This has been attributed to the fact that the soft tissues within a bone exhibit elastic deformations under physiological loading. In fact the skeleton’s capacity to withstand external loading is achieved and maintained because the adaptive (re)modeling of bone tissue is both sensitive and responsive to the functional demands placed upon it. The *in vivo* strain measurement is considered an invasive procedure and requires surgical implementation of strain gauges, and it might involve risks, principally those of infection. In addition, it is limited in practice to certain regions of superficial bones only. Based on previous studies, it was shown that the bone remodelling process relies on dynamic bone strains rather static strains. This shed a light on the uniqueness and significance of the flexible multibody approach in dynamic bone strain analysis. This is due to the fact that the finite element method may be limited to the static analysis of bone strains due to the expensive computation required for the dynamic analysis, especially for a biomechanical model consisting of several bodies. In addition, in rigid multibody biomechanical models the flexibility of the bones can not be taken into account, a fact that renders such models unfeasible for bone strain analysis. In order to investigate the capability of using the flexible multibody simulation approach in estimating bone strains during physical activity, two 3-dimensional musculoskeletal models with right flexible tibia in each model generated based on MRI were used as demonstration examples. The introduced models were applied to simulate walking on a level exercise in order to predict the tibial strains. The principal strains were obtained from the models at a location corresponding to the location defined in previous *in vivo* strain measurements at the anteromedial aspect of the right tibial midshaft. The predicted tibial strains were compared with their correspondences obtained from literature-based *in vivo* strain measurements conducted for walking. The simulated tibial strains predicted by the models were consistent with *in vivo* strain measurements. Further, the strain distributions around the cortical bone at the middle of the tibial shaft during the stance phase were found to be consistent with previous *in vitro* strain measurement study.

The floating frame of reference formulation was used in this study in the dynamic bone strain analysis during physical activity. The unique feature of the floating frame of reference formulation is the use of deformation modes in describing the deformation of the flexible body. This feature makes it feasible to be utilized in the dynamic analysis of bone strains, while the other methods can not be practical due the expensive computation. The proposed method was mainly limited to the complexity involved in developing multibody biomechanical models. Developing accurate musculoskeletal models is considered a challenging and ambitious task. This is attributed to the fact the mechanics of the human body, including changing geometry and changing muscle moment arms are complex. The models were verified by comparing numerical results of the ground reaction force and muscular force production patterns obtained by the models with their correspondences measured from the practical experiments. The introduced models were mainly limited to the procedure used for muscular forces estimation. Some discrepancy was found between the measured muscular activities and estimated muscular force patterns by the models. On the other hand, the models showed a good accuracy in mimicking the real mechanical loading environment of the ground reaction force measured from the experiment.

Based on the reasonable agreement between the simulated strain estimates and *in vivo* literature values, it can be concluded that the proposed approach may also be of use in the estimation of bone strains in general where other bones rather than tibia can be assumed as flexible bodies. Several future opportunities for development and research may be initiated with the potential of developing other biomechanical models based on the proposed approach that might be of use in the following medical applications: 1) studying strain behavior in bones that are not directly accessible *in vivo*; 2) designing targeted physical training exercises to improve skeletal rigidity; 3) developing of implants by applying dynamic strain analysis to assess how the implant material behaves under loading and 4) performing detailed internal strain analysis in the field of joint prostheses and characterize exercise induced loading in detail – e.g. whether the specific exercise will be able to result in cortical thickening through bone redistribution. However, this type of a detailed strain analysis might require a CT scanning, so that the inhomogeneous density and elasticity distribution of the bone as well as the internal structure could be better considered. Finally, it can be considered as a hypothesis that a more sophisticated muscle model and attachments, as well as bone material properties could further lead to a more accurate simulation of bone strains using the flexible multibody simulation approach presented in this study.

REFERENCES

[1] Bottasso, C. L., and Prilutsky, B. I., 2006, “A Numerical Procedure for Inferring from Experimental Data the Optimization Cost Functions Using a Multibody Model of the Neuro-Musculoskeletal System”, *Multibody System Dynamics*, **16**, pp. 123-154.

[2] Silva, M. P. T., and Ambrósio, J. A. C., 2002, “Kinematic Data Consistency in the Inverse Dynamics Analysis of Biomechanical Systems”, *Multibody System Dynamics*, **8**, pp. 219-239.

[3] Pandy, M. G., 2001, “Computer Modeling and Simulation of Human Movement”, *Annual Review of Biomedical Engineering*, **3**, pp. 245-273.

[4] Duda, G. N., Heller, M., Albinger, J., Schulz, O., Schneider, E., and Claes, L., 1998, “Influence of Muscle Forces on Femoral Strain Distribution”, *Journal of Biomechanics*, **31**, pp. 841-846.

[5] Cheung, J. T., Zhang, M., Leung, A. K., and Fan, Y. B., 2005, “Three-Dimensional Finite Element Analysis of the Foot during Standing - A Material Sensitivity Study”, *Journal of Biomechanics*, **38**, pp. 1045-1054.

[6] Van Rietbergen, B., Huiskes, R., Eckstein, F., and Rüegsegger, P., 2003, “Trabecular Bone Tissue Strains in the Healthy and Osteoporotic Human Femur” *Journal of Bone and Mineral Research*, **18**, pp. 1781-1788.

[7] Lotz, J. C., Cheal, E. J., and Hayes, W. C., 1991, “Fracture Prediction for the Proximal Femur Using Finite Element Models: Part I--Linear Analysis”, *Journal of Biomechanical Engineering*, **113**, pp. 353-360.

[8] Kasra, M., and Grynpas, M. D., 1998, “Static and Dynamic Finite Element Analyses of an Idealized Structural Model of Vertebral Trabecular Bone”, *Journal of Biomechanical Engineering*, **120**, pp. 267-272.

[9] Guo, X. E., Mcmahon, T. A., Keaveny, T. M., Hayes, W. C., and Gibson, L. J., 1994, “Finite Element Modeling of Damage Accumulation in Trabecular Bone under Cyclic Loading”, *Journal of Biomechanics*, **27**, pp. 145-155.

[10] Stolk, J., Verdonschot, N., Cristofolini, L., Toni, A., and Huiskes, R., 2002, “Finite Element and Experimental Models of Cemented Hips Joint Reconstructions Can Produce Similar Bone and Cement Strains in Pre-Clinical Tests”, *Journal of Biomechanics*, **35**, pp. 499-510.

[11] Ecker, J. A., and St Ville, J. A., 1989, “Part I. A Three Dimensional Finite Element Analysis Model of an Artificial Hip and Bone”, *Computers in Engineering, Proceedings of the International Computers in Engineering Conference and Exhibit*, California, USA, pp. 369-374.

[12] Kraus, C., Bock, H. G., and Mutschler, H., 2005, “Parameter Estimation for Biomechanical Models Based on a Special Form of Natural Coordinates”, *Multibody System Dynamics*, **13**, pp. 101-111.

[13] Delp, S. L., and Loan, J. P., 1995, “A Graphics-Based Software System to Develop and Analyze Models of Musculoskeletal Structures”, *Computers in Biology and Medicine*, **25**, pp. 21-34.

[14] LifeMOD User’s Manual, 2007, version 2007.0.0, Biomechanics Research Group, Inc, California, USA.

[15] Eberhard, P., Spägele, T., and Gollhofer, A., 1999, “Investigations for the Dynamical Analysis of Human Motion”, *Multibody System Dynamics*, **3**, pp. 1-20.

[16] Anderson, F. C., and Pandy, M. G., 1999, “A Dynamics Optimization Solution for Vertical Jumping in Three Dimensions”, *Computer Methods in Biomechanics and Biomedical Engineering*, **2**, pp. 201-231.

[17] Nagano, A., Yoshioka, S., Komura, T., Himeno, R., and Fukashiro, S., 2005, "A Three-Dimensional Linked Segmental Model of the Whole Human Body", *International Journal of Sport and Health Science*, **3**, pp. 311-325.

[18] Sasaki, K., and Neptune, R. R., 2006, "Differences in Muscle Function during Walking and Running at the Same Speed", *Journal of Biomechanics*, **39**, pp. 2005-2013.

[19] Bei, Y., and Fregly, B., 2004, "Multibody Dynamic Simulation of Knee Contact Mechanics", *Medical Engineering & Physics*, **26**, pp. 777-789.

[20] Silva, M. P. T., Ambrósio, J. A. C., and Pererira, M. S., 1997, "Biomechanical Model with Joint Resistance for Impact Simulation", *Multibody System Dynamics*, **1**, pp. 65-84.

[21] Ambrósio, J. A. C., and Silva, M. P. T., 2004, "Structural and Biomechanical Crashworthiness Using Multi-Body Dynamics", *Proceedings of the Institution of Mechanical Engineers, Part D: Journal of Automobile Engineering*, **218**, pp. 629-645.

[22] Delp, S. L., 1990, *Surgery Simulation: A Computer Graphics System to Analyze and Design Musculoskeletal Reconstructions of the Lower Limb*, Doctoral Thesis, Stanford University.

[23] Piazza, S. J., and Delp, S. L., 2001, "Three-Dimensional Dynamic Simulation of Total Knee Replacement Motion during Step-up Task", *Journal of Biomechanical Engineering* **123**, pp. 599-606.

[24] Turner, C. H., 1998, "Three Rules for Bone Adaptation to Mechanical Stimuli", *Bone*, **23**, pp. 399-407.

[25] Nigg, B. M., and Herzog, W., 1999, *Biomechanics of the Musculo-Skeletal System*, John Wiley & Sons, New York.

[26] Lanyon, L. E., and Rubin, C. T., 1984, “Static vs Dynamic Loads as an Influence on Bone Remodelling”, *Journal of Biomechanics*, **17**, pp. 897–905.

[27] Liskova, M., and Hert, J., 1971, “Reaction of Bone to Mechanical Stimuli. Part 2. Periosteal and Endosteal Reaction to Tibial Diaphysis in Rabbit to Intermittent Loading”, *Folia Morphologica*, **19**, pp. 301–317.

[28] Kannus, P., Niemi, S., Parkkari, J., Palvanen, M., Heinonen, A., Sievänen, H., Järvinen, T., Khan, K., and Järvinen, M., 2002, “Why is the Age-Standardized Incidence of Low Trauma Fractures Rising in Many Elderly Populations?”, *Journal of Bone and Mineral Research*, **7**, pp. 1363-1367.

[29] Kannus, P., Niemi, S., Parkkari, J., Palvanen, M., Vuori, I., and Järvinen, M., 1999, “Hip Fractures in Finland between 1970 and 1997 and Predictions for the Future”, *The Lancet*, **353**, pp. 802-805.

[30] Földhazy**,** Z.**,** Arndt, A., Milgrom, C., Finestone, A., and Ekenman, I., 2005, “Exercise-Induced Strain and Strain Rate in the Distal Radius”, *Journal of Bone and Joint Surgery*, **87**, pp. 261-266.

[31] Sievänen, H., Kannus, P., and Järvinen, T. L., 2007, “Bone Quality: An Empty Term”, *PLoS Medicine*, **4**, e27.

[32] Kohrt, W. M., Bloomfield, S. A., Little, K. D., Nelson, M. E., and Yingling, V. R., 2004, “American College of Sports Medicine Position Stand: Physical Activity and Bone Health”, *Medicine and Science in Sports and Exercise*, **36**, pp. 1985-1996.

[33] Sievänen, H., and Kannus, P., 2007, “Physical Activity Reduces the Risk of Fragility Fracture”, *PLoS Medicine*, **4**, e222.

[34] Skerry, T. M., 1997, “Mechanical Loading and Bone: What Sort of Exercise is Beneficial to the Skeleton?”, *Bone*, **20**, pp. 179-181.

[35] Shabana, A. A., 1998, *Dynamics of Multibody Systems*, Cambridge University Press, New York.

[36] De Jalon, J. G., and Bayo, E., 1994, *Kinematic and Dynamic Simulation of Multibody Systems: The Real Time Challenge*, Springer-Verlag, New York.

[37] Shabana, A. A., 1996, *Vibration of Discrete and Continuous Systems*, Springer-Verlag, New York.

[38] Escalona, J. L., Hussien, H. A., and Shabana, A. A., 1998, “Application of the Absolute Nodal Co-ordinate Formulation to Multibody System Dynamics”, *Multibody System Dynamics*, **214**, pp. 833-851.

[39] Shabana, A. A., 1997, “Definition of the Slopes and the Finite Element Absolute Nodal Coordinate Formulation”, *Multibody System Dynamics*, **1**, pp. 339–348.

[40] Shabana, A. A., and Yakoub, R. Y., 2001, “Three Dimensional Absolute Nodal Coordinate Formulation for Beam Elements: Theory”, *Journal of Mechanical Design*, **123**, pp. 606-613.

[41] Yakoub, R. Y., and Shabana, A. A., 2001, “Three Dimensional Absolute Nodal Coordinate Formulation for Beam Elements: Implementation and Application”, *Journal of Mechanical Design*, **123**, pp. 614-621.

[42] Mikkola, A. M., and Shabana, A. A., 2003, “A Non-Incremental Finite Element Procedure for the Analysis of Large Deformations of Plates and Shells in Mechanical System Applications”, *Multibody System Dynamics*, **9**, pp. 283-309.

[43] Shabana, A. A., 1997, “Flexible Multibody Dynamics: Review of Past and Recent Developments”, *Multibody System Dynamics*, **1**, pp. 189-222.

[44] Mayo, J., and Domínguez, J., 1996, “Geometrically Non-Linear Formulation of Flexible Multibody Systems in Terms of Beam Elements: Geometric Stiffness”, *Computers & Structures*, **59**, pp. 1039-1050.

[45] Wu, S. C., and Haug, E. J., 1988, “Geometric Non-Linear Substructuring for Dynamics of Flexible Mechanical Systems”, *International Journal for Numerical Methods in Engineering*, **26**, pp. 2211-2226.

[46] Burr, D. B., Milgrom, C., Fyhrie, D., Forwood, M., Nyska, M., Finestone, A., Hoshaw, S., Saiag, E., and Simkin, A., 1996, “In Vivo Measurement of Human Tibial Strains during Vigorous Activity”, *Bone*, **18**, pp. 405-410.

[47] Kim, S., and Haug, E. J., 1990, “Selection of Deformation Modes for Flexible Multibody Dynamics”, *Mechanics of Structures and Machines*, **18**, pp. 565-586.

[48] Meirovitch, L., 1975, *Elements of Vibration Analysis*, McGraw-Hill, New York.

[49] Wasfy, T. M., and Noor, A. K., 2003, “Computational Strategies for Flexible Multibody Systems”, *Applied Mechanics Reviews*, **56**, pp. 553-613.

[50] Craig, R. R., and Bampton, M. C. C., 1968, “Coupling of Substructures for Dynamic Analysis”, *American Institute of Aeronautics and Astronautics Journal*, **6**, pp. 1313-1319.

[51] Shabana, A. A., 1996, “Resonance Conditions and Deformable Body Co-Ordinate Systems”, *Journal of Sound and Vibration*, **192**, pp. 389-398.

[52] Shabana, A. A., 1996, “Finite Element Incremental Approach and Exact Rigid Body Inertia”, *Journal of Mechanical Design*, **118**, pp. 171-178.

[53] Garner, E., Lakes, R., Lee, T., Swan, C., and Brand, R., 2000, “Viscoelastic Dissipation in Compact Bone: Implications for Stress-Induced Fluid Flow in Bone”, *Journal of Biomechanical Engineering*, **122**, pp. 166-172.

[54] Reilly, D. T., and Burstein, A. H., 1975, “The Elastic and Ultimate Properties of Compact Bone Tissue”, *Journal of Biomechanics*, **8**, pp. 393-405.

[55] Ambrósio, J. A. C., and Nikravesh, P. E., 1992, “Elasto-Plastic Deformations in Multibody Dynamics”, *Nonlinear Dynamics*, **3**, pp. 85-104.

[56] Blemker, S. S., Asakawa, D. S., Gold, G. E., and Delp, S. L., 2007, “Image-Based Musculoskeletal Modeling: Applications, Advances, and Future Opportunities”, *Journal of Magnetic Resonance Imaging*, **25**, pp. 441–451.

[57] Kecskeméthy, A., and Weinberg, A., 2005, “An Improved Elasto-Kinematic Model of the Human Forearm for Biofidelic Medical Diagnosis”, *Multibody System Dynamics*, **14**, pp. 1-21.

[58] Kraus, C., Bock, H., and Mutschler, H., 2005, “Parameter Estimation for Biomechanical Models Based on a Special Form of Natural Coordinates”, *Multibody System Dynamics*, **13**, pp. 101-111.

[59] Leondes, C., 2000, *Biomechanical Systems: Techniques and Applications, Volume III: Musculoskeletal Models and Techniques*, CRC Press, Boca Raton.

[60] Warwick, R., and Williams, L. P., 1973, *Gray’s Anatomy*, Longman Group Ltd., Edinburgh.

[61] 3D-DOCTOR User’s Manual, 2007, version 4.0, Able Software Corp., Lexington, USA.

[62] SolidWorks User’s Manual, 2005, version SP3.1, Dassault Systemes, Sureness, France.

[63] ANSYS User’s Manual, 2001, version 11.0, ANSYS Inc., Canonsburg, USA.

[64] Amankwah, K., Triolo, R. J., and Kirsch, R., 2004, “Effects of Spinal Cord Injury on Lower-Limb Passive Joint Moments Revealed through a Nonlinear Viscoelastic Model”, *Journal of Rehabilitation Research and Development*, **41**, pp. 15-32.

[65] Lin, C. C. K., Ju, M. S., and Huang, H. W., 2005, “Gender and Age Effects on Elbow Joint Stiffness in Healthy Subjects”, *Archives of Physical Medicine and Rehabilitation*, **86**, pp. 82-85.

[66] Zajac, F. E., 1989, “Muscle and Tendon: Properties, Models, Scaling and Application to Biomechanics and Motor Control”, *Critical Reviews in Biomedical Engineering*, **17**, pp. 359-411.

[67] Hill, A. V., 1938, “The Heat Shortening and the Dynamic Constants of Muscle”, *Proceedings of the Royal Society of London. Series B, Biological Sciences*, **126**, pp. 136-195.

[68] Spägele, T., Kistner, A., and Gollhofer, A., 1999, “Modelling, Simulation and Optimisation of a Human Vertical Jump”, *Journal of Biomechanics*, **32**, pp. 521-530.

[69] Pressel, T., and Lengsfeld, M., 1998, “Functions of Hip Joint Muscles”, *Medical Engineering & Physics*, **20**, pp. 50-56.

[70] Huxley, A. F., 1974, “Muscular Contraction”, *Journal of Physiology*, **243**, pp. 1-43.

[71] Winters, J. M., and Stark, L., 1987, “Muscle Models: What Is Gained and What Is Lost by Varying Model Complexity”, *Biological Cybernetics*, **55**, pp. 403-420.

[72] Yamaguchi, G. T., 2001, *Dynamic Modeling of Musculoskeletal Motion: A Vectorized Approach for Biomechanical Analysis in Three Dimensions*, Springer-Verlag, New York.

[73] Hatze, H., 1981, “Estimation of Myodynamics Parameter Values from Observations on Isometrically Contracting Muscle Groups”, *European Journal of Applied Physiology and Occupational Physiology*, **46**, pp. 325-338.

[74] Eycleshymer, A. C., and Shoemaker, D. M., 1970, *A Cross-Section Anatomy*, Appleton-Century-Crofts, New York.

[75] Aggarwal, J. K., and Cai, Q., 1997, “Human Motion Analysis: A Review”, *Computer Vision and Image Understanding*, **7**, pp. 428-440.

[76] Ackermann, M., 2007, *Dynamics and Energetics of Walking with Prostheses*, Doctoral Thesis, University of Stuttgart.

[77] Cowin, S. C., 1989, *Bone Mechanics*, CRC Press, Boca-Raton.

[78] Vaughan C. L., Davis, B. L., and O'Connor, J. C., 1999, *Dynamics of Human Gait*, Kiboho Publishers, South Africa.

[79] Lanyon, L. E., Hampson, W. G., Goodship, A. E., and Shah, J. S., 1975, “Bone Deformation Recorded In Vivo from Strain Gauges Attached to the Human Tibial Shaft”, *Acta Orthopaedica Scandinavica*, **46**, pp. 256-268.

[80] Milgrom, C., Finestone, A., Simkin, A., Ekenman, I., Mendelson, S., Millgram, M., Nyska, M., Larsson, E., and Burr, D., 2000, “In-Vivo Strain Measurements to Evaluate the Strengthening Potential of Exercises on the Tibial Bone”, *Journal of Bone and Joint Surgery*, **8**, pp. 591-594.

[81] Milgrom, C., Radeva-Petrova, D. R., Finestone, A., Nyska, M., Mendelson, S., Benjuya, N., Simkin, A., and Burr, D., 2006, "The Effect of Muscle Fatigue on In Vivo Tibial Strains", *Journal of Biomechanics*, **40**, pp. 845-850.

[82] Peterman, M. M., Hamel, A. J., Cavanagh, P. R., Piazza, S. J., and Sharkey, N. A., 2001, "In Vitro Modeling of Human Tibial Strains during Exercise in Micro-Gravity", *Journal of Biomechanics*, **34**, pp. 693-698.

[83] Milgrom, C., Finestonec, A., Hameld, A., Mandesd, V., Burr, D., and Sharkey, A., 2004, "Comparison of Bone Strain Measurements at Anatomically Relevant Sites Using Surface Gauges versus Strain Gauged Bone Staples", *Journal of Biomechanics*, **37**, pp. 947-952.

[84] ADAMS Online Documentation, 2001, version 12.0, Mechanical Dynamics, Inc, Ann Arbor, Michican, USA.

[85] Al Nazer, R.**,** Rantalainen, T., Heinonen, A., Sievänen, H. and Mikkola, A., 2008, "Flexible Multibody Simulation Approach in the Analysis of Tibial Strain during Walking", *Journal of Biomechanics*, **41**, pp. 1036-1043.

[86] Al Nazer, R., Klodowski, A., Rantalainen, T., Heinonen, A., Sievänen, H. and Mikkola, A., 2008, "Analysis of Dynamic Strains in Tibia during Human Locomotion Based on Flexible Multibody Approach Integrated with Magnetic Resonance Imaging Technique", *Multibody System Dynamics*, Article in press.

[87] Al Nazer, R., Klodowski, A., Rantalainen, T., Heinonen, A., Sievänen, H. and Mikkola, A., 2008, "A Procedure Based on the Flexible Multibody Simulation Approach for Bone Strain Analysis during Human Locomotion", *Proceeding of the 8th International Symposium on Computer Methods in Biomechanics and Biomedical Engineering*, Porto, Portugal.

[88] Zhang, L. Q., Portland, G. H., Wang, G., DiRaimondo, C. A., Nuber, G. W., Bowen, M. K., and Hendrix R. W., 2000, "Stiffness, Viscosity, and Upper-Limb Inertia about the Glenohumeral Abduction Axis", *Journal of Orthopaedic Research*, **18**, pp. 94-100.

[89] Leger, A. B., and Milner, T. E., 2000, "Passive and Active Wrist Joint stiffness following Eccentric Exercise", *European Journal of Applied Physiology*, **82**, 472-479.

[90] Rao, S. S., 1999, *The Finite Element Method in Engineering*, Butterworth Heinemann, Woburn, USA.

[91] Dong, X. N., and Guo, X. E., 2004, "The Dependence of Transversely Isotropic Elasticity of Human Femoral Cortical Bone on Porosity", *Journal of Biomechanics*, **37**, pp. 1281-1287.

[92] Gilchrist, L. A., and Winter, D. A., 1996, "A Two-Part, Viscoelastic Foot Model for Use in Gait Simulations", *Journal of Biomechanics*, **29**, pp. 795-798.

[93] Hermens, H. J., Freriks, B., Disselhorst-Klug, C., and Rau, G., 2000, "Development of Recommendations for SEMG Sensors and Sensor Placement Procedures", *Journal of Electromyography and Kinesiology*, **10**, pp. 361-374.

[94] Rainoldi, A., Melchiorri, G., and Caruso, I., 2004, "A Method for Positioning Electrodes during Surface EMG Recordings in Lower Limb Muscles", *Journal of Neuroscience Methods*, **134**, pp. 37-43.

[95] MATLAB User's Manual, 2005, version 7.1, The MathWorks Inc., Natick, USA.

[96] Dias Rodrigues, J. F., Lopes, H., De Melo, F. Q., and Simoes, J. A., 2004, “Experimental Modal Analysis of a Synthetic Composite Femur”, *Society for Experimental Mechanics*, **44**, pp. 29-32.

[97] Hibbeler, R. C., 2005, *Mechanics of Materials*, Prentice-Hall, Singapore.

[98] Burr, D. B., 1997, “Muscle Strength, Bone Mass, and Age-Related Bone Loss”, *Journal of Bone and Mineral Research*, **12**, pp. 1547-1551.

[99] Delp, S. L., Anderson, F. C., Arnold, A., S., Loan, P., Habib, A., John, C. T., Guendelman, E., and Thelen, D. G., 2007, “OpenSim: Open-Source Software to Create and Analyze Dynamic Simulations of Movement”, *IEEE Transactions on Biomedical Engineering*, **54**, pp. 1940-1950.

[100] Duda, G. N., Brand, D., Freitag, S., Lierse, W. and Schneider, E., 1996, “Variability of Femoral Muscle Attachments”, *Journal of Biomechanics*, **29**, pp. 1183-1190.

[101] Sharkey, N. A., and Hamel, A. J., 1998, “A Dynamic Cadaver Model of the Stance Phase of Gait: Performance Characteristics and Kinetic Validation”, *Clinical Biomechanics*, **13**, pp. 420-433.

[102] Biewener, A. A.,1991, “Musculoskeletal Design in Relation to Body Size”, *Journal of Biomechanics*, **24**, pp. 19-29.

[103] Garcia, G. J., and da Silva, J. K., 2004, “On the Scaling of Mammalian Long Bones”, The Journal of Experimental Biology, **207**, pp. 1577-1584.

[104] Brown, S. H. M., and McGill, S. M., 2008, “Co-Activation Alters the Linear versus Non-Linear Impression of the EMG–Torque Relationship of Trunk Muscles”, *Journal of Biomechanics*, **41**, pp. 491-497.

[105] Doheny, E. P., Lowery, M. M., FitzPatrick, D. P., and O'Malley, M. J., 2007, "Effect of Elbow Joint Angle on Force–EMG Relationships in Human Elbow Flexor and Extensor Muscles", *Journal of Electromyography and Kinesiology*, Article in press.

[106] Basmajian, J. V., and De Luca, C. J., 1985, *Muscles Alive*, Williams and Wilkins, Baltimore.

[107] Byrne, C. A., Lyons, G. M., Donnelly, A. E., O'Keeffe, D. T., Hermens, H., and Nene, A., 2005, "Rectus Femoris Surface Myoelectric Signal Cross-Talk during Static Contractions", *Journal of Electromyography and Kinesiology*, **15**, pp. 564-575.

[108] Seth, A., and Pandy, M., 2006, "A Neuromusculoskeletal Tracking Method for Estimating Individual Muscle Forces in Human Movement", *Journal of Biomechanics*, **40**, pp. 356 – 366.

[109] Wang, L., and Buchanan, T. S., 2002, "Prediction of Joint Moments Using a Neural Network Model of Muscle Activations from EMG Signals", *IEEE Transactions on Neural Systems and Rehabilitation Engineering*, **10**, pp. 30-37.

[110] Song, R., and Tong, K. Y., 2005, "Using Recurrent Artificial Neural Network Model to Estimate Voluntary Elbow Torque in Dynamic Situations", *Medical & Biological Engineering & Computing*, **43**, pp. 473-480.

[111] Blemker, S. S., and Delp, S. L., 2005, "Three-Dimensional Representation of Complex Muscle Architectures and Geometries", *Annals of Biomedical Engineering*, **33**, pp. 661–673.

APPENDIX A

(I) The third model and the results obtained from it are presented in Figures 1-6 and Tables 1-3.

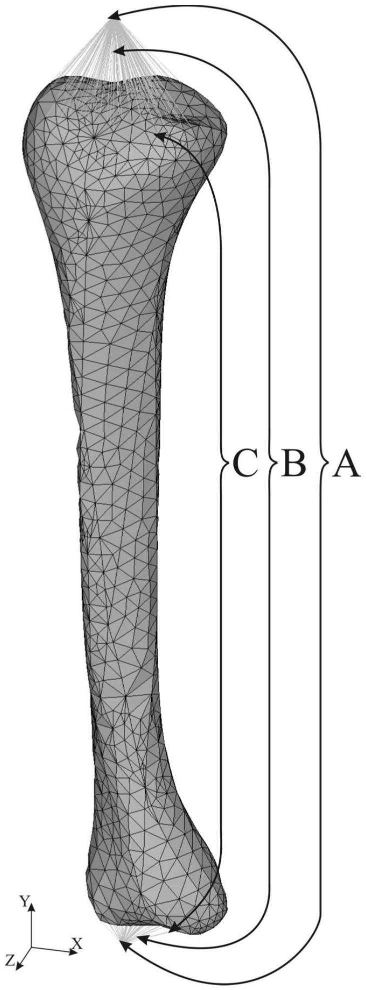

Figure 1 The tibial finite element model generated based on MRI of the third model and used in the forward dynamics simulation for strain analysis (*n* = 12726). A = two selected boundary nodes, B = massless rigid beams and C = surface nodes.

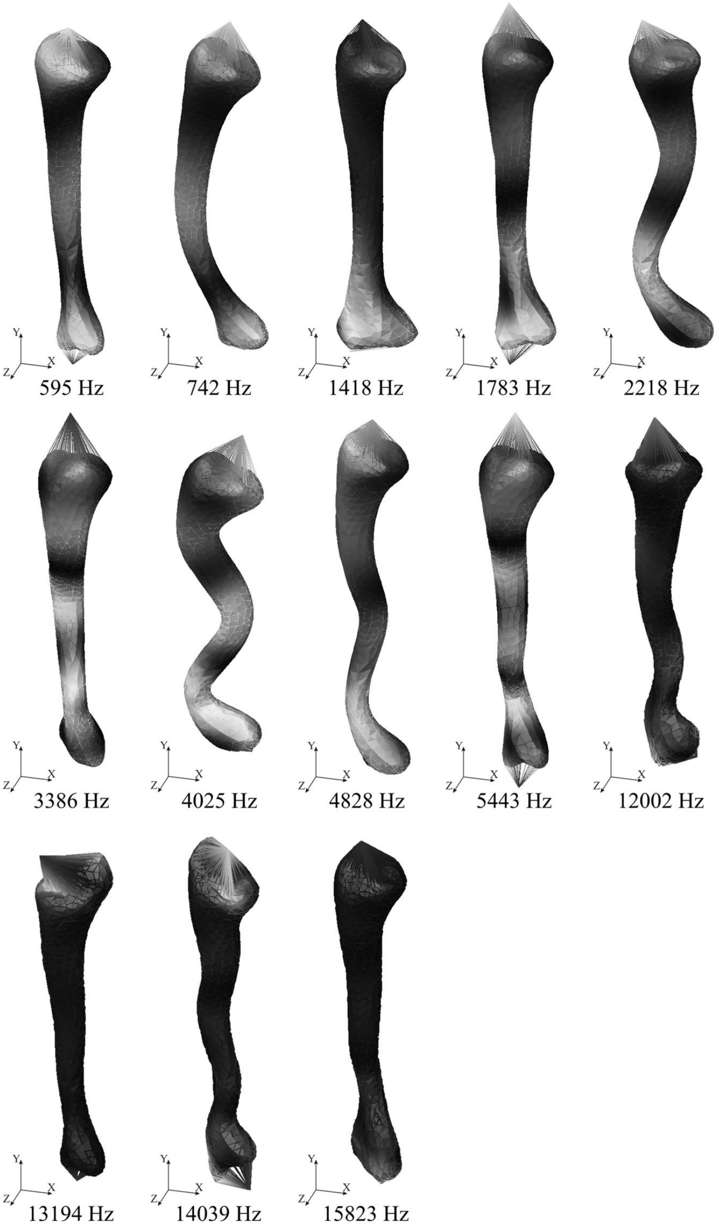

595 Hz 742 Hz 1418 Hz 1783 Hz 2218 Hz

3386 Hz 4025 Hz 4828 Hz 5443 Hz 12002 Hz

13194 Hz 14039 Hz 15823 Hz

Figure 2 The selected tibial deformation modes with their natural frequencies of the flexible tibia used in the third model.

Table 1 The principal and maximum shear strain magnitudes with their rates obtained from the third model.

	Strain magnitude [microstrain]			**Strain rate [microstrain/s]**		
	Max principal	Min principal	Max Shear	Max	Min	Max shear
Third model	260	-613	872	3100	-5750	10350

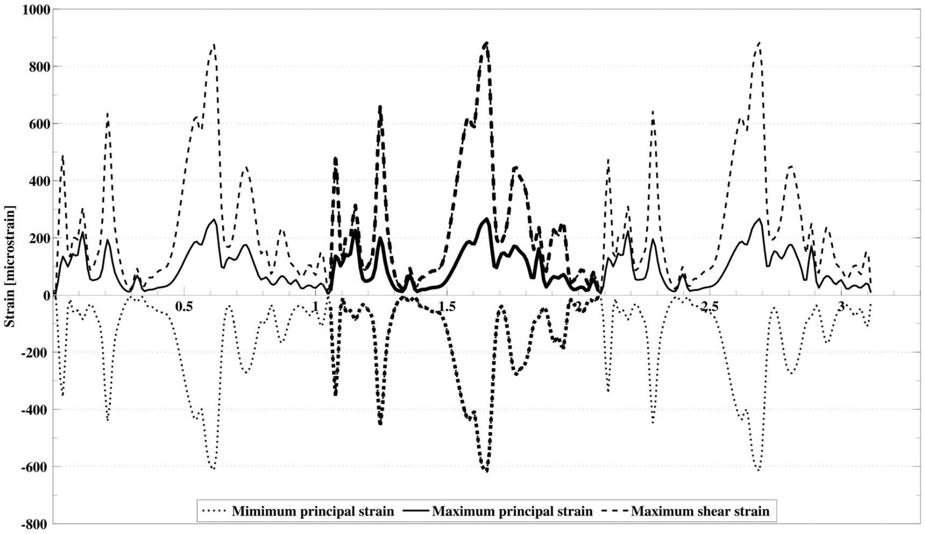

Figure 3 Simulated maximum and minimum principal strains and maximum shear strain curves at the anteromedial aspect of the right tibial shaft of the third model for three walking cycles. The bolded line corresponds to one walking cycle.

Table 2 Cross-correlation coefficient (γ) between measured and simulated values of the ground reaction and muscular forces of the third model.

Compared Items	**Third model** (γ)
Ground reaction force	0.96
Soleus	0.93
Gluteus medius	0.88
Vastus lateralis	0.44
Tibialis anterior	0.22
Biceps femoris	0.71
Rectus femoris	0.42
Gastrocnemius Lateralis	0.76
Gastrocnemius Medialis	0.81
Gluteus maximus	0.89
Vastus medialis	0.48

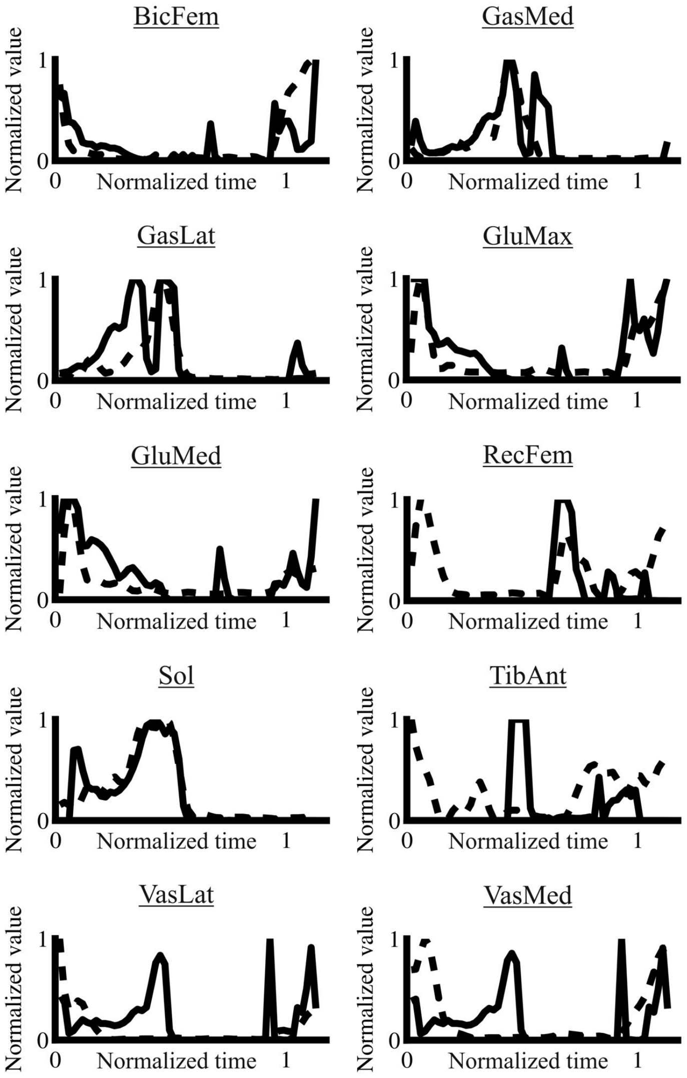

Figure 4 Measured electromyographical (EMG) muscle activity (dashed line ---) and simulated muscular force production (solid line —–) obtained from the third model plotted against normalized time for one walking cycle. EMG and force values are normalized to the maximum values for each plot. EMG is rectified and low pass filtered at 10 Hz. BicFem = biceps femoris, GluMed = gluteus medius, RecFem = rectus femoris, Sol = soleus, TibAnt = tibialis anterior, VasLat = vastus lateralis, GasLat = gastrocnemius lateralis, GasMed = gastrocnemius medialis, VasMed = Vastus medialis, GluMax = Gluteus maximus.

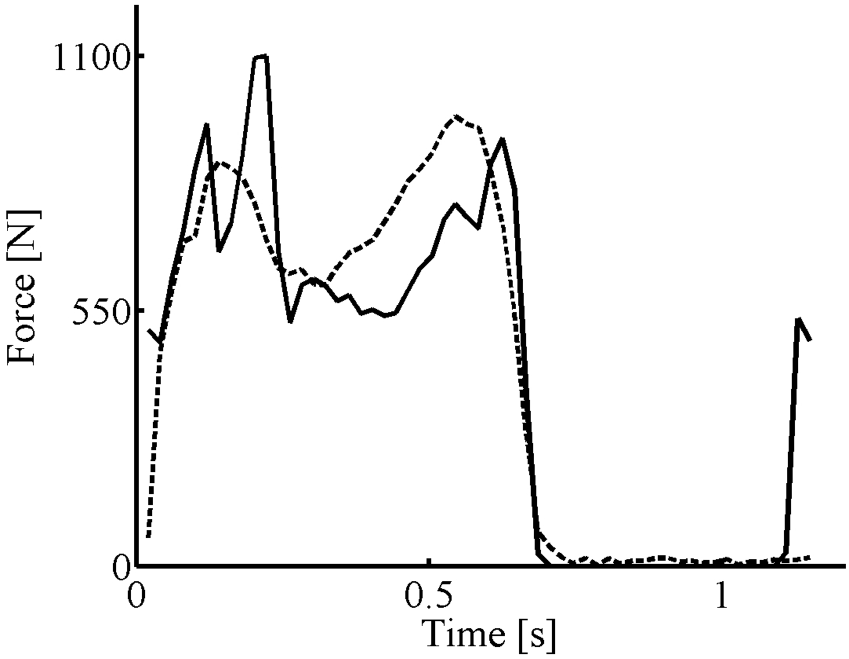

Figure 5 Measured ground reaction force (dashed line ---) and simulated ground reaction force (solid line ——) obtained from the third model plotted against time for one walking cycle.

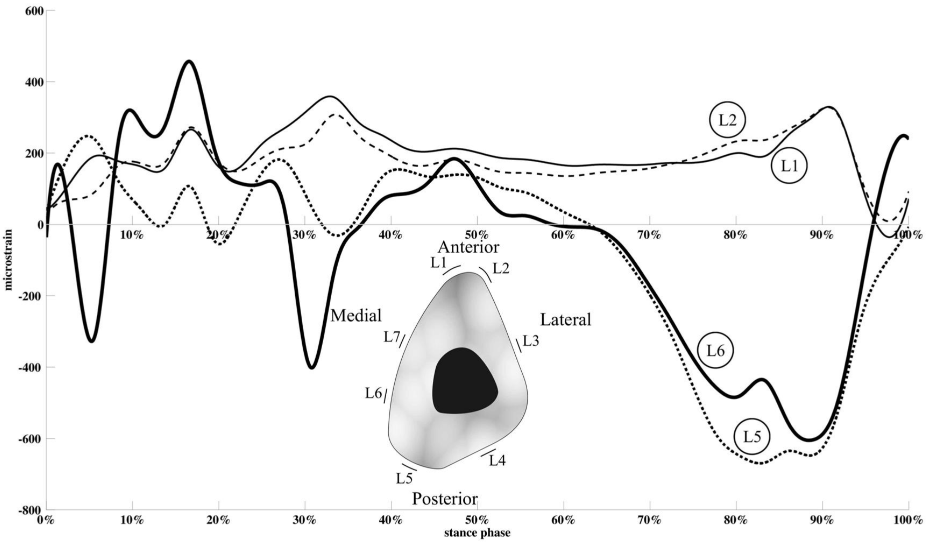

Figure 6 Simulated axial strain curves at two anterior and two posterior sites around the cortical tibia at the middle shaft during the stance phase. The shape represents the cortical cross sectional geometry at the middle of the third subject's tibia with marked locations that correspond most closely to the locations defined in the study of Peterman et al. [82].

Table 3 Strain distribution magnitudes about the cortical tibia obtained from the third model.

Locations & Type of strains	Third model [microstrain]
L1	
Axial strain	357
Maximum principal strain	359
Minimum principal strain	-267
Maximum shear	626
L2	
Axial strain	311
L3	
Axial strain	-646
L4	
Axial strain	-812
L5	
Axial strain	-670
Maximum principal strain	490
Minimum principal strain	-680
Maximum shear	1170
L6	
Axial strain	-605
L7	
Axial strain	-583

(II) The deformation modes calculated for each tibial finite element model using **ANSYS** are shown in Figures 7-9.

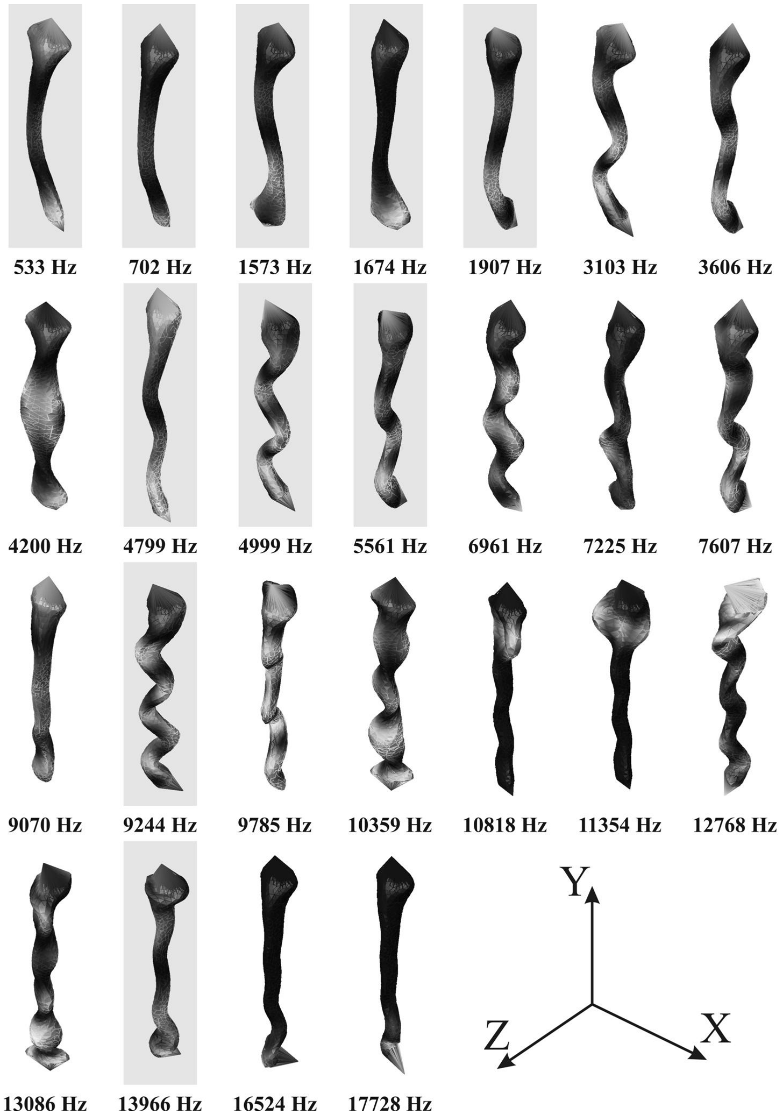
533 Hz
702 Hz
1573 Hz
1674 Hz
1907 Hz
3103 Hz
3606 Hz
4200 Hz
4799 Hz
4999 Hz
5561 Hz
6961 Hz
7225 Hz
7607 Hz
9070 Hz
9244 Hz
9785 Hz
10359 Hz
10818 Hz
11354 Hz
12768 Hz
13086 Hz
13966 Hz
16524 Hz
17728 Hz
Y
Z
X

Figure 7 Calculated deformation modes with their natural frequencies of the first model. Shaded modes present the significant deformation modes used in the numerical analysis.

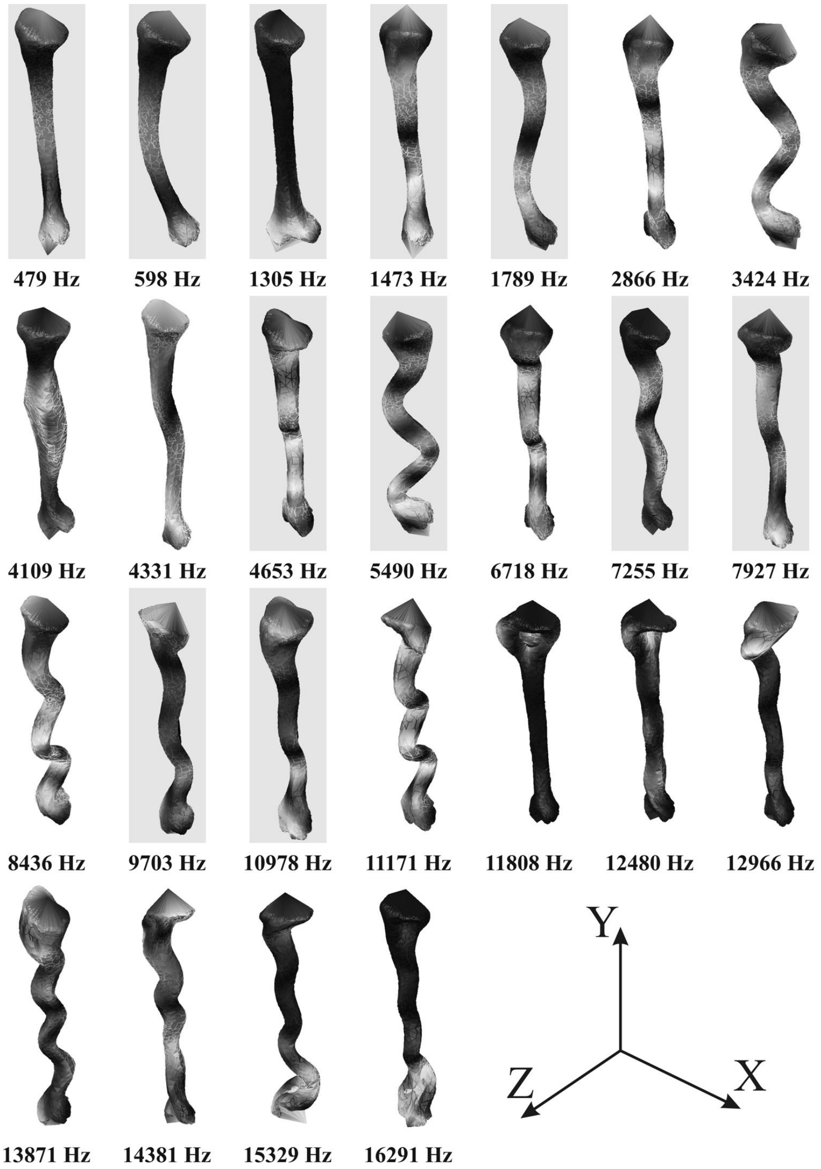
479 Hz
598 Hz
1305 Hz
1473 Hz
1789 Hz
2866 Hz
3424 Hz
4109 Hz
4331 Hz
4653 Hz
5490 Hz
6718 Hz
7255 Hz
7927 Hz
8436 Hz
9703 Hz
10978 Hz
11171 Hz
11808 Hz
12480 Hz
12966 Hz
13871 Hz
14381 Hz
15329 Hz
16291 Hz
Y
Z
X

Figure 8 Same as Figure 7 for the second model.

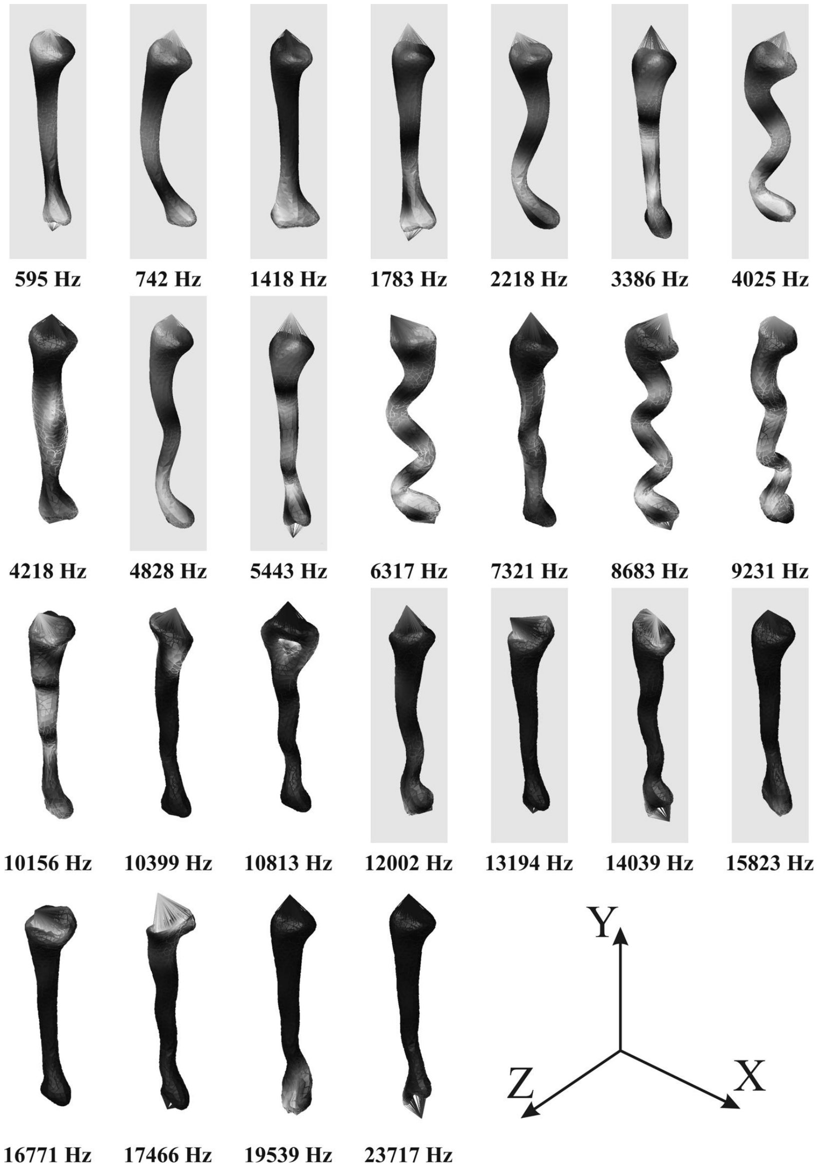
595 Hz
742 Hz
1418 Hz
1783 Hz
2218 Hz
3386 Hz
4025 Hz
4218 Hz
4828 Hz
5443 Hz
6317 Hz
7321 Hz
8683 Hz
9231 Hz
10156 Hz
10399 Hz
10813 Hz
12002 Hz
13194 Hz
14039 Hz
15823 Hz
16771 Hz
17466 Hz
19539 Hz
23717 Hz
Y
Z
X

Figure 9 Same as Figure 7 for the third model.

(III) Figures 10, 11 and 12 show the tibial strains reported in the previous *in vivo* [79, 46] and *in vitro* [82] strain measurement studies.

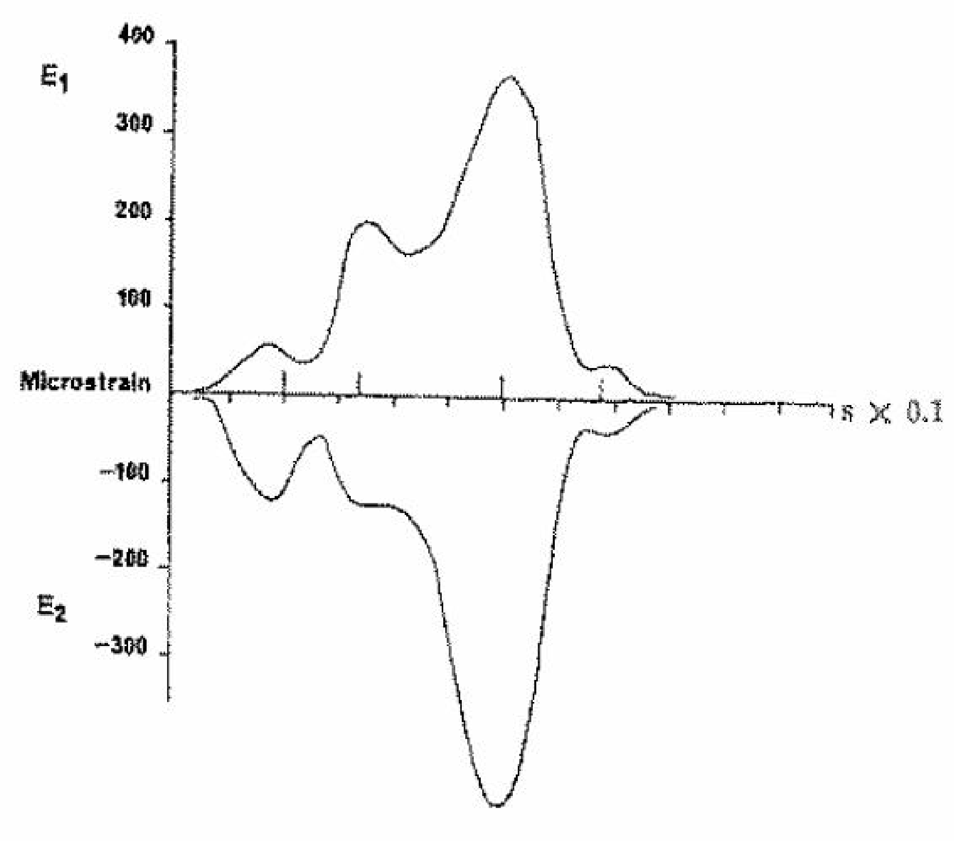

Figure 10 Maximum and minimum principal strains curves obtained by Lanyon et al. [79] at the anteromedial aspect of the tibial midshaft shaft during one cycle of walking on a belt without shoes.

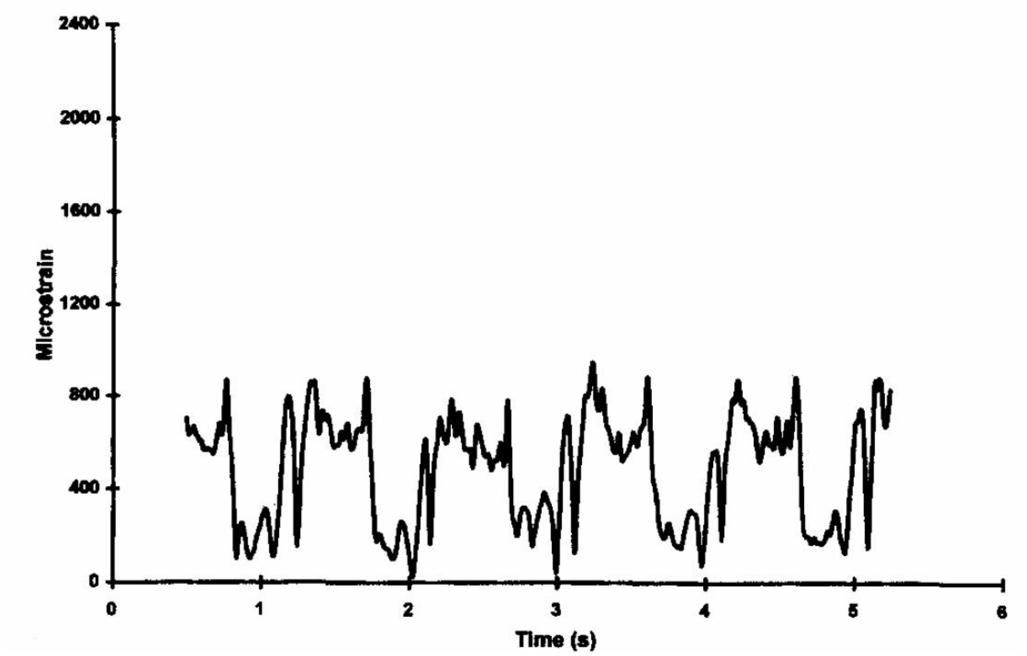

Figure 11 Maximum shear strain curve obtained by Burr et al. [46] at the anteromedial aspect of the tibial midshaft shaft during walking with boots.

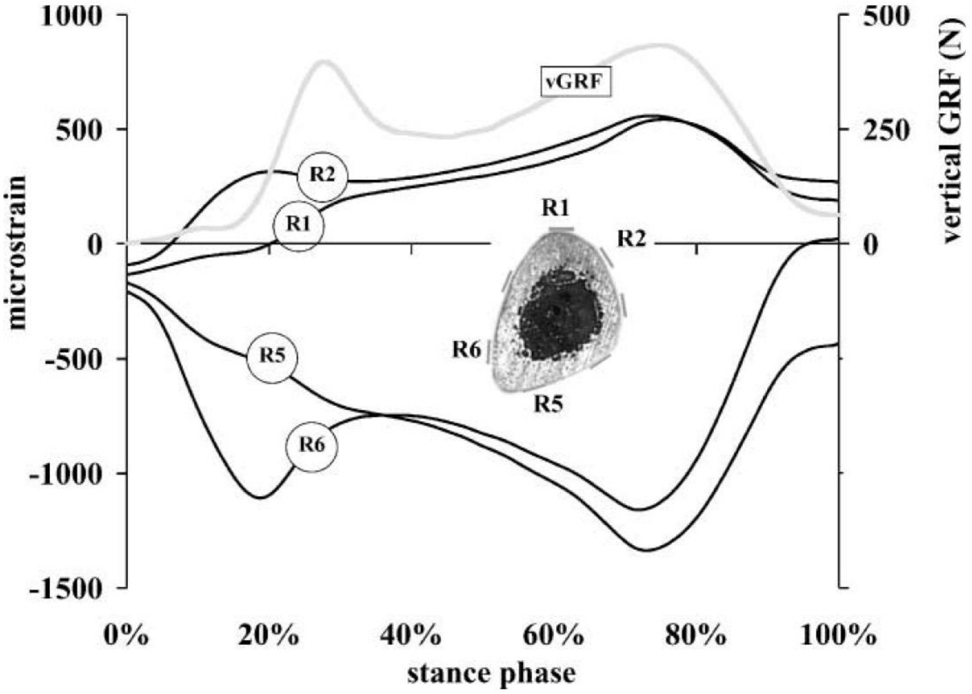

Figure 12 Axial strain curves obtained by Peterman et al. [82] at two anterior and two posterior sites around the cortical tibia at the middle shaft during the stance phase. The light grey curve represents the measured vertical ground reaction force during the *in vitro* strain measurements.

ACTA UNIVERSITATIS LAPPEENRANTAENSIS

268. BUTYLINA, SVETLANA. Effect of physico-chemical conditions and operating parameters on flux and retention of different components in ultrafiltration and nanofiltration fractionation of sweet whey. 2007. Diss.

269. YOUSEFI, HASSAN. On modelling, system identification and control of servo-systems with a flexible load. 2007. Diss.

270. QU, HAIYAN. Towards desired crystalline product properties: In-situ monitoring of batch crystallization. 2007. Diss.

271. JUSSILA, IIRO. Omistajuus asiakasomisteisissa osuuskunnissa. 2007. Diss.

272. 5th Workshop on Applications of Wireless Communications. Edited by Jouni Ikonen, Matti Juutilainen and Jari Porras. 2007.

273. 11th NOLAMP Conference in Laser Processing of Materials Lappeenranta, August 20-22, 2007. Ed. by Veli Kujanpää and Antti Salminen. 2007.

274. 3rd JOIN Conference Lappeenranta, August 21-24, 2007. International Conference on Total Welding Management in Industrial Applications. Ed. by Jukka Martikainen. 2007.

275. SOUKKA, RISTO. Applying the principles of life cycle assessment and costing in process modeling to examine profit-making capability. 2007. Diss.

276. TAIPALE, OSSI. Observations on software testing practice. 2007. Diss.

277. SAKSA, JUHA-MATTI. Organisaatiokenttä vai paikallisyhteisö: OP-ryhmän strategiat institutionaalisten ja kilpailullisten paineiden ristitulessa. 2007. Diss.

278. NEDEOGLO, NATALIA. Investigation of interaction between native and impurity defects in ZnSe. 2007. Diss.

279. KÄRKKÄINEN, ANTTI. Dynamic simulations of rotors during drop on retainer bearings. 2007. Diss.

280. KARPOVA, TATJANA. Aqueous photocatalytic oxidation of steroid estrogens. 2007. Diss.

281. SHIPILOVA, OLGA. Particle transport method for convection-diffusion-reaction problems. 2007. Diss.

282. ILONEN, JARMO. Supervised local image feature detection. 2007. Diss.

283. BOTAR-JID, CLAUDIU CRISTIAN. Selective catalytic reduction of nitrogen oxides with ammonia in forced unsteady state reactors. Case based and mathematical model simulation reasoning. 2007. Diss.

284. KINNUNEN, JANNE. Direct-on-line axial flux permanent magnet synchronous generator static and dynamic performance. 2007. Diss.

285. VALTONEN, MIKKO. Performance characteristics of an axial-flux solid-rotor-core induction motor. 2007. Diss.

286. PUNNONEN, PEKKA. Impingement jet cooling of end windings in a high-speed electric machine. 2007. Diss.

287. KÄRRI, TIMO. Timing of capacity change: Models for capital intensive industry. 2007. Diss.

288. TUPPURA, ANNI. Market entry order and competitive advantage of the firm. 2007. Diss.

289. TARKIAINEN, ANSSI. Field sales management control: Towards a multi-level theory. 2007. Diss.

290. HUANG, JUN. Analysis of industrial granular flow applications by using advanced collision models. 2007. Diss.

291. SJÖMAN, ELINA. Purification and fractionation by nanofiltration in dairy and sugar and sweetener industry applications. 2007. Diss.

292. AHO, TUOMO. Electromagnetic design of a solid steel rotor motor for demanding operation environments. 2007. Diss.

293. PURHONEN, HEIKKI. Experimental thermal hydraulic studies on the enhancement of safety of LWRs. 2007. Diss.

294. KENGPOL, ATHAKORN. An evaluation of ICTs investment using decision support systems: Case applications from distributor´s and end user´s perspective group decision. 2007. Diss.

295. LASHKUL, ALEXANDER. Quantum transport phenomena and shallow impurity states in CdSb. 2007. Diss.

296. JASTRZĘBSKI, RAFAŁ PIOTR. Design and implementation of FPGA-based LQ control of active magnetic bearings. 2007. Diss.

297. GRÖNLUND, TANJA. Development of advanced silicon radiation detectors for harsh radiation environment. 2007. Diss.

298. RUOKONEN, MIKA. Market orientation in rapidly internationalizing small companies – evidence from the software industry. 2008. Diss.

299. OIKARINEN, TUIJA. Organisatorinen oppiminen – tapaustutkimus oppimisprosessien jännitteistä teollisuusyrityksessä. 2008. Diss.

300. KARHULA, JUKKA. Cardan gear mechanism versus slider-crank mechanism in pumps and engines. 2008. Diss.

301. RAJAMÄKI, PEKKA. Fusion weld metal solidification: Continuum from weld interface to centerline. 2008. Diss.

302. KACHINA, ANNA. Gas-phase photocatalytic oxidation of volatile organic compounds. 2008. Diss.

303. VIRTANEN, PERTTU. Evolution, practice and theory of European database IP law. 2008.

304. TANNINEN, KATI. Diffusion of administrative innovation: TQM implementation and effectiveness in a global organization. 2008. Diss.

305. PUISTO, ANTTI. The initial oxidation of transition metal surfaces. 2008. Diss.

306. FELLMAN, ANNA. The effects of some variables on CO_2 laser-MAG hybrid welding. 2008. Diss.

307. KALLIOINEN, MARI. Regenerated cellulose ultrafiltration membranes in the treatment of pulp and paper mill process waters. 2008. Diss.

308. PELTOLA, SATU. Capability matrix – identifying and evaluating the key capabilities of purchasing and supply management. 2008. Diss.

309. HONKAPURO, SAMULI. Performance benchmarking and incentive regulation – considerations of directing signals for electricity distribution companies. 2008. Diss.

310. KORHONEN, KIRSI. Facilitating coordination improvement efforts in cross-functional process development programs. 2008. Diss.